EXOPLANET TRANSIT PHOTOMETRY FOR STELLAR ACTIVITY AND EXOMOON RESEARCH

A Thesis Submitted by

Shelley M. Zaleski
M.S. Physics, B.S. Physics

For the Award of

Doctor of Philosophy

2021

Abstract

Photometry underlies important discoveries in observational astronomy, from the detection of stellar magnetic phenomena unveiling dynamic dynamo processes to the much sought-after identification of exomoons. Transit light curves contain a wealth of information on planet-hosting stars and the celestial bodies orbiting them.

This body of work presents an analysis and interpretation of transit light curves of solar-type stars. Periodic flux dimming signals the transit of an exoplanet, with the degree of dimming indicative of the exoplanet's radial size. Small scale flux modulations within the transit duration, or dimming, appear as bumps and dips and are attributed to starspots and faculae on an unresolved stellar face. From the size and location of these photospheric features, much can be learned about the host star: differential rotation, active longitudes, and magnetic activity cycles.

For this thesis, two stars were selected as targets from the more than 150,000 stars observed by the *Kepler* telescope, Kepler-71 and Kepler-45. Both are solar-type stars, as defined by having a radiative core surrounded by a convective envelope. Kepler-71 is a G star somewhat younger than the Sun and orbited by a single hot Jupiter. The analysis of Kepler-71 transits presents the first use of faculae to measure stellar rotation period at the transit latitude. The difference between the mean stellar rotation period and the latitudinal rotation period indicate an almost rigid rotation. A complete anal-

ysis is presented in Chapter 2.

Kepler-45 is a young M dwarf, also orbited by a single hot Jupiter. The inspection of transit light curves revealed two distinct types of small-scale amplitude variations - temporally confined flux changes due to starspots and faculae, and extended decreases in flux due to a possible satellite of the hot Jupiter Kepler-45b. For the former case, Chapter 3 presents the first analysis of stellar activity for an M1V dwarf.

Investigation of the latter type of flux modulations revealed interesting evidence for an exomoon companion to Kepler-45b. A method for analyzing this evidence for a super-Earth exomoon is discussed in Chapter 4. The discovery of the first super-Earth exomoon would provide an important observational constraint for theories of planetary formation and evolution, and exomoon orbital stability. This potential exomoon candidate is expected to become an observational target and the subject of many future studies.

Certification of Thesis

This Thesis is the work of Shelley M. Zaleski except where otherwise acknowledged, with the majority of the authorship of the papers presented as a Thesis by Publication undertaken by the Student. The work is original and has not previously been submitted for any other award, except where acknowledged.

Student and supervisors signatures of endorsement are held at USQ.

Associate Professor Stephen C. Marsden
Principal Supervisor

Professor Bradley D. Carter
Associate Supervisor

Professor Adriana Valio
Associate Supervisor

List of Contributions from Publication Co-authors

This section details contributions by the various authors for each of the papers presented in this thesis by publication.

Chapter 2, Zaleski et al. (2019):
Zaleski, S. M., Valio, A., Marsden, S. C., & Carter, B. D. (2019). Differential rotation of Kepler-71 via transit photometry mapping of faculae and starspots. *MNRAS*, 484(1), 618–630

Author	Percent Contribution	Tasks Performed
S. M. Zaleski	85	Performed target selection, analysis, interpretation, wrote all drafts of paper, conception of project.
A. Valio S. C. Marsden B. D. Carter	15	Conception of project, suggested edits to manuscript, solar profile analysis

Chapter 3, Zaleski et al. (2020a):

Zaleski, S. M., Valio, A., Carter, B. D., & Marsden, S. C. (2020a). Activity and differential rotation of the early M dwarf Kepler-45 from transit mapping. *MNRAS*, 492(4), 5141–5151

Author	Percent Contribution	Tasks Performed
S. M. Zaleski	85	Performed target selection, analysis, interpretation, wrote all drafts of paper, conception of project.
A. Valio B. D. Carter S. C. Marsden	15	Conception of project, interpretation, suggested edits to manuscript.

Chapter 4, Zaleski et al. (2020b):

Zaleski, S. M., Valio, A., Guimaraes, A. H. F., Carter, B. D., & Marsden, S. C. (2020b). Method for Photometric Evaluation of Gnomic Exomoons: Case Study of the Kepler-45b System, submitted

Author	Percent Contribution	Tasks Performed
S. M. Zaleski	80	Performed analysis, interpretation, wrote all drafts of paper.
A. Valio A. H. F. Guimaraes S. C. Marsden B. D. Carter	20	Conception of project, interpretation, exomoon stability simulation, suggested edits to manuscript

Acknowledgments

It is with the greatest appreciation that I thank the people and organizations who have supported me and made completion of this thesis possible.

My life in science spans decades. At 11 years of age, I declared that I would become an astrophysicist. After a detour through High Energy Physics searching for unseen elementary particles, I have upheld that declaration. Now, I search for the unknown of a much larger scale.

I would like to recognize the financial support of the University of Southern Queensland awarded to me as the International Fees Research Scholarship. This scholarship did more than defray the cost of tuition. By acknowledging the quality and merit of my research, it was a source of encouragement.

I would also like to thank the members of the NASA Kepler Mission for their contributions to astronomy and astrophysics research. Data for this thesis was collected by the Kepler space telescope. Kepler is the gift that keeps giving.

I extend my deepest gratitude to the people who have shared in my long journey to a doctorate. I have had the good fortune of being mentored by

three people who are not only brilliant scientists but also unique and endearing individuals - Stephen Marsden, Brad Carter, and Adriana Valio. I have learned so much from them and am humbled by their wisdom and generosity of spirit. I look forward to being a colleague and not a student. I look forward to future collaborations and lasting friendships.

Success relies upon the support of others. The former and current PhD students at USQ share a common experience. To Matthew Mengel, Dag Evensberget, and Mathieu Clerté, I say 'thank you' for helping me through technical difficulties.

Finally, special thanks to my family and friends for their unwavering support. To my husband, thank you for forgiving the hours spent on my laptop. You have always supported and encouraged me. I could not have done this without you. To my daughters, I hope to forever be your source of inspiration, as you are mine. Always be fabulous! To my dear friends, thank you for accepting me as I am.

Thank you!

Contents

List of Figures

(Excluding publications included in Chapters 2-4)

List of Tables

(Excluding publications included in Chapters 2-4)

Abbreviations

CCD charge-coupled device
CoRoT COnvection, ROtation and planetary Transits

DI Doppler Imaging
DR25 Data Release 25

ESA European Space Agency

FWHM full width at half maximum

K2 Kepler Second Light
KOI Kepler Objects of Interest

LC long cadence
LOS line-of-sight

MCMC Markov Chain Monte Carlo
MIT Massachusetts Institute of Technology

NASA National Aeronautics and Space Administration

PDCSAP Pre-Search Data Conditioning Simple Aperture Photometry

PDVs photometric duration variations

PLATO PLAnetary Transits and Oscillations of stars

PRVs photometric radius variations

PTVs photometric timing variations

QBOs quasi-biennial oscillations

SAP Simple Aperture Photometry

SC short cadence

SOC Science Operations Center

TDVs transit duration variations

TESS Transiting Exoplanet Survey Satellite

TRVs transit radius variations

TTV$_p$ photometric transit timing variation

TTVs transit timing variations

XPG eXomoon Phase Gating

ZDI Zeeman Doppler Imaging

If we knew what it was we were doing, it would not be called research, would it?

Albert Einstein

Chapter 1 Introduction

The orbit of a celestial body, whether a planet or moon, is observable when its orbital path transits, or crosses, in front of a larger body in an observer's field-of-view. The fundamental principle of transits simply states that the passage, or transit, of a secondary, smaller body causes a distinct blockage of light from the primary body. In the case of host star-exoplanet systems, the reduction in stellar flux caused by an orbiting companion is detected as modulations in transit light curves. Since its introduction by Borucki & Summers (1984), the transit method has fueled the search for planets in Extra-Solar Systems, contributing more entries to the list of known exoplanets than other detection methods (including radial velocity, microlensing, direct imaging, pulsar timing, and astrometry).

The radial velocity method, or Doppler Spectroscopy, detects shifts in the wavelengths of light in a stellar spectrum due to a star's wobble about the center-of-mass shared by it and another massive body. Variations in the radial velocity of the star 51 Pegasi led Mayor & Queloz (1995) to the discovery of the first exoplanet, a Jupiter-mass planet orbiting a Sun-like star. Use of the radial velocity method continues in popularity for the measurement of exoplanet mass, though it is limited to massive planets orbiting close to their host stars (Wei, 2018). Today, the number of exoplanets discovered via the transit method greatly outweighs detection via radial velocity variation. Yet, in conjunction with the transit method, which affords measurement of exoplanet

radii, exoplanet densities may be estimated.

Microlensing, direct imaging, and pulsar timing variations ease the constraint on the semi-major axis of a planet's orbit imposed by the radial velocity method (Fischer et al., 2014). Exoplanet detection by gravitional microlensing requires that an exoplanet perturb the focused light emitted by a lensing star, acting as a second lens and magnifying that light. This technique is applicable to planets far from Earth in wide orbits about their host stars, but its use is limited by the need for perfect alignment of all bodies involved. Still, several dozen exoplanets have been detected via microlensing (Tsapras, 2018). Direct imaging is best suited to exoplanets orbiting young stars or brown dwarfs, far from their stars. Moreover, the detection is best if the observation is performed at infrared wavelengths, where the flux of the star is only a million times stronger than that of the exoplanet, as opposed to the billion factor in the visible. This technique has discovered a few self-luminous planets (Fischer et al., 2014). Similar to the radial velocity method, astrometry is sensitive to stellar wobble due to the presence of an exoplanet. Astrometric measurements disclose deviations in a star's sky position due to the gravitational pull of a planet from which exoplanet mass can be inferred (Perryman et al., 2014). The Gaia mission is expected to find tens of thousands of exoplanet via astrometry (Prusti et al., 2016).

Space-based transit observation missions dedicated to the acquisition of transit photometry continue to play a major role in the detection of stellar companions and afford a broad view of planetary and lunar transits within the Solar System and our neighborhood of the galaxy. Over the past ten years, CoRoT (COnvection, ROtation and planetary Transits; Baglin, 2003), Kepler (Borucki et al., 2003), K2 (Kepler Second Light; Howell et al., 2014), and TESS (Transiting Exoplanet Survey Satellite; Ricker et al., 2014), have cumulatively found thousands of exoplanets and exoplanet candidates [1].

The discovery of exoplanets via transit light curve analysis has far reaching implications. It contributes to the knowledge of extra-solar system architectures, showing that the structure of our Solar System with an orderly arrangement of inner dense

[1] https://exoplanetarchive.ipac.caltech.edu/

planets and outer gas giants may not be the galactic standard (Raymond et al., 2018). Most planet-hosting stars are solar-type main sequence stars of FGKM classification orbited by a preponderance of super-Earth and mini-Neptune sized exoplanets. As shown via indirect observation, planet occurrence rates increase as planet radius decreases and orbital period increases. Cool M dwarfs host the greatest number of Earth-sized worlds with an occurrence rate of 2 - 2.8 planets with orbital periods of less than 50 days (Mulders et al., 2015). Hot Jupiters comprise only 1% of planets orbiting Sun-like stars, and their cool analogs have an occurrence rate of 7% (Wittenmyer et al., 2019). A few hundred Jupiter-sized exoplanets are known to transit FGK stars with only 4 transiting M dwarfs, Kepler-45b (Johnson et al., 2012), NGTS-1b (Bayliss et al., 2018), HATS-71b (Bakos et al., 2018), and TOI-1899 (Cañas et al., 2020).

While exoplanet occurrence rates are important to the understanding of planetary formation and evolution theories, the information imparted by transiting exoplanets to the light curve of its stellar host is fundamental to the measurement of exoplanet physical properties. The degree to which an exoplanet blocks stellar flux during transit, i.e. the primary and deepest modulation in the stellar light curve, is indicative of its radial size. The repeat of flux loss with time is a measure of exoplanet orbital period. In turn, derived physical attributes thus support the tallies of exoplanet occurrence rates.

Transiting exoplanets are important probes of stellar surfaces. The surface activity of solar-type stars is of particular interest in the understanding of the Sun's dynamo. A probing exoplanet reveals new information on stellar magnetism. Secondary, small modulations in stellar flux due to the occultation of magnetic regions during transit are key to the assessment of magnetic activity created by the dynamo at play in solar-type stars. Dynamo models are based on observation of the cyclic activity of the Sun. They are mathematical expressions of the turbulent flow of electrically conducting plasma that amplifies magnetic fields via induction and maintains those fields against Ohmic dissipation (Charbonneau, 2020). In addition to addressing the large-scale regeneration of the Sun's magnetic field in accordance with observed solar cycles, solar dynamo models must also describe the small-scale dynamics and surface emergence

of sunspots. Examination of the magnetic activity in solar-type stars provides observational constraints on magnetohydrodynamic theory and magnetic field generation. An understanding of the magnetic activity of solar-type stars is the foundation of a stellar-solar connection.

In the current transit era, the search for exomoons remains at the forefront of exoplanetary research. With the thousands of known exoplanets and number of new exoplanets added weekly, it is only reasonable to assume that some have exomoon companions. Methodologies, including transit timing variations, pulsar timing, and microlensing, for finding exomoons have not yet yielded a confirmed detection (Heller, 2018). High precision transit photometry can contain the signs of exomoon presence. Stellar flux modulations due to the presence of an exomoon companion are distinguishable from those caused by changes in the stellar magnetic field. While starspots and faculae will only produce short modulations during transit as they are occulted by the exoplanet, exomoons should be characterized by longer flux changes both during transit and outside of transit. Just as planetary orbital period is bounded by the time between consecutive transits, exomoon orbital period is quantified by periodic flux modulations not due to starspots.

In comparison to exoplanet transits, smaller, secondary modulations in stellar flux are key to 1) the evaluation of magnetic activity created by the dynamo at play in solar-type stars and 2) the discovery of exomoons. In the former case, exoplanets act as probes of the stellar surface, marking regions of activity as they traverse stellar faces. Derived radial sizes and longitudinal positions of starspots and faculae open a window onto the dynamo activity in solar-type stars, thereby providing for evaluation of a solar-stellar connection. Does an internal dynamo generate starspots and faculae in the photospheres of cool main-sequence stars as it does on the Sun? Is the differential rotation profile of solar-type stars, measurable from the temporal change in the longitudes of magnetic phenomena, similar to that of the Sun's?

In the latter case, secondary stellar flux modulations due to the presence of an exomoon companion may be distinguished from those caused by changes in the stellar magnetic field. While starspots and faculae will only produce modulations when they

are occulted by during the transit of an exoplanet, exomoons can be evidenced by flux changes both during transit and outside of transit. Understanding the intricacies of transit light curves will shed new light upon exomoon discovery.

And so, this thesis embarks upon a study of transit light curves and the physical dynamics shaping them, with particular focus on the exemplary photometry from the *Kepler* mission. From stellar activity to exomoon orbits, it is all in the light curves.

1.1 Photometric Time Series of Transiting Exoplanets

Just as the moon blocks light from the Sun during a solar eclipse, an exoplanet crossing the face of its stellar host occludes light seen by an observer. While protected human eyes may observe an eclipse first-hand, direct observation of exoplanets in distant systems is extremely difficult, and transit detection requires a telescope with specialized instrumentation. Telescopes are designed to provide the sensitivity needed to detect the periodic dimming of stellar light, which can be as small as 0.01% of the total stellar flux for Earth-sized exoplanets and as large as 1% for Jupiter-sized planets transiting a solar-like star [2].

1.1.1 The Transit Light Curve

A light curve is simply a compilation of stellar flux measurements over a period of time. Stellar variability produces small, irregular modulations in the light curve, while a transiting exoplanet causes a characteristic u-shaped dip, signaling a transit light curve. Fig. 1.1 depicts a transit of the Earth-sized planet K2-28b about a mid-M dwarf observed by the Spitzer Space Telescopes on February 11, 2017. The black dots and vertical black bars represent observed data with errors. The red u-shaped curve is the transit fit to observed data.

The primary components of a transit, ingress, egress, and duration, are defined temporally. As shown in Fig. 1.2, points 1 and 2 demarcate the ingress of the planet onto a stellar face, represented by the large circle of radius R_*. The corresponding left wall

[2] https://www.nasa.gov/kepler/overview/abouttransits

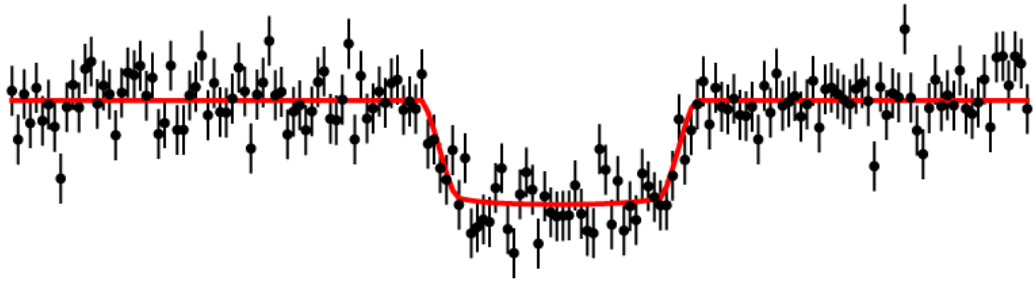

Figure 1.1: Observed flux data (black points with error bars) for K2-28b from the Spitzer Space Telescope on February 11, 2017 demonstrate a u-shaped decrease due to the planet's transit. The smooth red curve represents a light curve fit to the data. `https://iopscience.iop.org/article/10.3847/1538-3881/aabd75`, retrieved 30 September 2020

of the transit well is negatively sloped during partial eclipse. Egress from the stellar surface occurs between points 3 and 4, with the transit wall positively sloped during partial eclipse. Limb darkening will smooth the transitions at points 2 and 3 due to the gradual decrease in perceived stellar brightness from the maximum at the stellar center outward to the stellar limbs.

Planet radius is calculated from the transit depth, ΔF, as given by the ratio of the areas of the planet and star.

$$\Delta F = \frac{R_p^2}{R_*^2} \tag{1.1}$$

The greater the planet's radius with respect to the stellar radius, the greater the transit depth. The ability to detect exoplanets is dependent on the relative radial dimensions of the star and planet. To detect a 1% reduction in stellar flux, the planet's radius must be no smaller than one-tenth of the star's radius. Thus, the bigger the planet and the smaller the star, the better the chance of observing transits. M dwarfs are excellent target stars for transit detection given their small radii.

From point 2 to point 3, in Fig. 1.2, the planet is completely over the stellar surface for time t_F. During that time, the transit well is deepest. The time between points 1 and 4 is the total transit duration t_T.

The transit times above are expressed mathematically in terms of the star and planet radii, R_p and R_*, the semi-major axis, a, the inclination of the planet's orbit relative

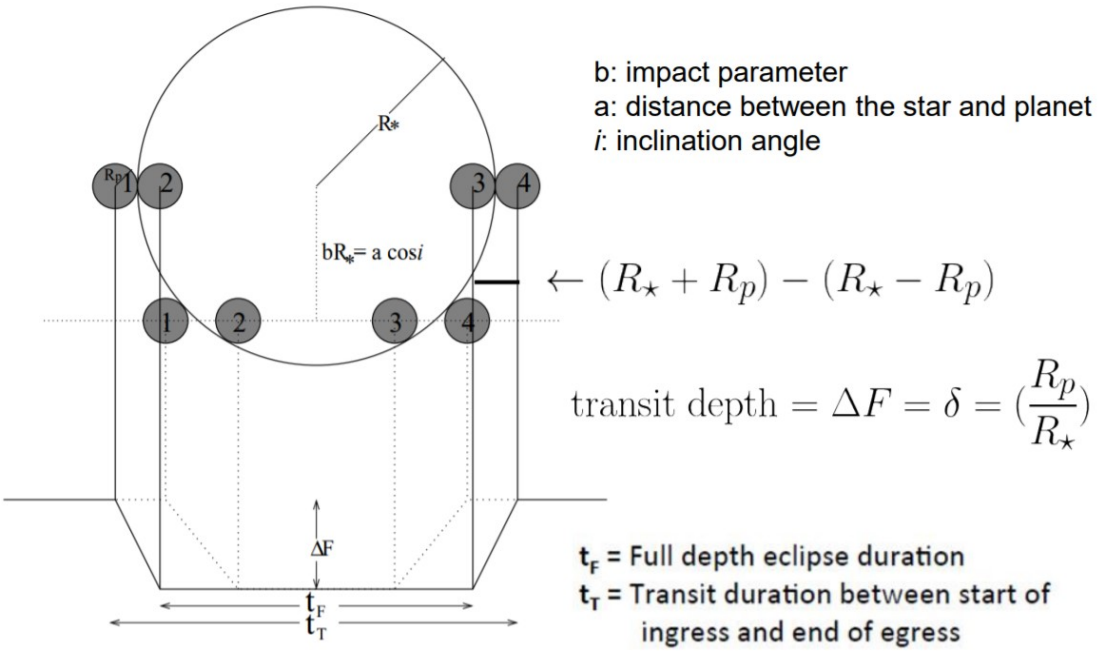

Figure 1.2: The transit of a planet (gray disk) across a stellar face (open circle) has measurable features. Points 1 and 2 mark the ingress of the planet across the stellar limb, while points 3 and 4 mark the egress across the opposing limb. The full transit duration equals the time between points 1 and 4, t_T. Between points 2 and 3, the planet is completely over the stellar face during time t_F. `http://www.astro.utoronto.ca/~astrolab/files/Lecture_Lab5_TransitPlanets-LightcurveAnalysis_2018-2019.pdf`, retrieved 2 October 2020

to the stellar rotation axis, i, and the planet's orbital period, P_{orb}. Assuming that the semi-major axis is much greater than the stellar radius and the inclination of the planet's orbit is close to 90°, the total transit duration is (Seager & Mallén-Ornelas, 2003)

$$t_T = \frac{P_{orb} R_*}{a\pi} \sqrt{(1 + \frac{R_p}{R_*})^2 - (\frac{a}{R_*} \cos i)^2} \tag{1.2}$$

The ratio between t_F and t_T is expressed as (Seager & Mallén-Ornelas, 2003)

$$\frac{t_F}{t_T} = \sqrt{\frac{(1 - \frac{R_p}{R_*})^2 - (\frac{a}{R_*} cos i)^2}{(1 + \frac{R_p}{R_*})^2 - (\frac{a}{R_*} cos i)^2}} \tag{1.3}$$

Impact parameter b is the sky projected distance between the planet and star at closest approach. Transit depth ΔF reflects the radial dimension of the planet relative to that of the star. Variations in the physical parameters of the star-planet system alter the composite shape of a transit. Transit times t_T and t_F change with the star-planet distance, or orbital semi-major axis. As the distance increases, the times shorten (and thereby the corresponding transit widths) and vice versa. In addition to the transit depth's relation to planet radius in terms of the stellar radius, R_p/R_*, transit shape is also dependent on the inclination of the planet's orbit relative to the stellar rotation axis. As the planet's inclination decreases, the transit becomes shallower and narrower with longer ingress and egress times. Transit depth is maximum when the planet's orbit is orthogonal to the stellar rotation axis.

Projected exoplanet latitude and longitude on the observed stellar face are also derived from star-planet parameters. Latitude is calculated from the same physical elements that determine the transit chord, as defined by the transit impact parameter, or the sky projected distance between the stellar and planetary centers at conjunction. In terms of the inclination of the planetary orbital plane, i, the planet's orbital semi-major axis, a, and the stellar radius, R_*, the transit impact parameter, b, is

$$b = \frac{a}{R_*}\cos(i) \tag{1.4}$$

In turn, transit latitude is given by

$$lat_{tran} = \arcsin\left[\frac{a}{R_* \cos(i)}\right] \tag{1.5}$$

For $b = 0$, the planet crosses the stellar equator. As the transit latitude nears the poles, b approaches 1. Impact parameter, and therein transit latitude, determines transit chord length and thus the transit duration.

The observed meridian of an exoplanet in a circular orbit about a stationary star changes with transit epoch and as such is dependent on the exoplanet's orbital period. Longitude defined with respect to 0° stellar topocentric longitude, which corresponds

to the middle of the planet's projection onto the stellar face at t= 0, is given by

$$\mathrm{lon_{tran}} = \arcsin\left[\frac{\mathrm{a}\cos\left(90^\circ - \frac{360^\circ\ \mathrm{t_{epoch}}}{24\ \mathrm{P_{orb}}}\right)}{\cos(\mathrm{lat_{tran}})}\right] \tag{1.6}$$

where $\mathrm{P_{orb}}$ is the orbital period, $\mathrm{lat_{tran}}$ is the transit latitude, and $\mathrm{t_{epoch}}$ is the transit epoch.

1.1.1.1 Elliptical Orbit Considerations

The orbits of many exoplanets have circularized due to tidal interactions resulting in a relatively fixed star-planet distance. For planets in elliptical orbits, the star-planet distance is variable. The elements of an elliptical planetary orbit are shown in Fig. 1.3. The semi-major axis of the ellipse and the distance from the star to the planet are and r, respectively. Angle Ω is the measure from the ascending node to the reference direction. The true anomaly, ν, is the angle between the planet's position and periastron (or periapsis) of the orbit. The angle of periastron, ω, is defined as the angle between the ascending mode periastron (or periapsis) measured clockwise in the orbital plane. A vector pointing from the focus of the orbit to apoapsis, or the eccentricity vector, has scalar magnitude e. This vector defines the direction from which the planet's location may be measured. The x and y vector components in terms of ω are

$$\mathrm{x} = \mathrm{e}\cos\omega \tag{1.7}$$

$$\mathrm{y} = \mathrm{e}\sin\omega \tag{1.8}$$

The star-planet distance is a function of the orbital eccentricity, e. As per Kepler's Law of Orbits, the distance varies from a(1+e) to a(1-e). In terms of a, e, and the planet's angular position with respect to periastron, ν, the star-planet distance, r, is

$$\mathrm{r} = \frac{\mathrm{a}(1 - \mathrm{e}^2)}{1 + \mathrm{e}\cos\nu} \tag{1.9}$$

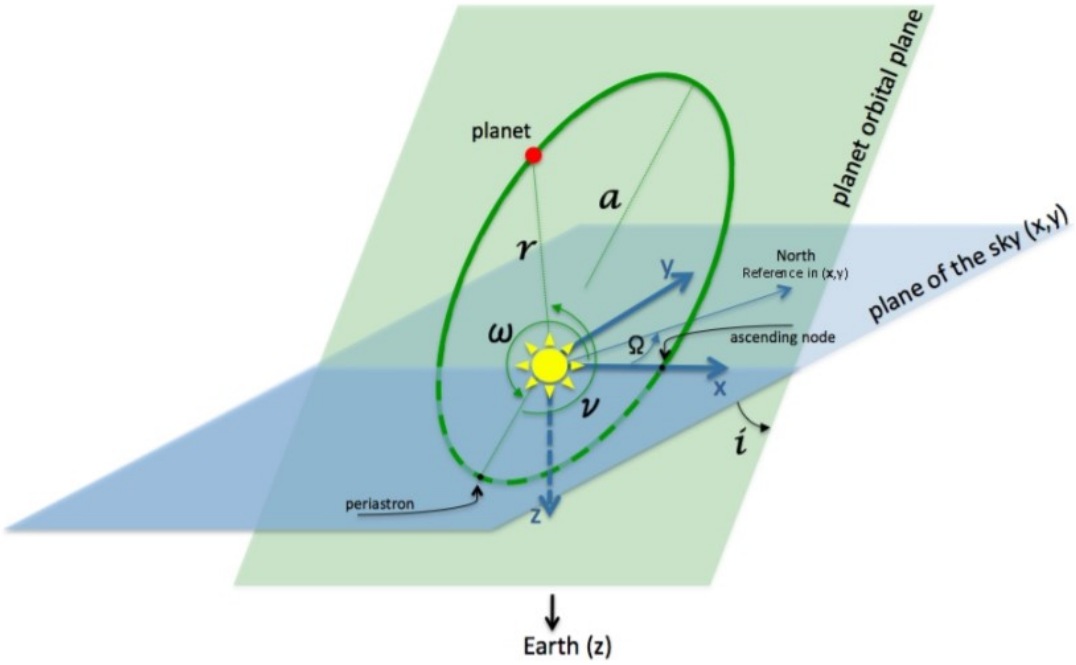

Figure 1.3: A planet (red) is in elliptical orbit about a star (yellow). The star-planet distance, r, varies with eccentricity. Orbital orientation is determined by the inclination of the orbital plane i, the ascending node Ω, and the angle of periastron ω. True anomaly, ν, is the angle between the planet's position and periastron. `https://www.astro.ex.ac.uk/people/alapini/Publications/PhD_chap1.pdf`, retrieved 24 June 2021

The angle of periastron, measured from the planet's ascending node to periastron, affects the planet's observability. At mid-transit, $\nu + \omega = \pi/2$, and star-planet distance is

$$r_{mt} = \frac{a(1-e^2)}{1+e\sin\omega} \tag{1.10}$$

It is generally assumed that this distance does not vary considerably during transit and as such is treated as the star-planet distance over time period t_T.

Ellipticity of a planet's orbits affects observed transit duration. While transit duration for circular orbits is fixed given constant orbital velocity, varying planet velocity from periapsis to apoapsis of elliptical orbits shortens or lengthens observed transit duration. The ratio between transit duration for circular and elliptical orbits is (Burke,

2008)

$$\frac{T_{ecc}}{t_T} = \frac{\sqrt{1-e^2}}{1+e\cos(\omega - 90^\circ)} \tag{1.11}$$

where T_{ecc} is the transit duration for a planet in an elliptical orbit. t_T is defined by Equation 1.2.

The position of the planet during its orbit is evaluated via Kepler's time dependent equation of motion

$$E - e\sin E = M \tag{1.12}$$

where E is the eccentric anomaly, or the angle between the ellipse center and the project of the planet's position on the great circle encasing the ellipses and M is the mean anomaly, which has the dimensions of an angle to represent the time since last periapsis. The eccentric anomaly is written as a function of e and ν as

$$E = 2\arctan\left[\sqrt{\frac{(1-e}{1+e}}\tan\frac{\nu}{2}\right] \tag{1.13}$$

In terms of the planet's mean motion, M is re-expressed as

$$M(t) = n(t - t_0) \tag{1.14}$$

where n is the mean motion, t_0 is the time of periastron passage and t is the time since periastron passage.

Solutions to Equation 1.12 are usually computed numerically by methods such as Newton-Raphson (Murray & Correia, 2011). Observations provide parameters for the computations, such as eccentricity and angle of periastron from radial velocity measurements.

1.1.2 False Positive Transits

As exoplanetary transits are observed over time, reductions in flux will repeat at an interval commensurate with the planet's orbital period. Other sources mimicking exoplanet periodicity, such as instrumental effects, eclipsing binaries, or transits of stars aligned with or bound to the target star, often cause false positives (Santerne et al., 2013; Deeg & Alonso, 2018). Elimination of false positives may be achieved via supplemental photometric observation, and/or the combination of photometric data with data from other detection methods such as radial velocity, which can identify stellar objects by their spectral lines. The identification of eclipsing binaries often warrants other analysis, such as the comparison of light curves recorded in different bandpasses or transit light curve fitting (Deleuil et al., 2018). Certain stellar configurations may result in the observation of grazing binaries or secondary-only eclipses. These eclipses resemble the short duration, V-shaped transits of exoplanets with high impact factors but do not display the limb darkening effects associated with planetary transits. Comparison with simulated transit light curves of a planet is one method by which an eclipsing binary may be identified (Santerne et al., 2013).

1.1.3 Transit Detection Probability

Critical to the observation of transits is the orientation of an exoplanet's orbital plane to the rotational axis of its host star. The planet must also orbit close to the observer's line-of-sight (LOS) (see Fig. 1.4). The geometric probability of observing a transit is defined by the angle about the LOS given as ratio of the stellar diameter to the radius of the planet's orbit. Assuming that the planet's orbit is circular and coplanar with the stellar equator (the orbital inclination is equal to the stellar inclination), the orbital pole, or orbital plane, of the planet must be within an angle of $d^*/D/2$ perpendicular to the LOS, where d^* (or $2R_*$)is the stellar diameter and D/2 is the semi-major axis of the planet's orbit (or a). This is true for all pole positions about the LOS within the total solid angle of $4\pi d^*/D$ steradians (Borucki & Summers, 1984).

Geometric probability decreases with increasing planet distance from its host star.

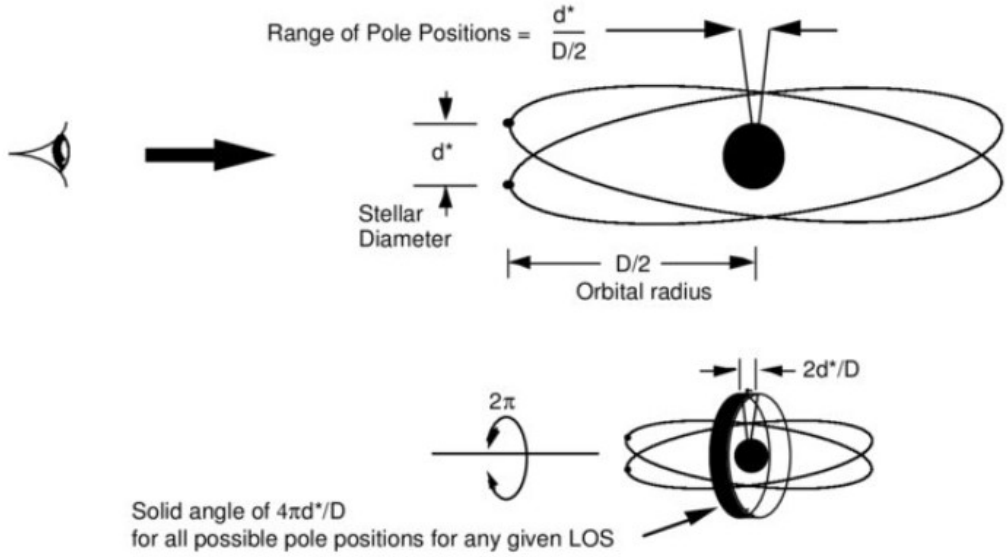

Figure 1.4: The probability of observing transits is dependent on the geometry of the star-planet system. The viewing angle relative to the line-of-sight is determined in terms of the stellar diameter, d^*, and the semi-major axis of the planet's orbit, D/2. (Borucki & Summers, 1984).

For a hot Jupiter orbiting its host at a distance of 0.05 au, the probability of detecting transits is 10%. An Earth-sized planet orbiting at 1 au would have a detection probability of 0.5% (Deeg & Alonso, 2018). However, when the stellar inclination is allowed to vary within $90° \pm 5°$, the probability increases to 74.8% for a Jupiter-sized planet and 4.25% for an Earth-sized planet (Beatty & Seager, 2010).

1.1.4 Transit Photometry from the Kepler Mission

The primary goal of the *Kepler* mission was the discovery of Earth-sized planets orbiting in the habitable zones of solar-type stars (Borucki et al., 2003). From March 2009 to May 2013, the *Kepler* telescope stared at more than 150,000 stars in a 115 square degree field-of-view in the Cygnus-Lyra region as shown in Fig. 1.5. At the heart of the Kepler spacecraft was a photometer comprised of an array of 21 charge-coupled device (CCD), each containing two 2200x1024 pixel CCDs covering 5 square degrees of the sky. Pixel counts are read out every 3 seconds and integrated over 29.42 min for

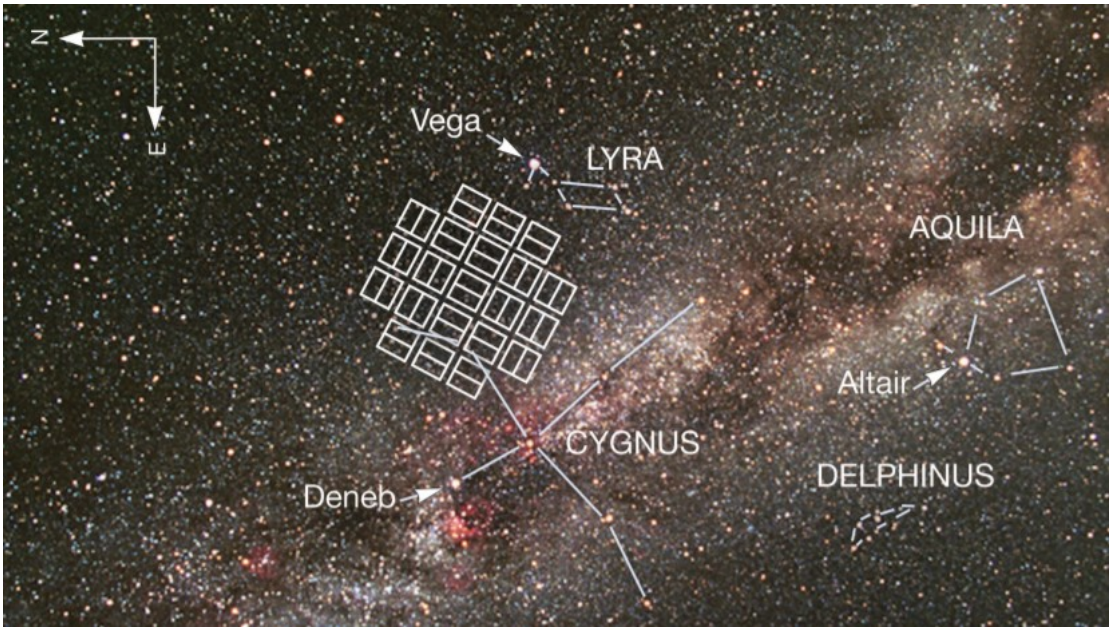

Figure 1.5: The 115 square degree view of the *Kepler* telescope in the Cygnus-Lyra region, marked by rectangles representing detectors. `https://www.nasa.gov/pdf/189566main_Kepler_Mission.pdf`, retrieved 15 October 2020

long cadence (LC) targets and 58.85 s for short cadence (SC) targets and downloaded monthly (Gilliland et al., 2010; Jenkins et al., 2010). Data in both modes are available as raw pixel data, or Simple Aperture Photometry (SAP) flux, and as Pre-Search Data Conditioning Simple Aperture Photometry (PDCSAP) flux corrected by the Kepler pipeline to remove instrumental effects and sky background artefacts from the data (Jenkins et al., 2010; Smith et al., 2012; Stumpe et al., 2012, 2014).

Data from the Kepler mission was made publicly available as the Kepler Objects of Interest (KOI) Catalog stored in the NASA Exoplanet Archive database [3]. The final catalog, Data Release 25 (DR25), was issued in August 2017. It contains the results of the ultimate Kepler Data Processing Pipeline, SOC 9.3, search for transiting exoplanets for all Kepler quarters Q1 - Q17, 3 month periods spanning 13 May 2009 - 9 December 2013 (Twicken et al., 2016). In addition to DR25 light curve data, the NASA Exoplanet Archive contains the properties of confirmed and candidate exoplanets, and stellar target parameters.

[3] https://exoplanetarchive.ipac.caltech.edu/cgi-bin/TblView/nph-tblView?app=ExoTbls&config=cumulative

The volume of collected data has supported the analysis of stellar behavior over a range of spectral types and ages, e.g. Reinhold et al. (2013); McQuillan et al. (2013, 2014); He et al. (2015); Mehrabi et al. (2017). LC data serves the analysis of large-scale trends, such as the periodicity and amplitude of light curve modulation due to magnetic activity, while SC data is useful for astrophysical studies and transit timing analysis (Murphy, 2012). As it will be shown, the detail in PDCSAP SC light curves also provides for the examination of magnetic phenomena in the photospheres of solar-type stars.

1.2 Starspots and Faculae

Starspots and faculae on stars other than the Sun are manifestations of dynamically driven magnetic fields, analogous to those observed on the Sun. Spots are regions of intense magnetic fields which are cooler than the surrounding photosphere and appear darker. Faculae are bright photospheric regions of lesser magnetic intensity around spots. The appearance of sunspots and faculae with solar rotation contributes to irradiance variability (Mehrabi et al., 2017). Maunder (1904) charted the emergence latitude of sunspots to show that new spots follow a pattern, emerging first at mid-latitudes and then progressively closer to the equator during an 11-year cycle. Spot coverage is least at solar minima, as spots form at mid-latitudes and decay at low latitudes. At solar maxima, solar irradiance peaks due to the appearance of abundant faculae. The Sun appears 0.1% brighter at solar maxima.

Stars also exhibit photometric variability due to starspot and facula coverage. Since the 1990's, several techniques have been employed to assess starspot physical characteristics and coverage (O'Neal et al., 1996). Neff et al. (1995) measured starspot area and temperature on active stars from synthetic spectra based on TiO absorption bands. Utilization of this technique is not restricted by stellar rotation period. The modeling of photometric light curves has been widely used but is limited to asymmetric spot distributions (Strassmeier et al., 1994; Olah et al., 1997). To resolve the degeneracy in spot configurations, light curve inversion is used to create an image of the stellar sur-

face (Messina et al., 1998). The measurement of spectral line asymmetries via Doppler Imaging provides better spatial information (Vogt et al., 1997). Doppler Imaging, however, is restricted to rapid rotators. Maximum-entropy imaging enhances Doppler Imaging by combining spectral line data with VRI photometry (Collier Cameron, 1986).

The magnetic activity cycles of solar-type stars may differ from that of the Sun (Nielsen et al., 2019). A knowledge of starspots augments the study of the stellar dynamo. While difficult to trace the latitudinal migration of starspots, the modulation of stellar irradiance due to starspots seen in long-term light curves as periodic, sinusoidal trends reflect magnetic activity cycles (Mehrabi et al., 2017). The periodicity can be used to measure mean stellar rotation rate (Reinhold et al., 2013; McQuillan et al., 2013, 2014). Light curves which include the effects of exoplanet transits provide the additional information needed to measure stellar differential rotation. Given the mean stellar rotation rate estimated from out–of–transit light curves and the rotation rate at the transit latitude as measured from the longitudes of starspots and faculae observed in-time along the transit chord, a differential rotation profile may be constructed. Basic questions drive the assessment of spots and faculae on extra-solar stars: Is the same internal dynamo active in the Sun also active in other stars? How do the rotation profiles of solar-type stars compare to that of the Sun? What are the activity cycles of other stars? Do starspots and faculae exhibit physical characteristics similar to those on the Sun?

1.2.1 The Solar Dynamo

The Sun's magnetic fields responsible for spot and faculae manifestation are cyclically generated by an organized, internal dynamo. During each cycle, sunspots of opposite leading polarity appear in each hemisphere from mid-latitudes towards the equator. At the commencement of a new solar cycle, sunspots emanate at latitudes near 40°. As the cycle progress towards solar maximum, sunspots appear at progressively lower latitudes. The greatest number of sunspots appear at low latitudes and cover up to 1% of the solar surface. Every 11 years, this pattern repeats with spot pairs of reversed

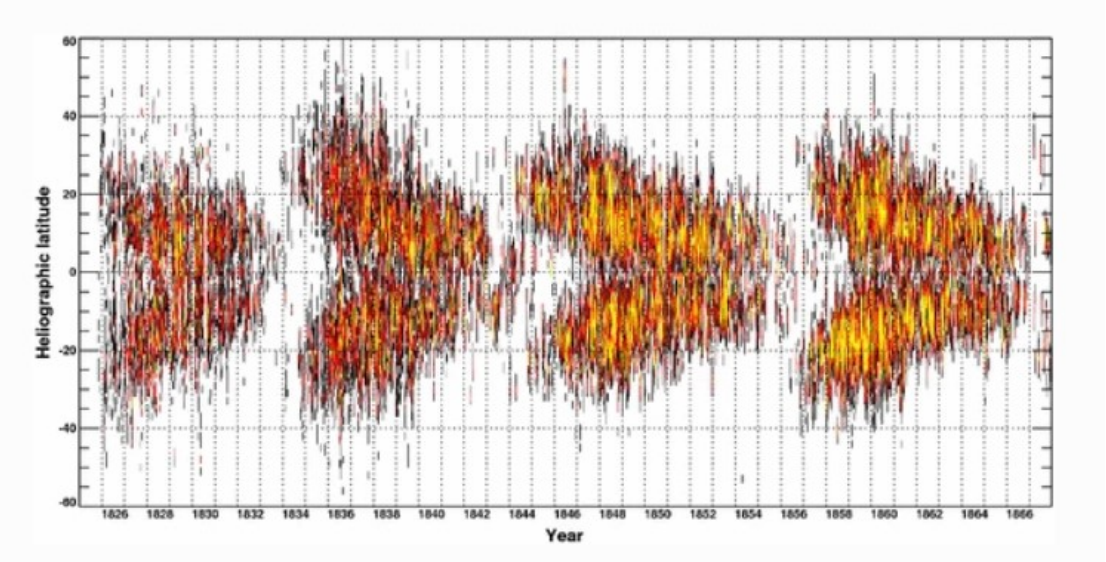

Figure 1.6: The latitude of emerging spots plotted for the years 1825-1867 depicts the butterfly pattern recognized by Maunder. `https://link.springer.com/article/10.1007/s41116-017-0006-9/figures/2`, Credit Arlt et al. (2013), retrieved 24 June 2021

magnetic polarities (Hale et al., 1919). The pattern is best recognized at the butterfly diagram of Maunder (1904), as shown in Fig. 1.6.

Solar dynamo models, such as the $\alpha\Omega$ model, are based upon observations of the Sun's activity (see Fig. 1.7).The source of magnetic fields is held to be the tachocline located deep in the convective zone where it meets the radiative zone. At that boundary, rotational shear acts upon electrically charged plasma flows to induce poloidal magnetic fields (Spruit, 2010; Charbonneau, 2014). Poloidal fields are then stretched about the stellar rotation axis and amplified by differentially rotating plasma forming toroidal fields (the Ω-effect). These fields are promoted to the surface via magnetic buoyancy and twisted into loops by the Coriolis effect (the α-effect) to appear as spots (Hubbard et al., 2011). As spots decay, meridional flow carries the strong magnetic fields once enclosed toward the poles. Polarity reverses and the dynamo cycle begins once again.

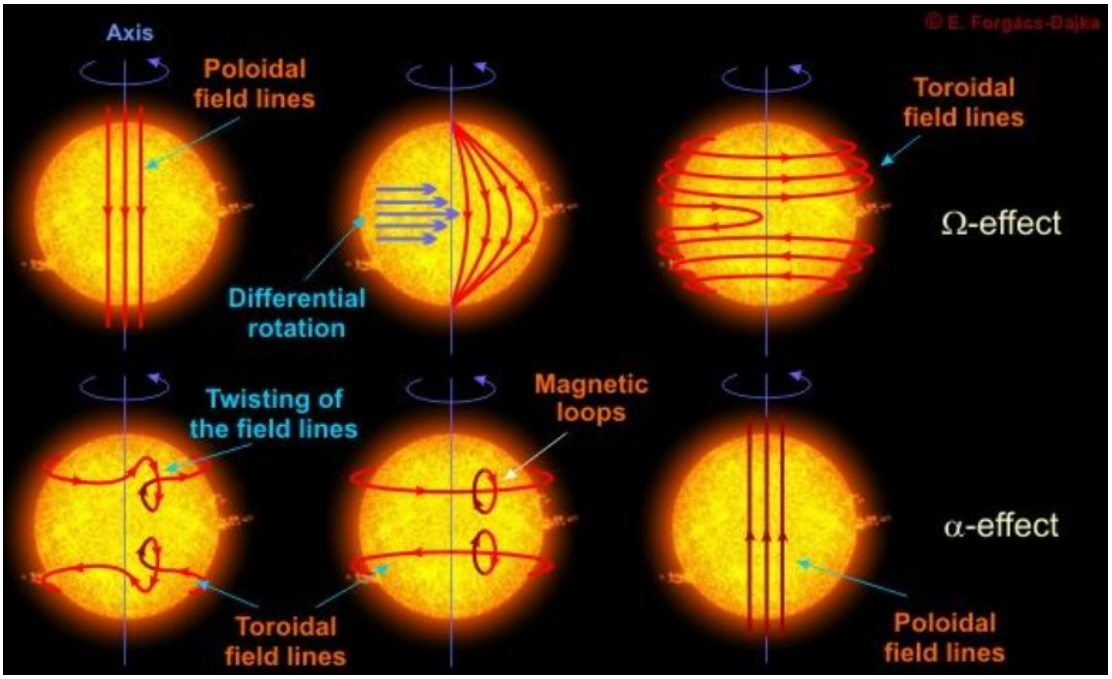

Figure 1.7: The α- and Ω-effects of the solar dynamo. Differential rotation wraps poloidal field lines into toroidal field lines (the Ω-effect). Rising toroidal field lines are twisted by Coriolis forces, resulting in spots. As spots decay, meridional flow carries the magnetic field toward the poles, regenerating poloidal field lines (α-effect). `https://www.crediblehulk.org/index.php/2017/01/12/the-solar-dynamo-the-physical-basis-of-the-solar-cycle-and-the-suns-magnetic-field`, Credit E. F. Dajka, retrieved 22 October 2020

1.2.1.1 Solar Differential Rotation

Long before the advent of helioseismology, the observation of sunspots indicated that the Sun rotates slower at the poles than at the equator. Helioseismology has provided measurements of the Sun's acoustic modes in proof of the different rotation rates in the outer radiative core and the layers of the convective envelope (Schou et al., 1998). This difference is theorized as the result of the interplay between rotation and convection (Kitchatinov, 2011). The Coriolis force deflects the convective flow of plasma fluid, and the plasma reacts by perturbing uniform rotation and creating subrotation regions. The resulting anisotropy is necessary for the outward transport of angular momentum.

Angular velocity varies with both radius and latitude (Howe, 2009; Matilsky et al.,

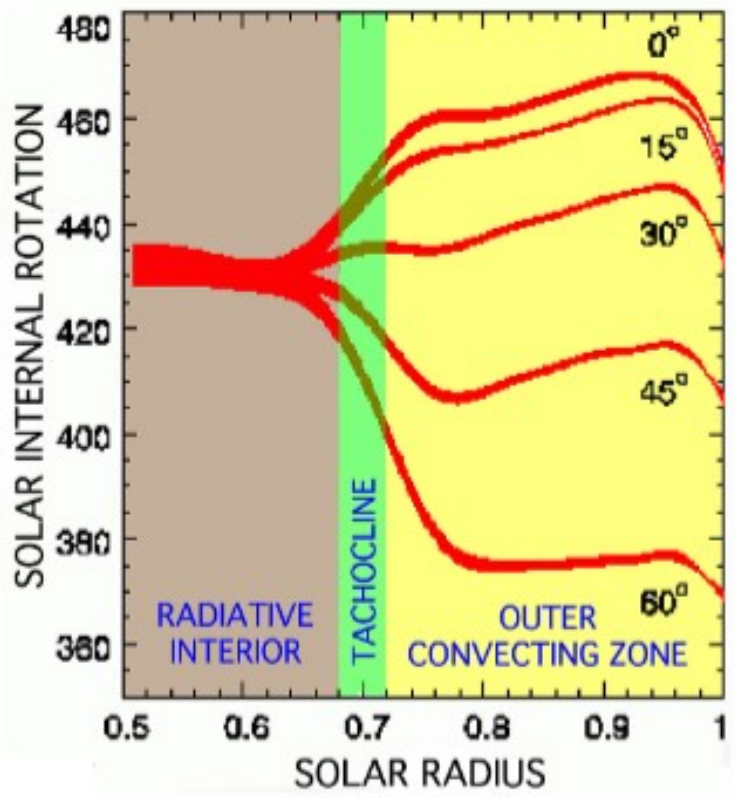

Figure 1.8: The tachocline forms a boundary between the rigidly rotating solar core and the differentially rotating convection zone. `https://www.researchgate.net/publication/259873333_Pattern_in_solar_variability_their_planetary_origin_and_terrestrial_impacts#fullTextFileContent`, Credit N. A. Morner, retrieved 16 July 2021

2020). A simplified solar differential rotation law expresses the change in angular velocity as a function of solar latitude by

$$\Omega(\alpha) = \Omega_{eq} - \Delta\Omega \ \sin^2(\alpha) \tag{1.15}$$

where Ω is the latitude dependent angular velocity, Ω_{eq} is the equatorial angular velocity, $\Delta\Omega$ is rotational shear, or the difference in angular velocity between the equator and pole, and α is solar latitude.

Fig. 1.8 depicts the divergence in solar rotation rate at the interface layer, or tachocline, between the rigidly rotating radiative zone and the fluid convection zone. The Sun's

internal rotation varies from approximately 450 nHz, or 35 days, at the equator to approximately 300 nHz, or 35 days, at the poles.

1.2.2 Stellar Dynamos and Starspot Latitudes

Though a solar-type dynamo may very well be the basis for the activity of solar-type stars, the expectation is that starspot emergence patterns on those stars will differ from that observed for the Sun. Latitudinal distribution of starspots is affected by stellar attributes, including rotation rate, and convection zone depth (Schüssler et al., 1996; Shapiro et al., 2014). These factors influence the trajectories of buoyant flux tubes from their origin at the tachocline to their breakthrough in the photosphere (Granzer, 2004).

The Rossby number is a widely used measure of magnetic activity strength for FGK and early-M stars. It expresses the ratio between observed stellar rotation rate and empirically derived convective turnover time based on stellar B-V color (Noyes et al., 1984). In other words, the Rossby number reflects the relative effect of the Coriolis force on flows in the convective plasma. The smaller the Rossby number, the greater the effects of rotation and the Coriolis force over inertial forces. Rapid stellar rotation results in a Coriolis force that dominates the buoyant force and deflects flux tubes to higher latitudes (Schüssler & Solanki, 1992; Granzer, 2004).

Granzer (2004) also investigated the relation between core size and starspot emergence patterns. He found that once the radius of the radiative core is less than 30% of the stellar radius, emergence latitude decreases directly with core size. Stars with masses $\leq 0.35 M_{\odot}$, such as late-M dwarfs, have lost their radiative cores and are fully convective. A distributed dynamo replaces the interface dynamo. Distributed dynamo simulations demonstrate the formation of starspots at high latitudes (Yadav et al., 2015) as well as at low and high latitudes simultaneously (Weber & Browning, 2016). Starspots have been observed at different latitudes (Barnes et al., 2017), but the

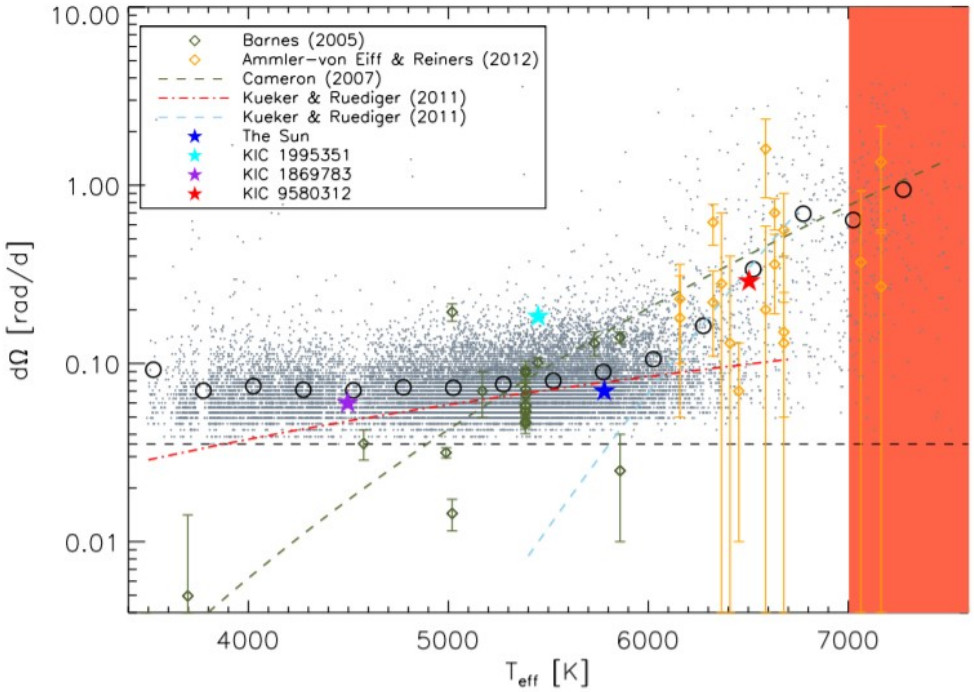

Figure 1.9: Measurements and theoretical predictions of horizontal shear agree that the dependence on stellar effective temperature is weak up to 6000 K and strong for hotter stars. `https://www.researchgate.net/publication/259873333_Pattern_in_solar_variability_their_planetary_origin_and_terrestrial_impacts#fullTextFileContent`, Credit Reinhold et al., 2013, retrieved 16 July 2021

mechanism of their emergence is not yet well understood (Weber & Browning, 2016).

1.2.2.1 Stellar Differential Rotation

Observation is required to assess the differential rotation of cool, solar-type stars for comparison with theoretical predictions and the modest differential rotation of the Sun. Options for measuring the different rotation of stars other than the Sun include asteroseismology, the relatively new equivalent of helioseismology that investigates the internal structure of stars which are not directly observable (Aerts et al., 2010) and calculating latitudinal rotation period from spectroscopic or photometric starspots. In the latter case, the difference between a star's mean stellar rotation as calculated via Lomb-Scargle analysis or autocorrelation of transit light curve data (McQuillan et al.,

2013, 2014), and a latitudinal period revealed by the movement of starspots yields an estimate of a star's differential rotation. Observation of starspots at multiple latitudes enhances the estimation of differential rotation and also allows mimicking of the butterfly diagram of the Sun (Netto & Valio, 2020). A pseudo-butterfly diagram will be temporally limited by observation time but can picture the latitudes at which spots emerge for stars of different spectral classes and ages.

Measurements of horizontal shear from the observation of active stars by Barnes et al. (2005), Ammler-von Eiff & Reiners (2012), and Reinhold et al. (2013) are summarized and plotted in relation to the theoretical predictions of Collier Cameron (2007) and Küker & Rüdiger (2011) in Fig. 1.9, as reprinted from Reinhold et al., 2013. The data are represented by gray dots, and olive and orange diamonds. The open black circles are the weighted means of of the Reinhold et al. (2013) measurements binned by temperature. The red dash-dot and blue dashed lines represent the trends predicted by Küker & Rüdiger (2011), whereas the olive dashed line represents the power law fit from Collier Cameron (2007). Both theory and observation agree on the weak dependence of horizontal shear on stellar effective temperatures up to 6000 K. Using mean-field models of outer convective zones for zero age main sequence stars, Küker & Rüdiger (2011) predicted two trends differential rotation with stellar effective temperature: a modest increase below 6000 K and a sharp increase above 6000K. Reinhold et al. (2013) confirmed these trends via the measurement of differential rotation for more than 18,000 stars in the *Kepler* field by correlating Lomb-Scargle periods from light curves of different *Kepler* quarters with a secondary period being within 30% of the primary rotation period. Their values of $\Delta\Omega$ generally fall between 0.03 and 0.20 rad d^{-1}, where the lower value was bound by observational limitations. The measurements of Ammler-von Eiff & Reiners (2012) show the scatter in $\Delta\Omega$ in the high temperature regime. The proposals of Barnes et al. (2005) and Ammler-von Eiff & Reiners (2012) to represent differential rotation as a function of effective temperature by a single power law does not address the discontinuity above 6000 K. Though not show by Fig. 1.9, the values from Reinhold et al. (2013) also exhibit the weak correlation of rotational shear and rotation rate proposed by Küker & Rüdiger (2011).

1.2.3 The Solar-Stellar Connection

Observation of the Sun has set the groundwork for describing the magnetohydrodynamic processes that generate time-dependent magnetic fields (Brun et al., 2014). Investigation of the magnetic activity of extra-solar stars will provide valuable benchmarks for solar dynamo theory. Any magneto-convective dynamo model such the solar $\alpha\Omega$ dynamo must explain the magnetic activity of stars with a radiative-convective internal structure (Hubbard et al., 2011; Isik et al., 2011; Shapiro et al., 2016). Due to the varying levels of magnetic activity exhibited by stars of different spectral types, rotation rates, and ages, solar-type stars, in particular cool stars, have become popular targets for observation since their dynamos are expected to produce activity patterns similar to the Sun's while still offering a broad view of magnetic activity. Much has already been learned about the activity of solar-type stars from chromospheric emissions, spectropolarimetry maps, asteroseismic data, and photometric analyses (Berdyugina, 2005; Brun et al., 2014). Skumanich (1972) established that magnetic activity of main sequence stars decreases as stellar rotation slows with age due to rotational braking. Dorren & Guinan (1982) found that starspots are present in active regions on solar-type stars. Barnes et al. (2005) and Reiners (2006) investigated the dependence of differential rotation on temperature as well as rotation and proposed that stellar effective temperature and surface differential rotation follow a direct relation. Reinhold et al. (2013) found that on cool stars (3000-6000 K), shear shows a weak dependence with stellar effective temperature. Shear increases significantly for temperatures above 6000 K, as predicted by (Barnes et al., 2005). From a photometric study of young, active late-F to mid-K stars, Lehtinen et al. (2016) noted that differential rotation is dependent on rotation period.

The template for assessing the magnetic activity of solar-types stars comprises the features observed for the Sun:

- starspot and faculae appearance, coverage, lifetimes, and temperatures
- active longitudes
- differential rotation

- activity cycles

Comparison of observed attributes for stars of different effective temperatures, masses, and convection zone depths will determine whether the solar dynamo model is indeed the common foundation for describing the behavior of solar-type stars across spectral classes. Similarities among stars and the Sun will enhance the solar-stellar connection, while differences will offer new constraints for solar dynamo theory.

1.2.4 The Study of Magnetic Activity

Starspots and faculae are proxies of magnetic activity, and their observation is thus critical to establishing a solar-stellar connection. The techniques of Doppler Imaging (DI) and Zeeman Doppler Imaging (ZDI) have been widely used to map areas of magnetic activity on the stellar surface (Vogt & Penrod, 1983). DI maps are constructed via inversion of the spectral line profiles of rapidly rotating stars. Starspots appear as bumps moving longitudinally with stellar rotation in a series of rotationally broadened line profiles. Light curve inversion methods applied to the line profiles return longitude information when degeneracies can be resolved but are less reliable for latitude determination (Roettenbacher et al., 2017, and references therein). ZDI maps of large-scale magnetic fields on stellar surfaces are derived from spectropolarimetric data (Semel, 1989). Spectral line polarizations for four Stokes parameters from a series of rotational phases are inverted to create a picture of magnetic field distribution (Berdyugina, 2005, and references therein). While both techniques are useful for assessing stellar differential rotation, they present limitations when studying solar-type stars across spectral classes: targets are limited to moderately and rapidly rotating active, bright stars; and small-scale starspots on cool stars cannot be detected due to their low brightness (Iliev, 2010; Kochukhov et al., 2017).

Several photometric techniques that are not limited by stellar rotation rate and magnitude have been employed in the study of spotted stellar light curves. These include Lomb-Scargle periodograms (Reinhold et al., 2013) and phase tracking (Davenport, 2015) to estimate surface differential rotation, and starspot modeling Silva (2003). The first two methods address broad photometric trends in long cadence *Kepler* photom-

etry, while the latter is focused on the physical characteristics of individual starspots found in short cadence *Kepler* photometry. Starspot physical properties include radial size, longitude, intensity, and temperature. Starspot latitude is the projected latitude of the transiting planet. Modeling of magnetic features in individual transit light curves also applies to the assessment of facular properties. Starspot and facula information obtained from long-term transit observation allows for mapping of the stellar surface and assessment of magnetic activity cycles. For low obliquity orbits, measurement of stellar rotation at the transit latitude and differential rotation is possible when a planet crosses the same magnetic features over successive transits.

1.2.4.1 Modeling Magnetic Features

The stellar surface is a dynamic skin, changing with the ebb and flow of magnetic fields. Transit light curves are snapshots of activity in the photosphere taken each time a planet crosses the visible photosphere at a latitude dictated by the planet's orbital inclination and distance to the star. The picture of a uniform, unspotted photosphere is a u-shaped curve. When a transiting planet occults regions of suppressed brightness (starspots) or enhanced brightness (faculae) due to magnetic activity, distinct variations appear in the light curve. As shown in Fig. 1.10, the TrES-1 transit light curve has a distinct bump indicative of the occultation of a dark starspot or starspot group, while the HD209458 transit light curve reflects a uniform photosphere.

Faculae, which are brighter than the photosphere, appear as dips in normalized flux (= 1) when compared to the model light curve of an unspotted photosphere. The example transit for Kepler-71 in Fig. 1.11 depicts the flux modulations due to a starspot and faculae relative to the light curve model for a spotless photosphere.

The model light curve for an unspotted photosphere, such as that shown by the red curve in Fig. 1.11, can be generated from host star-planet system parameters: stellar radius, and planet radius, orbital period, inclination, and semi-major axis. This requires preliminary use of a sampling algorithm to fit planet parameters to the average of phase-folded transits that have been polynomial detrended and normalized. Averaging reduces data noise and removes starspots/faculae, thereby removing light curve

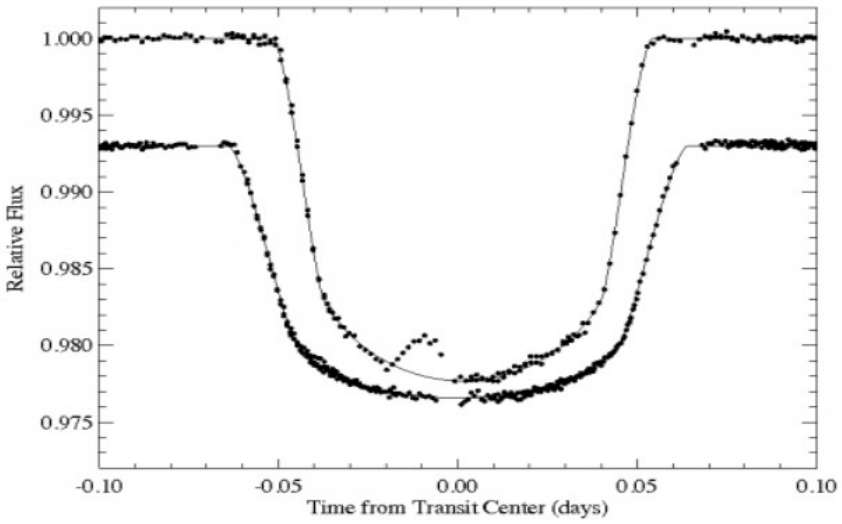

Figure 1.10: The HD209458 light curve (lower) is unspotted, while the TrES-1 light curve (upper) has the signature of a starspot left of mid-transit. (Charbonneau et al., 2007) `https://www.paulanthonywilson.com/the-transit-light-curve/`

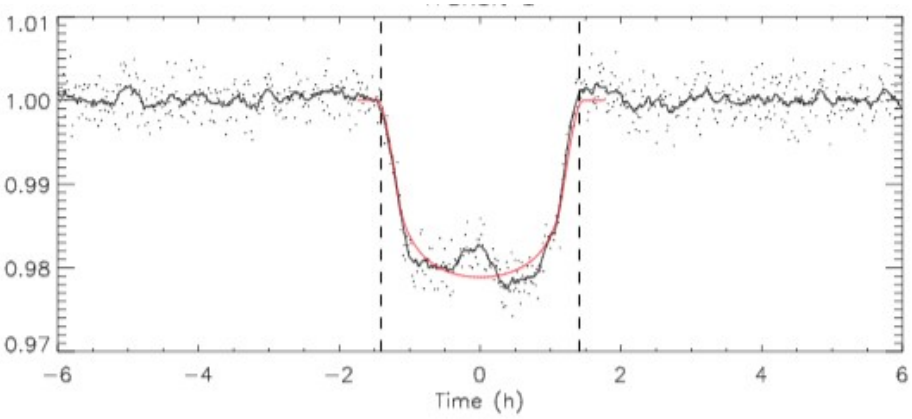

Figure 1.11: An observed light curve (smoothed data in black) for Kepler-71 shows one potential starspot signature at 0 h and two potential facular signatures at approximately -1.0 h, and +0.8 h from transit center. The red curve is a transit model for an unspotted photosphere. (Zaleski et al., 2019)

variations which may effect parameter optimization.

In the implementation of Silva (2003) for modeling transit light curves, which is used in the studies of Kepler-71 and Kepler-45 presented in Chapters 2 - 4, the star is defined as a limb darkened white light image, and the planet is a dark disk in a circu-

lar orbit. The disk radius and orbital characteristics orbit are described by optimized parameters. The planet's position in front of the star is calculated in predefined time steps. The planet's projection traverses the stellar face along the transit chord, which is a fixed latitude given by Equation 1.5. Longitude varies with transit epoch, as given by Equation 1.6.The stellar flux at each step is calculated as the sum of all points in the stellar image, including those occluded by the planet. The total flux increases when a spot is occulted because the planet is crossing a dark region rather than the bright photosphere. The resulting light curve is symmetric about mid-transit (t = 0).

Starspots and faculae are modelled by overlaying disks of varying size and intensity on the stellar image. They are added to the model light curve for an unspotted photosphere generated from optimized system parameters. Starspot and faculae radii and intensities are inferred from the widths and amplitudes of flux variations. Their stellar topocentric longitudes relative to 0°, which is the center of the projection of the planet onto the stellar disk at mid-transit (t = 0), are estimated from the time corresponding to their centers and calculated by

$$\mathrm{lon_{sf}} = \arcsin\left[\frac{\mathrm{a}\cos\left(90^\circ - \frac{360^\circ\ \mathrm{t_{sf}}}{24\ \mathrm{P_{orb}}}\right)}{\cos(\mathrm{lat_{tran}})}\right] \tag{1.16}$$

where $\mathrm{t_{sf}}$ is time corresponding to the starspot/facula center and $\mathrm{lat_{tran}}$ is given by Equation 1.5.

Fitting of spotted light curves created by this star-planet model to observed light curves has been successfully used to analyse starspots on many stellar targets, including CoRoT-2 (Silva-Valio & Lanza, 2011) and Kepler-17 (Valio et al., 2017). Those studies employed the χ^2 minimization routine *AMOEBA* (Press et al., 1992) to fit physical parameters. While *AMOEBA* is able to fit physical parameters, it is limited by an inability to provide parameter measurement errors. Probabilistic data analysis of model parameters has succeeded earlier mathematical methods. Markov Chain Monte Carlo (MCMC) algorithms are now employed for fitting since they return median values physical parameters with uncertainties.

All model light curves, whether for transits of a uniform and seemingly inactive or active photosphere, may be fit to observed data via an MCMC sampler to obtain a priori values for starspot/facula parameters. MCMC samplers employ Bayesian inference to return probable parameter solutions with uncertainties from probability distributions given physically reasonable prior information. In particular, the affine-invariant ensemble sampler for MCMCs, *emcee*, introduced by Goodman & Weare (2010) and implemented in Python by Foreman-Mackey et al. (2013) is computationally economical. This algorithm efficiently selects different combinations of parameter values as it moves through parameter space. At each move *emcee* calculates the likelihood of a transit light curve built according to a generative function such as the model of Silva (2003). The sampler returns parameter statistics as median (50%) values of parameter samplings, with lower and upper 1-σ errors corresponding to the 16% and 84% quantiles (Hogg & Foreman-Mackey, 2018).

A catalog of starspot/faculae parameters and their errors is created by fitting spotted light curves unique to each observed transit. The number of magnetic features modeled is inferred from observed data and varies from transit to transit, some transits having no flux variations discernible as magnetic features. During the fitting process, only starspots/parameters are free to vary. The underlying, optimized system parameters remain unchanged. Once complete, the catalog is an invaluable resource for analysing stellar magnetic activity.

1.2.4.2 Mapping Magnetic Features

Snapshots of starspot and facula longitudes at the transit latitude may be compiled into 360° longitude maps of the stellar surface for a given rotation period. For each *Kepler* day of observation, longitudes are transformed from the topocentric frame of the observer to one that rotates with the star. Magnetic features are then temporally stacked, as shown in Fig. 1.12 for Kepler-17 activity (Valio et al., 2017). The size and shading of starspots represent relative radius and intensity. The total flux deficit vs longitude is plotted under the map.

Longitude maps are an important tool for diagnosing stellar differential rotation

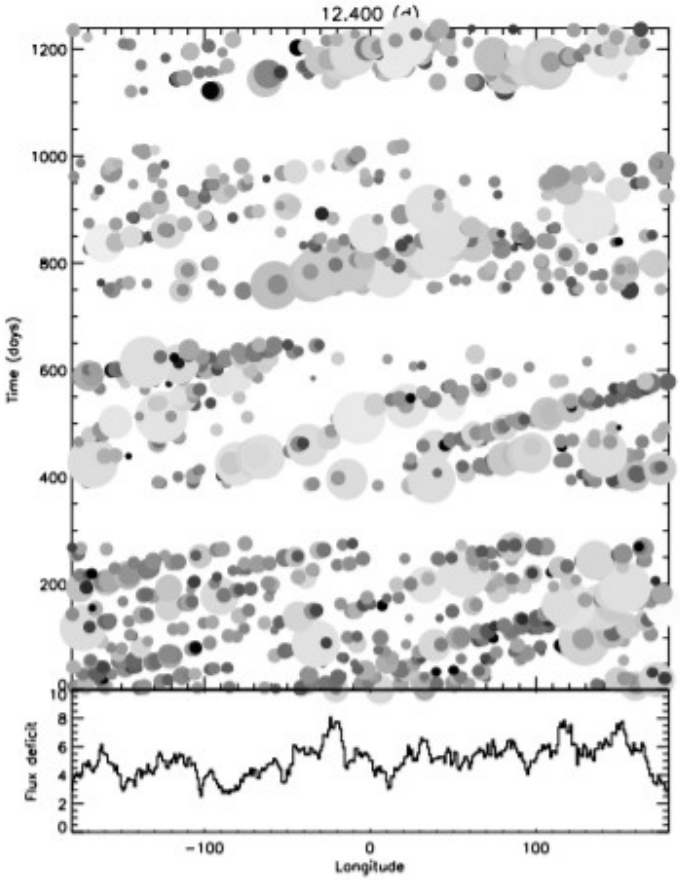

Figure 1.12: A longitude map of starspots on Kepler-17 at the mean stellar rotation period of 12.40 d shows diagonal alignment indicative of different rotation rate at the transit latitude. The size and shading of starspots represent relative radius and intensity. The bottom panel depicts the total flux deficit at each longitude. (Valio et al., 2017)

and active longitudes. Non-vertical spot alignment is symptomatic of rotation rate changing as latitude increases towards the stellar poles. As observed for the Sun, rotation rate is greater at the equator than at the poles. This is described by the following simplified solar differential rotation law.

$$\Omega(\alpha) = \Omega_{eq} - \Delta\Omega \ \sin^2(\alpha) \tag{1.17}$$

where Ω is the angular velocity at latitude α, Ω_{eq} is the equatorial angular velocity, and

$\Delta\Omega$ is rotational shear, or the difference in angular velocity between the equator and pole.

As may be noted by the number of spots in Fig. 1.12, Kepler-17 is an active G2V star ($1.16 M_\odot$, $1.05 R_\odot$) (Bonomo & Lanza, 2012). The apparent slope which the Kepler-17 spots follow when mapped at the mean stellar rotation period is particularly evident. At the appropriate transit latitude rotation period, spots will align vertically yielding a peaked distribution in total flux deficit. Autocorrelation of flux deficit at varying rotation periods has been successfully applied to determining rotation period at the transit latitude by Silva-Valio & Lanza (2011) for CoRoT-2 and Valio et al. (2017) for Kepler-17. The minimum FWHM of the autocorrelated flux deficit corresponds to maximum spot alignment at the transit latitude rotation period. For Kepler-17, the rotation period at the transit latitude of $-5°$ is 11.24 d. The longitude map in Fig. 1.13 for this rotation period shows spots that are vertically aligned.

For stars whose latitudinal rotation follows a solar-type profile dependent on $\sin^2(\alpha)$, knowledge of the average rotation rate from out–of–transit modulation, P_*, and the rotation period at the transit latitude is sufficient for estimating rotational shear, $\Delta\Omega$, and relative differential rotation, $\Delta\Omega/\bar{\Omega}$, where $\bar{\Omega} = 2\pi/P_*$. The equatorial angular velocity and rotational shear can be derived from a system of two equations. The first equation is a generic form of Equation 1.17

$$\Omega(\alpha) = \mathrm{A} - \mathrm{B}\ \sin^2\alpha \tag{1.18}$$

where A and B are the stellar equatorial angular velocity and rotational shear, respectively.

The second equation for average rotation is the integral of the above generic profile from the minimum latitude to the maximum latitude where spots emerge.

$$\bar{\Omega} = \frac{1}{(\alpha_2 - \alpha_1)} \int_{\alpha_1}^{\alpha_2} \left(\mathrm{A} - \mathrm{B}\ \sin^2\alpha\right) d\alpha \tag{1.19}$$

where α_1 and α_2 are the minimum and maximum latitudes, respectively. For the Sun,

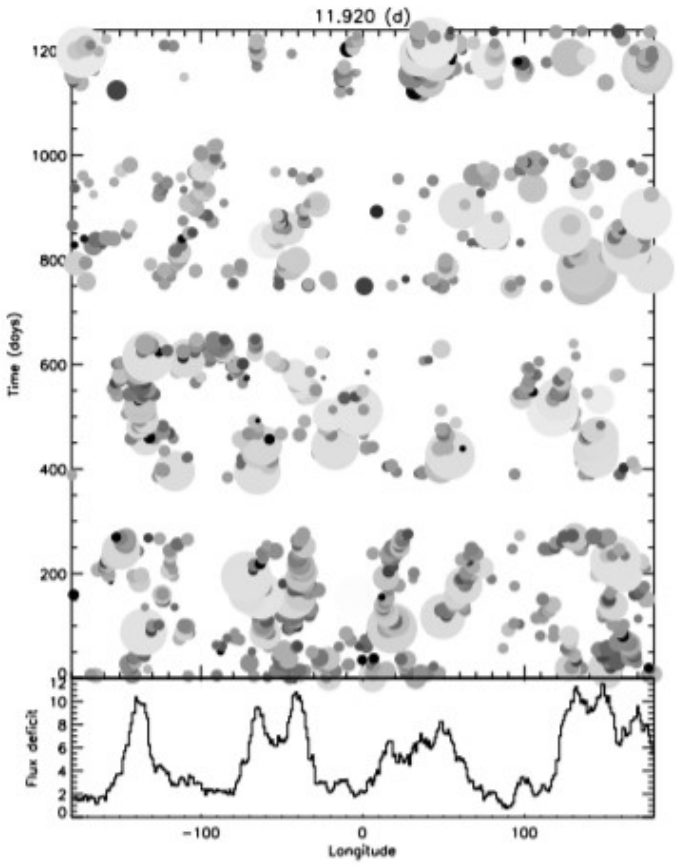

Figure 1.13: A longitude map of starspots on Kepler-17 at the transit latitude rotation period of 11.92 d shows vertical alignment of starspots. The size and shading of starspots represent relative radius and intensity. The bottom panel depicts the total flux deficit at each longitude. (Valio et al., 2017)

the bounds of integration are 0° and ±35°, corresponding to the latitudes at which sunspots emerge, For younger stars which may have polar spots, the upper bound of integration is 90°.

The distribution of starspot flux deficit with longitude given in the bottom panel of Fig. 1.13 shows that stellar activity is concentrated in four regions, indicative of active longitudes where starspots tend to appear. This phenomema has been observed on the Sun (Berdyugina & Usoskin, 2003) and young, rapidly rotating solar-type stars like Kepler-17 (Lanza et al., 2019). While the dynamo mechanisms responsible for the

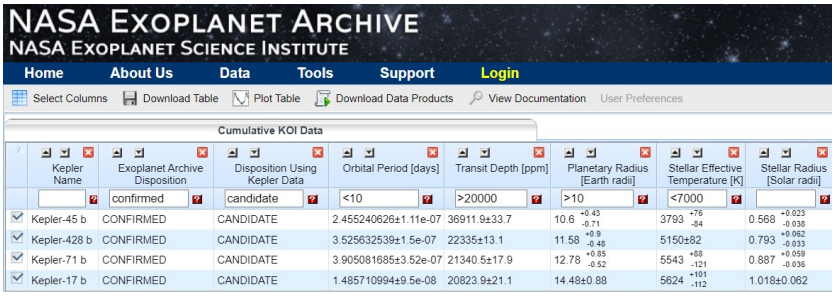

Figure 1.14: Search columns for the KOI table can be set to specify stellar and exoplanet attributes. This example shows the results of a search for a Jupiter-sized planet completing its orbit about a solar-type star in less than 10 d. In order to discern starspots and/or faculae, transit depth must exceed 20,000 ppm. `https://exoplanetarchive.ipac.caltech.edu/cgi-bin/TblView/nph-tblView?app=ExoTbls&config=cumulative` retrieved, 17 July 2021

generation of active longitudes is not completely understood, Weber et al. (2013) have proposed that convection may organize emergent flux.

1.2.4.3 Target Selection and Workflow

The *Kepler* repository is an excellent resource for the selection of a transited star for analysis. The selection process begins with the KOI table, which comprises search fields specific to star, planet, and transit characteristics. Fig. 1.14 depicts the search for a confirmed exoplanet completing its orbiting about an FGKM star in less than 10 d. In order to observe small flux modulations, the planet must be Jupiter-sized, and the planetary transits must have a depth of more than 20,000 ppm. The example search returned four possible target stars orbited by a single planet: Kepler-45 (spectral class M), Kepler Kepler-71 (spectral class G), Kepler-428 (spectral class K, and Kepler-17 (spectral class G). No short cadence data is available for Kepler-428 making it unsuitable for starspot study. Kepler-17 has already been well-studied by cite Adriana. Thus, Kepler-71 and Kepler-45 are the only viable target stars. Analyses of the data for Kepler-71 and Kepler-45 comprise Chapters 2, 3, and 4.

Fig. 1.15 presents the steps taken to prepare transit data, optimize transit parameters, construct a transit model, determine whether an exoplanet has transited a spotted stellar photosphere. A pre-processed set of individual transits is assembled from available

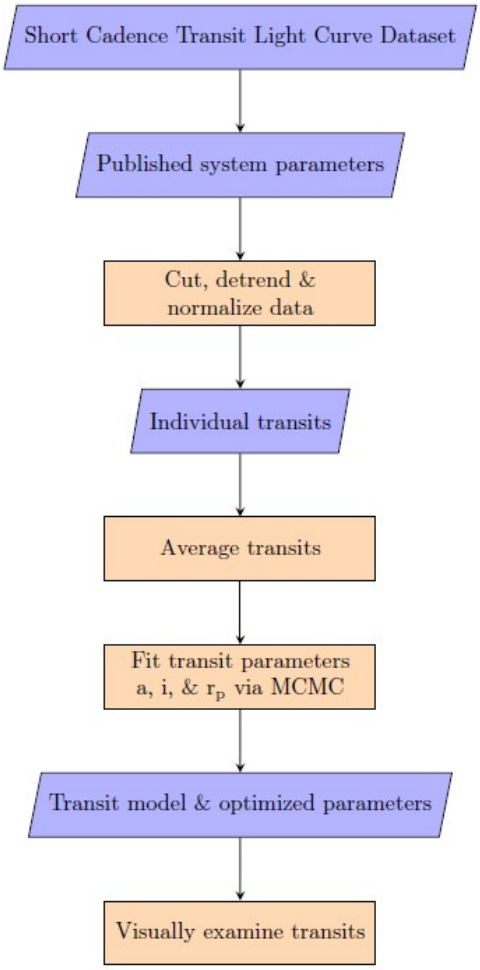

Figure 1.15: Transit light curves for all available quarters of observation are processed to compile a set of individual transits for examination.

Kepler SC transit light curve data in accordance with the planetary orbital period in the literature. Published values for the semi-major axis and inclination of the planets orbits are then used to build a transit model as described by Silva 2003. An MCMC algorithm then varies those parameters to yield values which describe the transit shape that best fits the averaged, observed data. At this point, human intervention is required. For each transit, the residuals resulting from the subtraction of the model from data must be examined for flux modulations that exceed rms noise indicate the

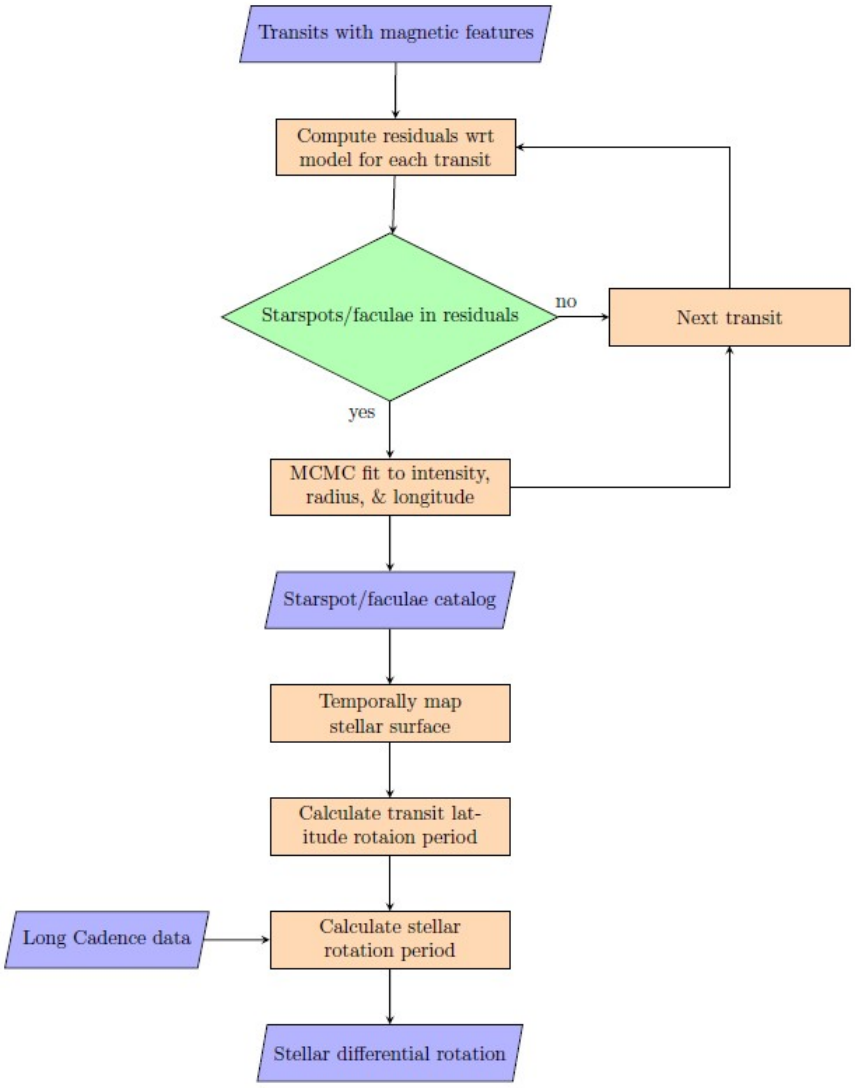

Figure 1.16: Parametrized starspot/faculae modulations are saved in a catalog for the calculation of stellar differential rotation.

occultation of starspots and/or faculae.

Transit analysis continues only if no less than 10% of the transits appear spotted. When this criteria is met, analysis proceeds with the steps in Fig. 1.16. For each transit, a plot of the transit with an overlay of the transit model is used to estimate starspot/faculae characteristics. Characteristics are added to the unspotted transit model for flux am-

plitude variations indicating the occultation of starspots and/or faculae. An MCMC algorithm is again used to find a spot-inclusive model that fits the observed transit by varying starspot/faculae radius, intensity, and longitude.

The optimized starspot/faculae characteristics for all transits are stored in a catalog for further processing. Fig. 1.16 highlights the calculation of differential rotation, as discussed in Section 1.2.4.2. The catalog may also be used to study starspot/faculae coverage and temperature.

1.3 Exoplanetary Satellites

Twenty-five years ago, Mayor & Queloz (1995) presented their discovery of a gas giant exoplanet closely orbiting the solar-type star 51 Pegasi. Their remarkable interpretation of periodic variations in radial velocity observations set the stage for further exoplanet discoveries. Time has seen the development of new detection methodologies and the design and construction of dedicated new precision instruments. The detection of extra-solar planets, from terrestrial to gas giant sized, has become more usual than unusual. In the current decade, astronomers search for the next unusual - extra-solar moons.

1.3.1 Searching for Exomoons

Stellar light is a measurable quantity fundamental to the acquisition of evidence for gravitationally bound bodies, exoplanet-host star or exomoon-exoplanet-host star. Interactions between a central body and its satellite are witnessed in observed light, whether in the form of spectra or light curves. Absorption lines in the spectrum of a star are shifted when the gravitational tug of an orbiting planet causes the star to move. The light curve of a star hosting a transiting planet is modulated by that planet. The gravitational field of an exoplanet lenses the light of a distant star causing a change in background brightness. These observable phenomena have also been considered as the bases for exomoon detection (Heller et al., 2014; Kipping, 2014, and references therein).

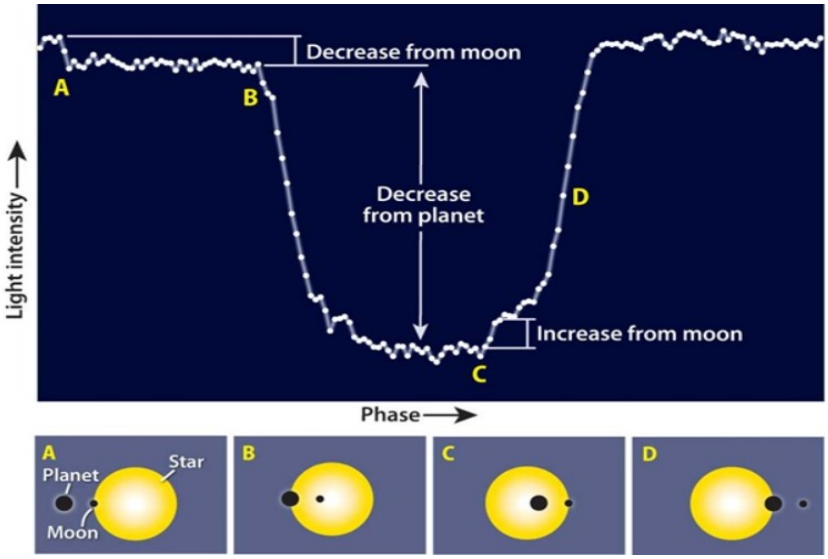

Figure 1.17: Modulations in light curve flux correspond to the moon's position relative to the planet. An exomoon leading the planet's transit causes the flux step-down between points A and B. The exomoon egresses the stellar face at point C resulting in an increase in flux. Credit Roen Kelly. `https://astronomy.com/magazine/ask-astro/2012/12/searching-other-moons` retrieved, 8 November 2020

Currently, the method of transits provides the greatest opportunity for finding exomoons. The proven ability of missions such as *Kepler* to discover both small and large worlds over a wide range of orbital periods is vital to solving a problem down-scaled to planet and moon sizes. High photometric and temporal precisions are needed in order to detect the effects of an exomoon on a transit light curves. A transiting exomoon may produce three types of amplitude modulation: 1) small in–transit amplitude modulations in addition to those of the transiting planets which must be distinguishable from variations due to starspots; 2) out–of-transit decreases in stellar flux when the moon leads or trails the planet; 3) deepening of the transit well during moon-planet-star conjunction and syzygy or opposition and syzygy. As well as affecting flux amplitude, an exomoon may also influence light curves dynamically. The gravitational effect of an exomoon may be witnessed as offsets in transit timing and duration.

1.3.2 Exomoon Photometric Signatures

In a hypothetical 3-body system, an exoplanet orbits about the planet-star barycenter while an exomoon orbits about the moon-planet barycenter. As the planet and moon each follow their orbits, the moon's position, or phase, relative to the planet's positions determines if the moon blocks stellar irradiance. When the moon is to the left or right of the planet's rim, it will cause the blockage of flux in addition to flux lost due to the planet. As depicted in Fig. 1.17, a planet's transit results in a u-shaped light curve, and a moon's transit further reduces stellar brightness when the moon is not obscured by the planet. From points A to B, the moon alone blocks stellar flux, noted as a decrease from the moon. From points C to D, the moon's phase has changed by 180°. The moon no longer blocks stellar flux and intensity increases. The amplitude of the secondary changes in flux, Δf, is determined by the moon's radius relative to the planet's radius, given by

$$\Delta f = \frac{R_m^2}{R_*^2} \tag{1.20}$$

where R_m is the moon's radius and R_* is the stellar radius.

Flux variations due to an exomoon are distinguishable from those due to starspots and faculae. Fig. 1.18 depicts a spotted stellar surface with one facula (left panel) and the simulated light curve which results when that surface is transited. Starspots and faculae, defined as areas darker and brighter than the surrounding photosphere, respectively, present opposing signatures in a transit light curve when occluded. Starspots produce bumps, or flux increase, in the light curve, while faculae produce dips, or flux decrease, in the light curve. The flux variations due to either type of magnetic feature individually is temporally limited, typically lasting on the order of minutes.

The transit of a moon also produces flux reductions, which manifest themselves differently from those due to faculae. Faculae are typically observed close to the stellar limbs, as oblique lines–of–sight reach deeper into facular flux tubes where their walls are hottest (Spruit, 1976). Further, the duration of the transit a moon+planet, and the associated flux decrease, is longer than a facular dip, as shown in Fig. 1.19. A

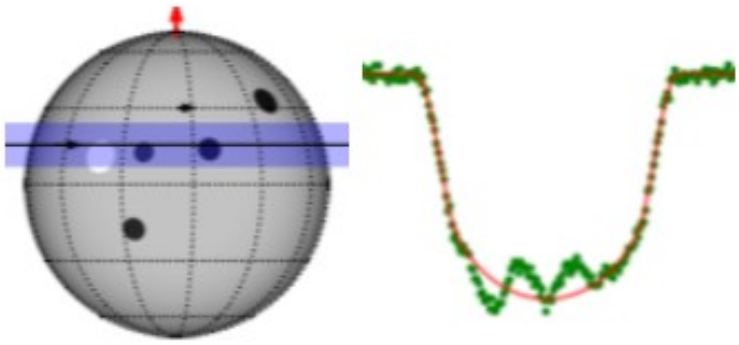

Figure 1.18: A planet transiting a simulated stellar face (left) with one facula (white disk) and two starspots (black disks) along the transit chord (black line) will cause light curve variations. The simulated light curve (right, green) shows two bumps corresponding to the occultation of the starspots whereas a dip appears when a facula is occulted. The red curve represents a model transit over an unspotted stellar face. `https://sites.astro.caltech.edu/~fdai/spot_crossings.html`, retrieved 12 November 2020

more critical difference is the appearance of asymmetric flux decreases due to an exomoon pre-planetary ingress or post-planetary egress (points 1 and 5 in Fig. 1.19). Flux loss due to an exomoon can appear out–of–transit and anywhere in–transit, while facular reduction appears only in–transit. A small number of out–of-transit and in–transit flux asymmetries in the Hubble Space Telescope light curves of Kepler-1625b, a long-period Jupiter-sized planet, were reported by Teachey et al. (2017), who proposed the first exomoon candidate. Their findings included dynamic as well as photometric effects.

1.3.3 Exomoon Effects

In a star-planet-moon system, all bodies move under the influence of their mutual gravitation resulting in perturbed orbits. The reflex motion of the exoplanet due to its satellite's perturbation is pictured in Fig. 1.20. The planet-moon barycenter traces a circular path about the central star, while the planet's orbit wobbles about the barycenter due to the moon's gravitational force.

Sartoretti & Schneider (1999) proposed that the exomoon induced reflex motion, or wobble, of an exoplanet could affect the timing of transits observed in light curves.

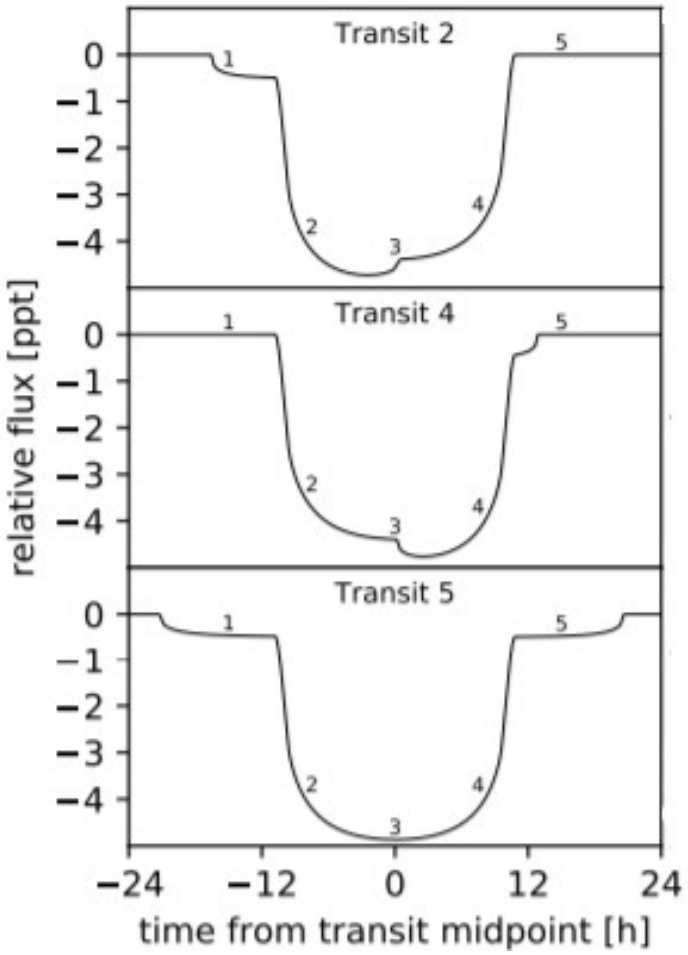

Figure 1.19: A leading moon transits pre-planet at point 1 (top) and post-planet at point 5 (middle). The moon+planet transit together where the light curve is deepest (2 - 3, top, and 3 - 4, middle). A long duration moon+planet transit from points 1 - 5 (bottom). (Rodenbeck et al., 2018)

The planet may enter egress onto the stellar face either early or late depending on its position relative to the planet-moon barycenter. The resulting offsets in transit midpoint, commonly referred to as transit timing variations (TTVs), are sensitive to exomoon mass m_m and semi-major axis a_m, scaling as $m_m a_m$ (Kipping, 2009). The velocity of the wobble, as an additive to the barycentric velocity, may also cause the transit duration to vary, i. e. transit duration variations (TDVs) (Kipping, 2009). This effect is also sensitive to the exomoon's mass and semi-major axis but scales as ${m_m a_m}^{-1/2}$.

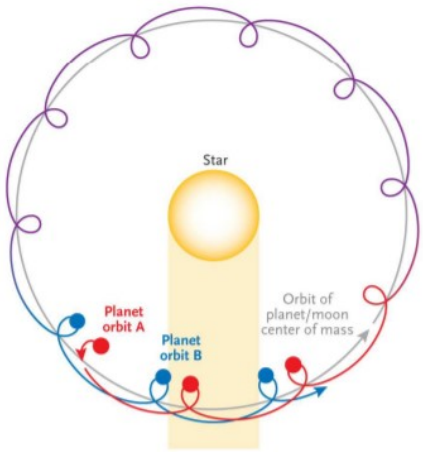

Figure 1.20: The presence of an exomoon can perturb exoplanet motion. While the planet-moon barycenter follows a circular path about the central star, the gravitational force from the exomoon causes the planet's orbit to wobble. (Kipping, 2014)

The ratio of TDV to TTV allows for an estimate of exomoon mass.

The detection of both TTVs and TDVs rely on system configuration. Whereas TTVs may be greater for a moon distant from the host exoplanet, TDVs are greater for a close-in exomoon. Detecting both TDVs and TTVs requires an optimal distance between planet and moon (Barr, 2017). Additionally, either effect could, but not necessarily, appear in conjunction with exomoon flux modulations.

The blockage of stellar irradiance by an exomoon can cause photometric changes equivalent to TTVs and TDVs, *i.e.* photometric timing and transit duration variations, PTVs (aka TTV_p (Simon et al., 2007)) and PDVs, respectively. The reduction in flux due to an exomoon leading or trailing an exoplanet's transit widens an observed transit and shifts transit center. PTVs can be calculated via time-weighted fluxes while TTVs requires parametric light curve fitting (Simon et al., 2015).

An additional photometric effect is the change in transit depth, or photometric radius variations (PRVs) (aka TRVs (Rodenbeck et al., 2020)), due to both a transiting planet and moon. As pictured in Fig. 1.19, the depth of a planet+moon transit is deeper than a planet-only transit. When a planet-only model is fit to true planet+moon flux curve, true flux will overshoot the planet-only simulated flux by an amount propor-

tional to the square of the moon's radius. This difference may be noted close to transit center where it may be distinguished from flux decreases due to faculae, which are observed close to stellar limbs.

1.3.4 Estimating Exomoon Parameters

The photometric method of modeling light curve modulations is a widely used technique for estimating starspot physical parameters (Silva, 2003; Oshagh et al., 2013; Tregloan-Reed et al., 2015; Morris et al., 2018; Juvan et al., 2018). The underlying premise common to all variations on modeling photometry is that synthetic light curves generated by adding starspots to an image of a limb darkened stellar surface may be compared to observed light curve data (see Sect. 1.2.3.1). Starspots are added to the stellar face along the project transit chord of an exoplanet as determined by it orbital distance from the star and its inclination relative to the stellar spin axis. Though the representation of starspots may vary from circular to ellipsoid, the time dependent flux is always the sum of the flux in each image pixel, totalling the net irradiance of the photosphere.

By extending a star-planet model to include a moon, a similar matching of synthetic and observed data may be undertaken to estimate fundamental exomoon physical parameters: radius, orbital period, orbital semi-major axis, and inclination of the orbital plane relative to the stellar rotation axis. A star-planet-moon model requires that planetary parameters (radius, semi-major axis, orbital plane inclination, and orbital eccentricity) have been predetermined. Only the exomoon parameters may vary. In general, the moon's mass is unknown, resulting in the inability to calculate the barycenter of the planet-moon system and model reflex motion. Assuming that the planet is more massive than its moon, the system center-of-mass lies within the planet, and thus, it is within reason to adopt constant planet-to-star and planet-to-moon distances for circular orbits. For elliptical orbits of the planet, the planet-to-star distance during transit is assumed to be constant.

1.3.5 Exomoon Orbits

The ability to resolve the moon's orbital direction and angular positions relative to the planet's position is also sought. When modeling the moon, its orbital direction may be preset to prograde or retrograde. Physically acceptable solutions for both orbital directions result in a degeneracy that cannot be broken via transit light curve analysis (Lewis & Fujii, 2014; Heller & Albrecht, 2014). Generally, the two directions yield orbits which are reflections of each other. The planet's Hill radius is a limited discriminator for the moon's orbital direction. To wit, resolved planet-moon distances within 49% of the planet's Hill radius may indicate either prograde or retrograde stable orbits (Domingos et al., 2006). However, at distances from approximately 50% to 93% of the Hill radius, a retrograde orbit may be stable while a prograde orbit will not be. Resolution of orbital degeneracy may be achieved by mathematical means, one computationally expensive and another much simpler, as described in the next section.

Whether the moon's orbit is prograde or retrograde, an observer will see the moon at the same phases, or angular positions. The moon's phase is dependent upon its orbital period with respect to the planet's orbital period. If both periods are known, the moon's phase ephemeris can be predicted. The issue of exomoon orbital direction is addressed below.

1.3.5.1 Orbital Direction Degeneracy

Two methods for addressing the resolution of orbital direction are determination of the maximum mass of a moon in prograde or retrograde orbit, and simulation of exomoon stability as a function of planet-moon distance. First, Barnes & O'Brien (2002) proposed that the stability of a moon's orbit about a giant planet is dependent upon the tidal dissipation of angular momentum. Based on this idea, Domingos et al. (2006) presented an equation relating the maximum mass of a moon to a planet's tidal dissi-

pation factor, Q_p, and Hill radius, R_H.

$$M_{m,max} = \frac{2}{13}(f_H R_H)^{13/2} \frac{Q_p}{3k_{2p}\mathrm{T}{R_p}^5}\sqrt{\frac{M_p}{\mathrm{G}}} \tag{1.21}$$

where f_H is the fraction of the Hill radius and equal to maxima of 0.49 or 0.93 for prograde and retrograde moon orbits, respectively, k_{2p} is the planet's tidal Love number, T is the moon's lifetime, R_p is the planet's radius, M_p is the planet's mass, and G is the gravitational constant. The age of the stellar system is substituted for T.

Given the dependency of maximum moon mass on the fractional Hill radius, a moon in retrograde orbit can have a greater maximum mass and orbital axis than a moon in prograde orbit. Maximum moon mass also increases with increasing values of Q_p. The tidal dissipation factor of Jupiter is on the order of 10^5, as derived from the orbit of Io, while it may be as high as $\simeq 10^{12}$ for exoplanets (Cassidy et al., 2009).

Tidal dissipation is also quantified via the modified tidal quality factor, Q'_p, which is expressed in terms of Q_p by

$$Q'_p = \frac{2k_{2p}}{3}Q_p \tag{1.22}$$

The approximate Love number for Jupiter is 0.54, for example, when assuming a core mass density of 20 - 30 g/cm^3 for an inflated planet. (Ni, 2018; Sestovic et al., 2018).

By comparing circularization times with stellar age for transiting hot Jupiters, Bonomo et al. (2017) found that generally $10^5 \lesssim Q'_p \lesssim 10^9$ for close-in giant planets with orbital semi-major axes less than 0.05 au. The estimation of upper and lower limits is complicated by the difficulty to bound stellar ages. Yet, the closer the planet, the higher the value of Q'_p and in turn the higher the value of Q_p and maximum moon mass.

Second, the stability of a star-planet-moon configuration may be numerically simulated as a 3-body problem (Szebehely & Grebenikov, 1969; Murray & Dermott, 1999). The critical limits for orbital stability are a function of the planet's Hill radius and the eccentricities of the moon's and planet's orbits, given by Domingos et al. (2006) as

$$a_{E,pro} = R_{Hill}0.4895(1 - 1.0305e_p - 0.2738e_{sat}) \tag{1.23}$$

and

$$a_{E,ret} = R_{Hill} 0.9309(1 - 1.0764e_p - 0.9812e_{sat}) \tag{1.24}$$

where $a_{E,pro}$ and $a_{E,ret}$ are the upper critical limits, and e_p and e_{sat} are the eccentricities of the planet and its satellite, respectively. Long-term integrations are performed in a_{sat}xe_{sat} parameter space, where the moon's semi-major axis a_{sat} is bounded by the planet's radius and semi-major axis. The moon's eccentricity e_{sat}may be bound as well to values within 0.0 to 1.0.

While computationally expensive, this method yields both regions of orbital stability and instability. Unstable orbits result in either the ejection of the moon from the system or the decay of the moon's orbit towards collision with the planet. Once the moon crosses the Roche limit, it will disintegrate.

1.3.5.2 Exomoon Phases

Similar to our moon, an exomoon will pass through a sequence of positions, or phases, as seen by an observer. The moon's position relative to the planet it orbits will be commensurate with the ratio of the planet to moon orbital periods. Assuming that the planet's orbital period is not an exact multiple of the moon's orbital period, the remainder when dividing the planet's orbital period by the moon's translates to the number of degrees by which the moon's position shifts after every integral number of planet orbits. Hypothetically, the shift in moon position will be apparent in the repeat appearance of flux modulations due to the moon in a sequence of transit light curves. Given sufficient moon amplitude modulations, the initial moon phase at mid-transit of the first transit may be estimated. The phase angle of the moon's orbit at the mid-transit time of the n^{th} planetary orbit, $\theta(n)$, is described by

$$\theta(n) = \theta_0 \pm 2\pi n P_{orb}/P_{moon} \tag{1.25}$$

where P_{orb} is the planet's orbital period, P_{moon} is the moon's oribtal period, and θ_0 is the phase of the moon at mid-transit of the very first transit. The plus sign defines prograde motion of the moon, while the minus sign denotes retrograde motion.

The technique of eXomoon Phase Gating (XPG) validates the moon's angular positions predicted by Eq. 1.10 by searching for transits whose corresponding positions match within a predefined angular gate, e.g. ±4°. The width of the gate adjusts for offsets in mid-transit timing and uncertainties in phase angle. For transits meeting a series of gates, e.g. every 30°, plots of averaged transits at each angular position will show flux modulations due to the moon when the moon and planet are not in conjunction.

1.4 Research Questions

This thesis focuses on the application of transit photometry from the *Kepler* mission to investigations of stellar activity and exomoons. Since its beginnings as a platform for exoplanet discovery, the Kepler mission has become an invaluable source for the study of solar-type stars and their systems. Transit light curves are common ground for many areas of study. As applies to this thesis, stellar activity and the physical characteristics of extrasolar bodies are derived from the flux amplitude variations contained in *Kepler* transit light curves. In the case of one target star, the use of the same photometric data in different studies is demonstrated. The chapters that follow answer questions about the connection between the Sun and Sun-like stars, and the existence of an exomoon in an extrasolar system.

1.4.1 To what extent do the differential rotation profiles of solar-type stars demonstrate physical attributes of the Sun's dynamo?

In Chapters 2 and 3, the papers (Zaleski et al., 2019) and (Zaleski et al., 2020a) examine the differential rotations of the G7V star Kepler-71 and the M1V star Kepler-45 from the mapping of starspots and faculae observed along the transit chord. Additionally, the features of starspots and faculae on those stars are compared to their solar counterparts. For both stars, rotation is found to be latitude dependent. However, while the rotational shear for Kepler-45 is within the theoretical limits for an M dwarf (Reinhold & Gizon, 2015), the rotational shear for Kepler-71 is significantly less than

the 0.055 rad d^{-1} for the Sun (Berdyugina, 2005) and infers an almost rigid rotation.

1.4.2 How do indicators in the transit light curves of Kepler-45 signal the orbit of a Jupiter-sized planet + super-Earth moon system about the host star?

In Chapter 4, the paper (Zaleski et al., 2020b) investigates the transit of a planet+moon, rather than the transit of a planet only, as a source of modulation in the high-precision light curves of Kepler-45. Previously, the HEK: Hunt for Exomoons with *Kepler* (Kipping et al., 2012) proposed the exomoon candidate Kepler-1625b-i (Teachey et al., 2017). Due to the 287.4 d orbital period of Kepler-1625b, few transits have been observed in support of this candidate. Kepler-45b completes its orbit about the host star every 2.46 d, and more than 300 transits have been recorded. Zaleski et al. (2020b) (Chapter 4) presents the search for an exomoon in the Kepler-45 system via an analysis of accumulated transits. The methodology incorporates multiple lines of reasoning for evaluating the existence of an potential exomoon.

Ce que nous connaissons est peu de chose, ce que nous ignorons est immense

Pierre-Simon Laplace

Chapter 2 Differential rotation of Kepler-71 via transit photometry mapping of starspots and faculae

The magnetic behavior of solar-type stars is benchmarked against the known activity of the Sun. Cool main-sequence FGKM stars having a layered radiative-convective internal structure are expected to exhibit attributes paralleling the Sun's. To investigate these characteristics, this study focuses on the fundamental magnetic phenomena from which much of stellar behavior may be derived, starspots and faculae. Do the appearance and erosion of these distinct regions of photospheric activity on Sun-like stars tell the tale of a solar dynamo at work?

The ability to detect starspots and faculae in transit light curves relies upon the selection of target stars having available high precision data. Flux amplitude variations due to starspots and faculae are but a few percent of the transit depth, at best. The high photometric and temporal precisions of the data from the *Kepler* mission made such a selection possible. The Exoplanet Archive of Kepler Objects of Interest was examined for confirmed planets with maximum transit depth and signal-to-noise ratio.

Candidate planets also had to have cataloged SC light curves, as indicated in the Kepler Target Overview. After visual examination of the light curves, the first target star selected was Kepler-71, a late-type G star. This star hosts a single hot Jupiter in a 3.9 day orbit. Long cadence data exhibits sinusoidal trends due to the rotational modulation of starspots from which the mean stellar rotation rate is measurable. Short cadence light curves exhibit individual starspots and faculae along the transit chord occulted by the hot Jupiter Kepler-71b. The physical parameters of these magnetic features (radial size, intensity, and longitude) were estimated by fitting each observed light curve to synthetic light curves generated by a spotted star-planet model. The derived characteristics were translated into activity maps of the stellar surface.

Kepler-71 stellar activity and rotation at the transit latitude were assessed relative to the attributes of the Sun's behavior. The analytic methods employed and the results achieved are detailed in the following paper, "Differential rotation of Kepler-71 via transit photometry mapping of starspots and faculae" (Zaleski et al., 2019).

2.1 Zaleski et al. (2019) "Differential rotation of Kepler-71 via transit photometry mapping of faculae and starspots"

The published paper Zaleski et al. (2019), "Differential rotation of Kepler-71 via transit photometry mapping of faculae and starspots", follows.

Monthly Notices of the ROYAL ASTRONOMICAL SOCIETY

MNRAS **484,** 618–630 (2019) doi:10.1093/mnras/sty3474
Advance Access publication 2019 January 16

Differential rotation of Kepler-71 via transit photometry mapping of faculae and starspots

S. M. Zaleski [1]★ A. Valio,[2] S. C. Marsden[1] and B. D. Carter[1]

[1] *University of Southern Queensland, Centre for Astrophysics, Toowoomba 4350, Australia*
[2] *Center for Radio Astronomy and Astrophysics, Mackenzie Presbyterian University, Rua da Consolação, 896 São Paulo, Brazil*

Accepted 2018 December 19. Received 2018 December 18; in original form 2017 November 16

ABSTRACT

Knowledge of dynamo evolution in solar-type stars is limited by the difficulty of using active region monitoring to measure stellar differential rotation, a key probe of stellar dynamo physics. This paper addresses the problem by presenting the first ever measurement of stellar differential rotation for a main-sequence solar-type star using starspots and faculae to provide complementary information. Our analysis uses modelling of light curves of multiple exoplanet transits for the young solar-type star Kepler-71, utilizing archival data from the *Kepler* mission. We estimate the physical characteristics of starspots and faculae on Kepler-71 from the characteristic amplitude variations they produce in the transit light curves and measure differential rotation from derived longitudes. Despite the higher contrast of faculae than those in the Sun, the bright features on Kepler-71 have similar properties such as increasing contrast towards the limb and larger sizes than sunspots. Adopting a solar-type differential rotation profile (faster rotation at the equator than the poles), the results from both starspot and facula analysis indicate a rotational shear less than about 0.005 rad d^{-1}, or a relative differential rotation less than 2 per cent, and hence almost rigid rotation. This rotational shear contrasts with the strong rotational shear of zero-age main-sequence stars and the modest but significant shear of the modern-day Sun. Various explanations for the likely rigid rotation are considered.

Key words: stars: activity – stars: rotation – stars: solar-type – starspots.

1 INTRODUCTION

Starspots and faculae are observable proxies of stellar magnetic activity in solar-type stars, providing a window to the internal dynamo. Starspots and faculae may be observed on cool stars with a convective envelope surrounding a radiative core (Berdyugina 2004; Balona & Obedigamba 2016). They are tracers of an unseen dynamo and markers of magnetic topology. Starspots and faculae are the surface emanations of internal magnetic fields caught in turbulent flows. They are areas of amplified magnetic fields which erupt through the stellar surface. Starspots and faculae differ thermally from the surrounding photosphere (Ortiz et al. 2002), with starspots appearing dark against a hotter and brighter photosphere and faculae appearing brighter than the photosphere.

Spots on the Sun have been observed for four centuries. Sunspot coverage and the latitudinal drift of the sunspot distribution have been correlated with long-term solar magnetic cycles (Maunder 1904; Hathaway 2015; Covas 2017). Magnetic activity in a solar-type interface dynamo is thought to be generated deep in the convective zone at the tachocline where rotation interacts with convective flows (Spruit 1997; Spuit 2011). Though the magnetohydrodynamic processes at work in the stellar interior are not fully understood, the convectively driven interface dynamos in late-type stars, slow rotators such as the Sun, are based on rotating, weakly magnetized differential flows (Uzdensky et al. 2010). Any large-scale dynamo model such the solar $\alpha\Omega$ dynamo, in which weak magnetic fields are amplified by shearing of field lines via differential rotation (Hubbard, Rheinhardt & Brandenburg 2011), twisted by the Coriolis effect and promoted to the surface via magnetic buoyancy, must allow the same magnetic features, dark spots, and bright faculae, to appear on the surface of stars with a convective envelope (Hubbard et al. 2011; Isik, Schmidtt & Schussler 2011; Shapiro et al. 2016). Thus, any $\alpha\Omega$ dynamo model that explains the magnetic activity of the Sun should be applicable to any rotating, convective solar-type star. Observations of solar-type stars expand the understanding of stellar processes, i.e. convection, rotation, and magnetism, and allow for the evaluation of commonality among dynamic properties of the Sun and other stars, thereby establishing a solar-stellar connection. An interface dynamo model may be constructed to agree with available solar data, but it will be limited by that same data. Solar data collected in this century reflect the Sun's current activity. The characteristics of starspots and faculae on magnetically active solar-

★ E-mail: shelley.zaleski@usq.edu.au

type stars will add to our understanding of the evolution of the Sun's magnetic activity.

The presence of starspots and faculae contribute to the overall stellar irradiance and light curve variance (Mehrabi, He & Khosroshahi 2017). The temporal change in starspot/facula coverage on the stellar surface is witnessed as periodic, sinusoidal trends in stellar light curves, with the degree of light curve modulation being indicative of magnetic activity level (Mehrabi et al. 2017). Studies of modulation in light curves recorded by the *Kepler* mission (Borucki 2010) have produced a wealth of information on stellar rotation rates and activity trends (McQuillan, Mazeh & Aigrain 2013, 2014; Reinhold, Reiners & Basri 2013; He, Wang & Yun 2015; Mehrabi, He & Khosroshahi 2017). During its approximately four years of data collection, from 2009 March to 2013 May, NASA's *Kepler* telescope gathered data for over 150 000 stars in a wide-field of view in the Cygnus–Lyra region. Though the primary goal of the *Kepler* mission was to discover terrestrial size planets in the habitable zones of Sun-like stars via the transit method (Borucki 2010), the abundance of data collected has supported the analysis of stellar behaviour over a range of spectral types and ages. *Kepler* collected data in two cadence modes, a long cadence (LC) of 29.4 min and a short cadence (SC) of 58.85 s. LC data are well suited to the analysis of large-scale trends, such as the periodicity and amplitude of light curve modulation due to magnetic activity. For *Kepler* G-type main-sequence stars with rotation periods of 10–20 d, for example, the periodicity and amplitude of light curve variation show a positive correlation for approximately 80 per cent of sampled stars (Mehrabi et al. 2017). The percentage of positive correlation stars is greatest for shorter stellar rotation periods and least for rotation periods longer than 20 d, inferring that magnetic activity decreases with age due to spin-down and decreasing $T_{\rm eff}$, though starspot stability increases as rotation slows. The active regions on G-stars are also larger and more stable than those on A and F stars (McQuillan, Aigrain & Roberts 2012; Giles, Collier Cameron & Haywood 2017). Analysis of starspot lifetime for FGKM stars with rotation periods approximately 10 and 20 d shows that starspots decay more slowly on cooler stars, commensurate with the diffusive mechanisms of the dynamo. For G-type stars, the majority of spots lasted up to 100 d, with few lasting as long as 300 d (Mehrabi et al. 2017).

While magnetic activity is evident in LC data, the fine detail indicative of faculae, single starspots, or groups of starspots is not discernible. Due to a high-sampling rate, SC data have the resolution to detect the presence of starspots and faculae in transit light curves. When an exoplanet occults starspots and/or faculae during its transit across the face of its host star, small variations appear in the in-transit portion of a stellar light curve. Starspots and faculae are seen as bumps and dips, respectively, in the transit light curve. An example of amplitude variation due to occulted magnetic structures is shown in Fig. 2. Starspot and facula physical characteristics of radius, intensity, and position may be modelled using the width, height, and time of variations (Silva 2003). Through the application of transit photometry mapping, these characteristics are translated into magnetic activity maps of the stellar surface. This methodology (see Section 3) has been used to assess surface activity and stellar rotation at transit latitudes for Kepler-17 (Valio et al. 2017), CoRoT-2 (Silva-Valio et al. 2010; Silva-Valio & Lanza 2011), and Kepler-63 (Estrela & Valio 2016).

Starspot and facula longitudes derived from SC data lie along the projected transit latitude, which is typically non-equatorial. Stellar rotation rates at transit latitudes may be calculated from starspot/facula longitudes in transit light curves commensurate with multiple, consecutive stellar rotations. Stellar differential rotation may be estimated when latitudinal rotation periods differ from that at the stellar equator. Simulations of differential rotation in spectral type G and K stars at 0.7 and 0.9 $M_{\odot}$, respectively, rotating at the solar rate show solar-like differential rotation, with the equator rotating more rapidly than the poles, e.g. Matt et al. (2011). Küker & Rüdiger (2005) modelled FGK stars for different solar masses and found that differential rotation is dependent on stellar temperature, i.e. convection zone depth, and only weakly dependent on rotation rate. The greater the stellar effective temperature and mass, the higher the shear and differential rotation (Barnes et al. 2005; Balona & Obedigamba 2016). The differential rotation of *Kepler* stars calculated by Reinhold et al. (2013) predominantly lies between 0.03 and 0.11 rad d^{-1} over the temperature range 3500–6000 K. They find wide scatter in differential rotation values from 0.4 to 3.0 rad d^{-1} at temperatures from 6000 to 7000 K. This is in agreement with Barnes et al. (2005), who predicted an exponential growth in differential rotation as a function of stellar temperature for young stars, and the observations of Marsden et al. (2011) and Waite et al. (2011). Barnes et al. (2005) also proposed that a decrease in differential rotation in later spectral types is due to a greater α-effect than Ω-effect.

To date, measurement of stellar rotation period and differential rotation has utilized spectroscopic and spectropolarimetric methods to build structural and magnetic maps of spotted stellar surfaces, Fourier domain methods applied to Doppler broadened line profiles, and photometric methods to analyse the periodic trends in light curves caused by starspots. Doppler Imaging (DI) and Zeeman Doppler Imaging (ZDI) have been used to map the surfaces of active cool stars. Their use, especially DI, tends to be limited to comparatively rapid rotators, as spatial resolution of the stellar surface decreases with slowing rotation. Nevertheless, DI and ZDI mapping can measure the differential rotation of moderately to rapidly rotating stars, e.g. Carter, Marsden & Waite (2015) and Hackman et al. (2016). Fourier transformed absorption profiles show distinct behaviour in the Fourier domain (Reiners & Schmitt 2002). This technique, however, is also limited to rotators with values of $v\sin i \geq 10$ km s^{-1}.

Photometric techniques used to study the effect of starspots on stellar light curves include phase tracking (Davenport, Hebb & Hawley 2015) and sine-fitting periods from Lomb–Scargle periodograms (Reinhold et al. 2013). These methods are applicable to a wide range of stellar rotation rates and magnitudes. Aigrain et al. (2015) employed various photometric methods, including Lomb–Scargle periods, auto-correlation functions, and wavelet power spectra, in a blind study to extract rotation rates and differential rotation from simulated *Kepler* light curves. The study showed limited agreement among methods in the computation of differential rotation.

Our methodology is based on individual magnetic features as they appear in transit light curves rather than on broader photometric trends. We have detected and mapped both facula and starspot signatures in the transit light curves for Kepler-71 and thus present the estimation of transit latitude rotation periods and differential rotation from the longitudinal movement of individual facula as well as starspots. We discuss the differential rotation of Kepler-71 relative to theoretical predictions and published observational values (see Section 5).

2 KEPLER-71 OBSERVATIONAL DATA

Kepler-71 is a *Kepler*-band magnitude 15, solar-type G star with a single hot Jupiter in a 3.91 d orbit. The parameters of the host star-exoplanet system are given in Table 1. Kepler-71 has approximately

Table 1. Star-exoplanet parameters of the Kepler-71 system.

Parameter	Value	Ref.
Star		
Spectral type	G7V–G9V	1
Mass ($M_\odot$)	$0.997^{+0.03}_{-0.07}$	2
Radius ($R_\odot$)	0.887 ± 0.05	2
Effective temp (K)	5540 ± 120	2
Rotation period (d)	19.773 ± 0.008	3
Age (Gyr)	2.5–4.0	4, 5
Limb darkening coeff, u_1	0.431 ± 0.008	3
Limb darkening coeff, u_2	0.287 ± 0.005	3
Planet		
Mass ($M_{\rm Jup}$)	n/a	
Radius ($R_{\rm Jup}$)	1.1987 ± 0.0044	3
Radius ($R_{\rm star}$)	0.1358 ± 0.0005	3
Semimajor axis (au)	$0.05029^{+0.00002}_{-0.00006}$	3
Semimajor axis ($R_{\rm star}$)	$12.186^{+0.006}_{-0.015}$	3
Inclination angle (°)	$89.557^{+0.005}_{-0.003}$	3
Orbital period (d)	$3.905079476^{+8e-6}_{-9e-6}$	6

1: Howell et al. (2010), 2: Mathur et al. (2016), 3: Fit by authors in this work, 4: Meibom et al. (2015), 5: Guinan & Engle (2009), and 6: Müller et al. (2013).

the same size and mass as the Sun with $0.887\,R_\odot$ and $0.997\,M_\odot$, respectively, with an orbiting planet of radius $1.14R_{\rm Jup}$. Howell et al. (2010) first noted rotational modulation in the raw *Kepler* light curves for Quarter 6 and intensity fluctuations indicative of starspots in the transit well of phase folded light curves. Both McQuillan et al. (2013) and Holczer et al. (2015) calculated a stellar rotation period of 19.77 d via the autocorrelation of light curve modulation. Holczer et al. (2015) noted another prominent peak in the power spectrum at 9.9 d, possibly due to active regions that are 180° out-of-phase (discussed in Section 4.4).

The age of Kepler-71 is estimated to be between 2.5 and 4.0 Gyr. The lower bound of 2.5 Gyr was determined by Meibom et al. (2015) in their study of stellar rotation in the 2.5 billion year old open cluster NGC 6819. The average rotation period of 18.2 d for the observed solar mass stars in that cluster served to establish a rotation rate benchmark for the Sun at 2.5 Gyr. The upper bound of 4.0 Gyr is taken from the study of main-sequence G-star rotation rate versus age presented by the *Sun in Time* program (Guinan & Engle 2009).

We extend the work of Howell et al. (2010) and Holczer et al. (2015) by quantifying starspot activity on Kepler-71. The NASA Exoplanet Archive contains pre-conditioned light curve data for Kepler-71 spanning *Kepler* Quarters 1–17. The *Kepler* pre-conditioning pipeline removes systematic artefacts of the instrumentation onboard the *Kepler* spacecraft from raw aperture data to yield Pre-search Data Conditioning Simple Aperture Photometry (PDCSAP) flux values that preserve stellar variations and astrophysics (Jenkins et al. 2010; Smith et al. 2012; Stumpe et al. 2012). The PDCSAP SC data provide both uninterrupted coverage for time periods during which multiple transits are observed and the temporal resolution required for the detection of occultations lasting on the order of minutes. Of interest to this investigation are the detrended PDCSAP SC light curves in *Kepler* Data Release 25 (Thompson 2016) available for Quarter 6 (2010 June 24–2010 September 22), Quarter 7 (2010 September 23–2010 December 22), Quarter 13 (2012 March 29–2012 June 27), Quarter 14 (2012 June 28–2012 October 3), Quarter 15 (2012 October 5–2013 January 11), Quarter 16 (2013 January 12– 2013 April 8), and Quarter 17 (2013 April 9–2013 May 11). The SC light curves for those quarters, as shown in Fig. 1, comprise observations for approximately 500 d and contain 117 complete, uninterrupted transits out of 261 total transits from the beginning of Quarter 6 to the end of Quarter 17.

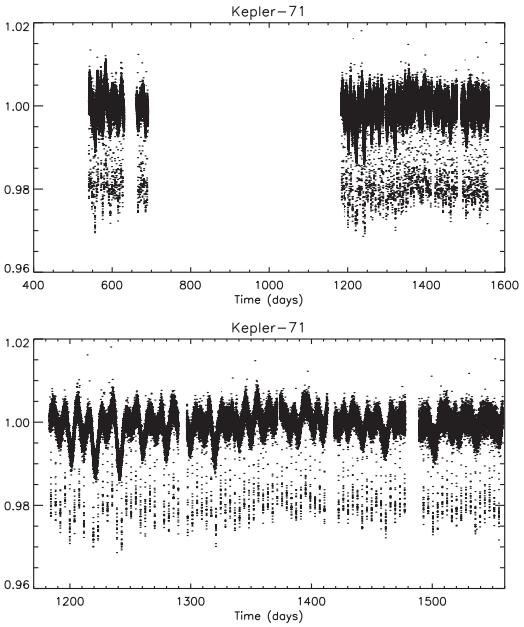

Figure 1. *Top:* SC light curves for Kepler-71 for Quarters 6–7 and Quarters 13–17. *Bottom:* Enlargement of the SC light curves for Quarters 13–17.

Late-type stars, such as Kepler-71, display a stochastic stellar variability commensurate with surface activity (McQuillan et al. 2012). As such, we require that the transit well be deep enough to detect relatively small modulations due to faculae and starspots. Deep transits are evident in Fig. 1. The mean normalized flux decrease for Kepler-71 is approximately 2 per cent from ingress to the bottom of the transit well. The example given in Fig. 2 for Transit 3 shows an approximate 2.5 per cent overall decrease in normalized flux. Mid-transit time ($t = 0$) corresponds to transit epoch 547.3541 BKJD [Barycentric Kepler Julian Date defined as Barycentric Julian Day (BJD) minus an offset of 2454833 corresponding to 12:00 On 2009 January 1 UTC]. The flux changes due to the starspot at midtransit and the faculae at times -1.0 h and $+0.8$ h from transit centre, respectively, are on the order of 0.4, 0.3, and 0.2 per cent. The modelled red curve is described in the next section.

3 THE MODEL

The light curve model developed by Silva (2003) is used to determine the physical characteristics of in-transit photometric variations caused by the passage of an exoplanet across a stellar disc. The model's flexibility allows for the generation of transit light curves for an exoplanet traversing unspotted, spot-dominated, and facula-dominated stellar surfaces. Thus, the model may be used for solar-type stars of varying magnetic activity. As solar-type stars evolve along the main-sequence, losing angular momentum, magnetic activity moves from spot dominance to facula dominance

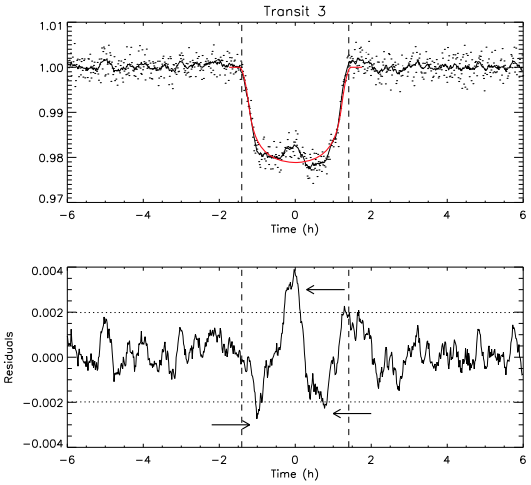

Figure 2. Top: SC light curve for Kepler-71, Transit 3. The solid line is the data smoothed every 10 points. Bottom: Residuals after subtraction of a spotless model (red curve in top panel). Potential starspot and facula signatures are centred at approximately 0 h, -1.0 h, and + 0.8 h, respectively, from transit centre, as indicated by the black arrows. The time at transit centre corresponds to transit epoch 547.3541 BKJD (Barycentric Kepler Julian Date, BJD-2454833). The spot and faculae signals are detected beyond the rms noise (dotted horizontal line). The vertical dashed lines mark the beginning of ingress and egress of the planet on to the stellar disc.

(Berdyugina 2004). We find the presence of both starspots and faculae on Kepler-71, as shown in Fig. 2.

The model represents the stellar surface as a two-dimensional pixelated white light image (disc) with varying intensity, I, decreasing with $\mu = \cos(\theta)$, where θ is the angle between the line of sight and the emergent intensity. The quadratic limb darkening applied to the image is given by

$$\frac{I(\mu)}{I_c} = 1 - u_1(1-\mu) - u_2(1-\mu)^2 \quad (1)$$

where I_c is the maximum intensity at disc centre, and u_1 and u_2 are the limb darkening coefficients.

The planet is a dark, opaque disc with a radius defined in units of the stellar radius. Its orbit is calculated given the physical parameters of the host star-exoplanet system, specifically the semimajor axis and inclination angle of the planet's orbit. The planetary orbit is assumed to be circular, given the lack of RV data to otherwise constrain the eccentricity value. The angle between the orbital and stellar spin axes may be input for oblique transits. However, for the Kepler-71 system, the transit latitude remains unchanged between transits, and thus, the orbit is adopted as coplanar with the stellar equator. The presence of the same magnetic features on consecutive transits infers an obliquity close to zero. The model determines the orbital position of the planet every two minutes, and the stellar intensity is calculated by summing over all pixels in the stellar image. This technique produces a noiseless, or unspotted, transit light curve as a function of time.

The parameters used to model the noiseless transit light curve include orbital semimajor axis, inclination, planet radius, planet orbital period, and quadratic limb darkening coefficients. A preliminary model light curve is generated using parameter values available in the literature. To ensure that the shape of the transit

Table 2. Uniform priors for model light curve fitting.

Parameter	Range
Planet radius (R_{star})	[0.02–0.2]
Semimajor axis (R_{star})	[9–16]
Inclination angle (°)	[85–95]
Impact parameter	[0.01–0.5]
Parametrized limb darkening coeff 1	[0–1]
Parametrized limb darkening coeff 2	[0–1]

Table 3. Secondary transit parameters of the Kepler-71 system.

Parameter	Value
Transit latitude (°)	$-5.404\ ^{+0.003}_{-0.007}$
Impact parameter	0.0942 ± 0.0001
Transit duration (h)	2.771 ± 0.001

is well described by the parameters, the model is fit to an average of the normalized and phase folded observed transits. A first fit of the published values for semimajor axis, planet radius, inclination, and quadratic limb darkening coefficients was performed using the χ^2 minimization routine AMOEBA (Press et al. 1992). The resulting fit parameters where then used as initial values to a Monte Carlo Markov Chain (MCMC) ensemble sampler. We chose to run an IDL version of the affine-invariant ensemble sampler for MCMC's proposed by Goodman & Weare (2010) and introduced in PYTHON by Foreman-Mackey et al. (2013). By sampling from a posterior probability representing a distribution of parameters consistent with the observed data, we obtained the most probable parameters and their uncertainties. Given the limited number of parameters input to the transit model, it was sufficient to calculate likelihoods and posterior probabilities for thousands of walkers and thousands of iterations of the Goodman & Weare MCMC sampler (GWMCMC). The walkers stretched through the parameter space during a relatively short burn-in phase. All GWMCMC chains were flattened before splitting the walker values for each starspot and facula parameter into confidence intervals using quantiles of 16 per cent, 50 per cent, and 84 per cent. Each parameter value was accepted as the median (50 per cent) value of its sampling, with lower and upper 1σ errors corresponding to the 16 per cent and 84 per cent quantiles (Hogg & Foreman-Mackey 2018).

As required by unbiased sampling, prior knowledge of the transit model parameters was not assumed. The parameters were allowed to explore parameter space freely but within physically acceptable bounds set by uniform priors. The priors are given in Table 2. To remove any degeneracy with other parameters, the limb darkening coefficients were parametrized following the triangular sampling methodology of Kipping (2013). At each iteration of the sampler, the parametrized coefficients were re-expressed as u_1 and u_2 before calculating the model transit light curve.

The optimized transit model parameters are given in Table 1. To best fit the averaged transit shape, the semimajor axis increased by 4.5 per cent, the inclination increased by 4.5 per cent, and the planet's radius decreased by 3.2 per cent. Limb darkening coefficient 1 decreased and limb darkening coefficient 2 increased from previously published values.

Secondary transit parameters, which include impact parameter, transit latitude, and transit duration, are computed from the fit parameters and are given in Table 3. Impact parameter and transit latitude are determined by inclination angle and semimajor axis, as

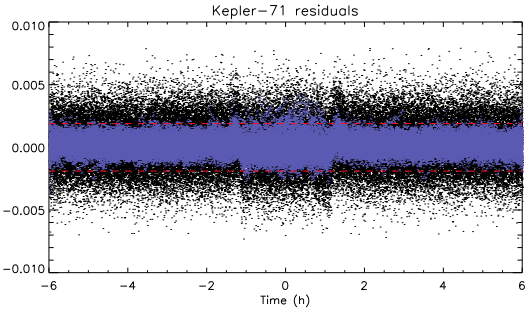

Figure 3. Residuals of all *Kepler* SC transit light curves. The black dots are the residuals for all observed light curves after subtraction of the transit model constructed using optimized parameters. The blue dots are the same data smoothed every 10 points. The horizontal red lines represent the unsmoothed out-of-transit rms.

given by

$$b = \frac{a\cos(i)}{R_{\rm star}} \tag{2}$$

$$lat_{\rm tran} = \arcsin\left[\frac{a}{R_{\rm star}\cos(i)}\right] \tag{3}$$

where a is the semimajor axis, $R_{\rm star}$ is the stellar radius, and i is the inclination of the planet's orbit. We have arbitrarily chosen the transit projection to be in the Southern hemisphere.

Though the light curves have been pre-conditioned, they remain inherently noisy with possible contributions from long-term stellar variability or instrumental effects. The residuals for all observed light curves after subtraction of the model constructed with the parameters obtained from the GWMCMC fit are shown in Fig. 3 as black dots. The blue dots are the same data smoothed every 10 points. The red horizontal lines banding the smoothed data represent the unsmoothed out-of-transit rms, which is approximately ten times the 3 h Combined Differential Photometric Precision (CDPP; Christiansen, Jenkins & Caldwell 2012) of 184 ppm. The calculated rms noise of the unsmoothed residuals is 0.0020 in-transit and 0.0019 out-of-transit. After smoothing the residuals every 10 points, the rms noise is reduced to 0.00063 out-of-transit and 0.00093 in-transit. The in-transit rms is greater than the out-of-transit rms in both cases, indicating the presence of magnetic features. The smoothed data will be used in the search for stellar activity signatures (see Section 4).

The optimized light curve simulating a transit across the unspotted stellar disc is compared to each observed transit light curve to disclose the presence of surface variations. When the transited stellar surface contains starspots or faculae, a modulation beyond the typical irregularity due to stellar noise is seen in the flux residuals resulting from subtraction of the light curve model from observed light curve data. Bumps and dips in the residuals indicate the position of starspots and faculae, respectively, as a function of time (see bottom panel of Fig. 2).

Estimates of starspot and faculae physical characteristics may be added to the unspotted model in order to synthesize spotted light curves. We define a spotted light curve as one which includes modulations due to starspots only, faculae only, or starspots and faculae. Starspots and faculae are modelled as discs with three free parameters: radius, intensity, and longitude. Starspot and facula

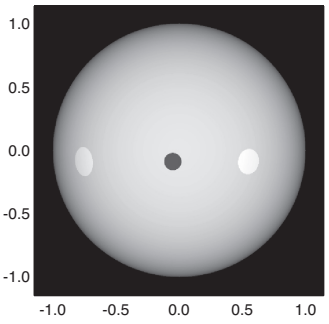

Figure 4. 2D representation of the limb darkened surface of Kepler-71 with one starspot (black) and two faculae (white) inferred from Transit 3 features.

latitudes are that of the projected planetary transit on the surface of the star, which for Kepler-71b is -5.4°, close to the stellar equator given an orbital inclination of 89.56°.

Radius and intensity may be inferred from the width and amplitude of modulations. Longitude is calculated from the estimated time at the centre of a modulation. Starspot/facula longitude is defined relative to the stellar topocentric longitude, 0°, which is the centre of the projection of the planet on to the stellar disc at mid-transit ($t = 0$). Longitudes are constrained to $\pm 80^\circ$ of disc centre to avoid measurement inaccuracies caused by the steep variations in intensity during ingress and egress, i.e. near the limb (Silva-Valio et al. 2010). Longitude is converted from transit time to stellar longitude by

$$\mathrm{lon}_{\rm spotfac} = \arcsin\left[\frac{a\cos\left(90^\circ - \frac{360^\circ}{24}\frac{t_s}{P_{\rm orb}}\right)}{\cos(\mathrm{lat}_{\rm tran})}\right] \tag{4}$$

where a is the semimajor axis, $P_{\rm orb}$ is the orbital period, $\mathrm{lat}_{\rm tran}$ is the transit latitude, and t_s is the time at bump maximum height or dip maximum depth.

Starspots and/or faculae are modelled for each observed transit of Kepler-71 having the signatures of magnetic activity. The number of starspots and faculae added to the model noiseless light curve can vary per transit. For the majority of transits, we found that a maximum of four magnetic features per transit could be distinguished from noise and added to an unspotted model. The unspotted model is visually compared to each observed transit, and the flux residuals remaining after subtraction of the spotless model from observed data are compared to the transit noise to verify that starspot and facula signatures are discernable from the noise (see discussion in Section 4.1). For those transits having starspot and/or facula modulations that pass our selection criteria (discussed in Section 4.1), estimates for those modulations are added to the unspotted model on a per transit basis to create a spotted light curve unique to each observed transit. An example of the 3rd transit of Kepler-71 is given in Fig. 2. The top panel depicts the observed transit, smoothed every 10 points, with an overlay of the unspotted transit model in red. As shown in the bottom panel, the residuals obtained when subtracting the unspotted model from the observed light curve indicate magnetic features that are distinct from the noise. Estimates for the radius, intensity, and longitude of each feature are added to the unspotted model to build a spotted model. A two-dimensional representation of the stellar surface is given in Fig. 4. The dark starspot and two bright faculae are pictured on a limb darkened simulation of the stellar surface.

Table 4. Uniform priors for starspots and faculae.

Parameter	Value
Starspot	
Radius (R_{planet})	[0.2, 2.0]
Intensity	[0, .99]
Longitude	[−80, 80]
Facula	
Radius (R_{planet})	[0.2, 2.0]
Intensity	[1.01, 1.50]
Longitude	[−80, 80]

For each starspot and facula, the radius is defined in units of planetary radius R_p, and the intensity is constrained from 0 to less than 1 for starspots and from greater than 1 to 1.5 for faculae [in units of central stellar intensity I_c ($\mu = 1$)]. Initial fit starspot and facula parameters are set to mid-range values for radius and intensity, 1.0 R_p and 0.5 I_c ($\mu = 1$) for starspots and 1.0 R_p and 1.25 I_c ($\mu = 1$) for faculae. Initial fit longitude at the centre of each magnetic feature is estimated by equation (4) above. Starspot and facula physical characteristics are added to the unspotted model light curve at their estimated central longitudes. Best fit of the observed and synthesized spotted light curve for each transit was performed using GWMCMC. Starting with initial values for starspot and/or facula parameters, GWMCMC simultaneously optimized the three degrees-of-freedom (radius, intensity, and longitude). The uniform priors for the parameters are given in Table 4. The GWMCMC sampling yielded median values for starspot/faculae parameters from which high probability spotted light curves unique to each magnetically active transit can be synthesized.

4 RESULTS

Assuming solar-type activity, we anticipated both the presence of starspots at longitudes along the transit chord from the central meridian to the stellar limbs and the observation of faculae closer to the stellar limbs. Yet, many bright regions were discovered along the transit chord away from the stellar limb.

Magnetic activity, such as starspots and/or faculae, was observed in several of the 117 complete transits for Kepler-71. For many transits with magnetic activity, the out-of-transit noise was equal to or greater than the in-transit flux residuals resulting from subtraction of an optimized model light curve. Thus, the noise masked many starspot and facula signatures and reduced the number of identifiable starspots and faculae. Light curves were examined over a span of ±6 h from mid-transit time (= 0) to compare out-of-transit flux changes to those within the transit, which has a duration of 2.77 h.

Given that the stellar rotation rate and planetary orbital period are in an approximate 1:5 resonance, transit light curves in sequences of every fifth transit were analysed to accentuate any starspot and/or facula signatures. The light curves from transits 186, 191, 196, and 201 are shown as the top four curves in Fig. 5. The transit epoch in BKJD at mid-transit is included, indicating the five orbital period intervals of approximately 19.5 d between transits.

The light curves within the transit, bounded by the vertical solid lines in Fig. 5, show two magnetic features, a starspot at time 0.5h and a faculae at −0.5 h (times refer to the bottom transit shown in black with centre at 1320.5597 BKJD). Since the noise of transit data is significant, the light curves of the four transits were averaged to accentuate the features. As the rotation period of the star is slightly larger than five times the planetary orbital period, each transit had to be shifted in time by 0.06 h accordingly. The displacement corresponds to a stellar rotation period of 19.71 d at the transit latitude. Thus, the dashed lines indicating the starspot and facula appear somewhat slanted. The averaged light curve after the time correction is shown as bottom curve of the figure. As can be seen, the noise outside the transit decreased by a factor of 2 while the two features remained.

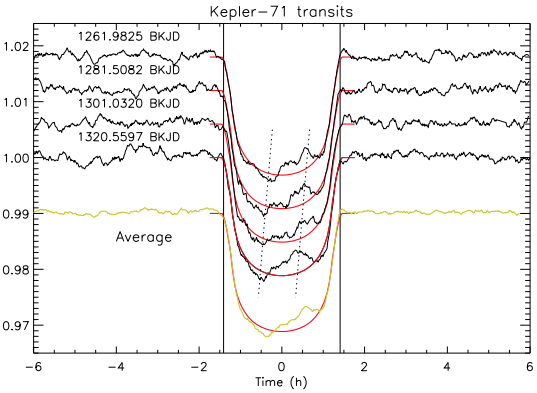

Figure 5. In black, light curves for a sequence of every fifth transit in descending order: Transit 186, Transit 191, Transit 196, and Transit 201, with mid-transit time of each transit given in BKJD. The solid red curves represent the model transit of an unspotted star. The vertical lines mark ingress and egress. The bottom curve (yellow) is an average of all four transits after each is shifted by 0.06 h. The slanted dashed lines cross the positions of a starspot and a facula in the four transits.

The starspot and the facula proved to be occulted during 15 consecutive planetary rotations. Due to their persistence, these magnetic features were accepted as confirmed. Their lifetimes are at least 60 d.

4.1 Modelling starspots and faculae

We visually compared each of the transit light curves of Kepler-71 to an overlay of the model light curve to search for indications of starspots/faculae. For those transits showing potential magnetic variations, the residuals resulting from the subtraction of the GWMCMC optimized model transit light curve from observed transit data were evaluated. Residuals indicating starspots and/or faculae had to meet one the following criteria before being fit via GWMCMC to obtain values for starspot/facula radius, longitude, and intensity: (1) residuals exceed ±100 per cent of the unsmoothed out-of-ransit rms, (2) residuals meet or exceed ±66 per cent of the rms with overall transit noise within ±66 per cent of the rms, or (3) residuals meet or exceed ±66 per cent of the rms and the magnetic feature(s) is(are) repeated every fifth transit.

Fig. 6 for Transit 34 depicts examples of the transit light curve with an overlay of the model and the flux residuals as compared to ±66 per cent and ±100 per cent of the rms. This figure also illustrates the noise in the observed light curves and the difficulty of discerning magnetic features from that noise. The upper panel shows flux variations in the observed light curve when compared to the model light curve. There appear to be a starpots at $t = -0.75$ and a facula at $t = 0.8$ h.

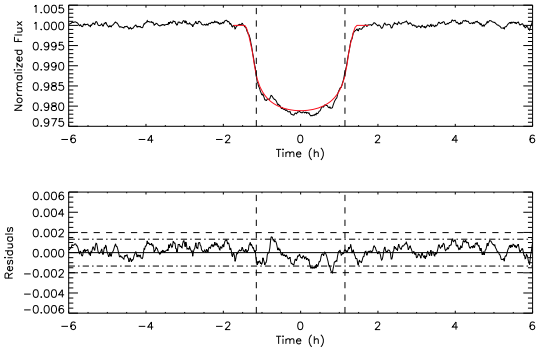

Figure 6. *Top:* Example of the light curve for Transit 34 (transit epoch 668.4125 BKJD) with a starspot at t = -0.75 h and a facula at t = 0.8 h. The smooth, u-shaped curve represents a spotless model. The vertical dashed lines highlight the area of interest. *Bottom:* Residuals after the subtraction of the spotless model from the transit light curve. The dot-dashed lines represent ±66 per cent of the unsmoothed out-of-transit rms, whereas the dashed lines represent ±100 per cent of the unsmoothed out-of-transit rms.

Table 5. Transit distribution of starspots and faculae.

Magnetic feature	No. of transits	Singlet	Doublet	Triplet	Quadruplet
Starspots and faculae	21	0	10	9	2
Starspots only	34	21	13	0	0
Faculae only	17	8	9	0	0

Singlets are defined as only one starspot or facula per transit. Doublets are defined as either two faculae, two starspots, or one starspot and one facula per transit. Triplets are defined as either one starspot and two faculae or two starspots and one facula. Quadruplets are defined as two starspots and two faculae or three starspots and one facula.

The flux residuals in the lower panel of Fig. 6 are plotted against both ±66 per cent and ±100 per cent of the unsmoothed out-of-transit rms. When applying the above criteria, the starspot at -0.75 h and the facula at 0.8 h fail to meet criteria 1, having residuals just below ±100 per cent of the rms. The residuals do, however, pass criteria 2 since they are between ±66 per cent and ±100 per cent of the rms and the out-of-transit noise is well contained within ±66 per cent of the rms. Criteria 3 can only be applied successfully to the spot residual since it meets the rms requirement and reappears in a sequence of every fifth transit at a temporally shifted position.

Magnetic features that either met an out-of-transit rms threshold for individual transits or were occulted during consecutive planetary rotations were modelled as described in Section 3. In total, 76 starspots and 52 faculae were identified in the observed transit light curves and modelled using GWMCMC. Of the 21 transits with a starspot-facula doublet, triplet, or quadruplet, 13 transits had starspot-faculae adjacent pairs. The remaining starspots and faculae were spatially separated. Twenty-nine transits contained a single starspot or facula. Nine transits had just 2 faculae, and 13 transits had only 2 starspots. The distribution of starspots and faculae among the 72 transits is summarized in Table 5.

Histograms of starspot and facula physical parameters are given in Fig. 7. Mean starspot radius is 0.61 ± 0.32 R_p, or (51 ± 26) × 10^3 km. Starspot radii fall within the range of 0.24–1.66 R_p, or (20–138) × 10^3 km. Mean starspot intensity is 0.55 ± 0.23 I_c, where $I_c(\mu = 1)$ is the central intensity of the photosphere. Starspot intensity falls within the range of 0.01–0.92 I_c. Starspot longitudes span −80° to 57°, where 0° longitude corresponds to the central meridian of Kepler-71 at mid-transit in the reference frame of the observer on Earth. As can be seen from the longtiude histogram, the spots longitude distribution is bell shaped and centred around zero longitude.

The mean facula radius is 0.80 ± 0.31 R_p, equivalent to (67 ± 25) × 10^3 km, 31 per cent larger than the mean starspot radius. Facula radii fall within the range of 0.42–1.98 R_p, or (35–165) × 10^3 km. Mean facula intensity is 1.19 ± 0.09 I_c. Facula intensity falls within the range of 1.08 to 1.50 I_c, with intensity greatest towards the stellar limb. Facula longitudes span −58° to 64°. As compared to the spots longitude distribution, the faculae longitude distribution is not centred about zero longitude, with many faculae closer to the stellar limb. Spots are more concentrated towards the centre of the stellar disc, whereas the faculae tend to occur closer to the limb with peaks in the distribution around ±50°. This behaviour is similar to that observed for solar faculae.

The area coverage of the magnetic features was estimated considering the radius of starspots and faculae and the total stellar area occulted by the planet during its transit. The results are plotted in Fig. 8. The starspots (red histogram) occupy about 4.3 per cent of the area of the transit latitudes, approximately two thirds the area occupied by faculae (black histogram). Thus, the average ratio of the faculae to spot area, Q, is 1.7, which is smaller than that for the Sun (Q = 9; Lanza 2010). However, solar-like stars that are more active than the Sun have typically smaller contribution from the facular area: Q = 1.5 for CoRoT-2 (Lanza et al. 2009a) and CoRoT-6 (Lanza et al. 2011), Q = 1.6 for Kepler-17 (Bonomo & Lanza 2012), and Q = 4.5 for CoRoT-4 (Lanza et al. 2009b).

To further evaluate the effective brightness of faculae along the transit chord, facula intensity was converted to flux using the following equation

$$F_{fac} = r_{fac}^2 (I_{fac} - 1), \quad (5)$$

where r_{fac} and I_{fac} are facula radius and intensity, respectively.

Similarly, the starspot flux can be estimated by

$$F_{spot} = r_{spot}^2 (1 - I_{spot}), \quad (6)$$

where r_{spot} and I_{spot} are spot radius and intensity, respectively.

The flux values, in arbitrary units, with longitude for both starspots (red diamonds) and faculae (black asterisks) are plotted in the bottom panel of Fig. 9. As can be seen in the figure, facula flux surplus increases towards the limb more prominently than the spot flux deficit. The trend significantly steepens for longitudes larger than ±45°, indicating a solar-like trend. The starspot flux does not follow a strong increase in value with longitude, as would be expected.

The intensity of the 52 modelled faculae is shown in the top panel of Fig. 9. The solid black line is a model for the increase of solar faculae intensity towards the limb given by $1 + c_f(1 - \mu)$, where $\mu = \cos(\theta)$ is the cosine of the heliocentric angle and c_f = 0.115 to represent the increase of solar faculae at the limb. The blue line is this same equation with a factor of 0.2 in intensity added, showing that the Kepler-71 faculae, despite being brighter than the solar counterparts, follow a similar increase when seen closer to the limb. Thus, the faculae found on Kepler-71 are approximately 20 per cent brighter than their solar counterparts near disc centre.

Criscuoli, Norton & Whitney (2017) studied the photometric properties of network and faculae observed on the Sun using restored images from the Helioseismic Magnetic Imager. For the purposes of their study, magnetic features were classified by their distance from active regions. They found that the network exhibits

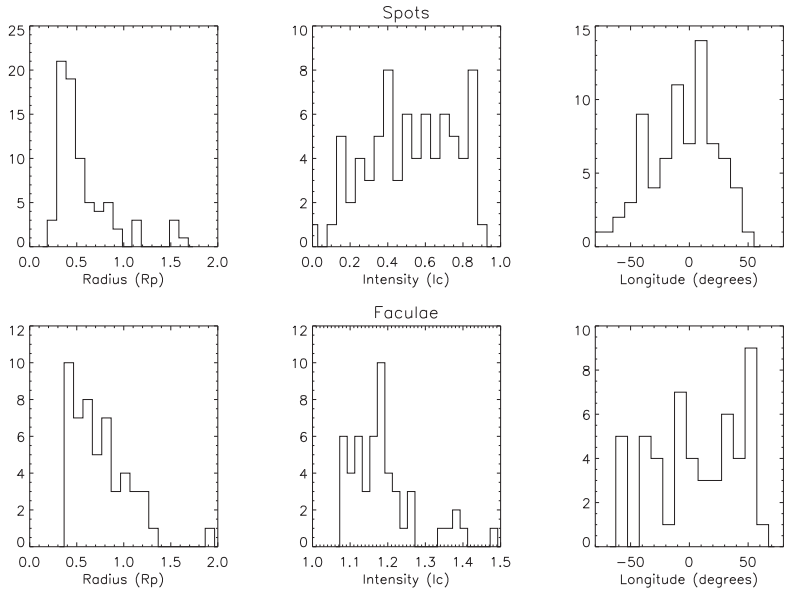

Figure 7. Histograms of starspot (top row) and facula (bottom row) physical parameters (from left to right): radius, intensity, and longitude.

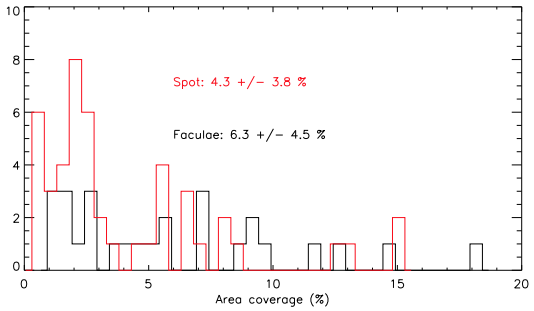

Figure 8. Histograms of the area coverage of starspots (red) and faculae (black). The inset values are the relative areas occupied by starspots and faculae at the transit latitude band.

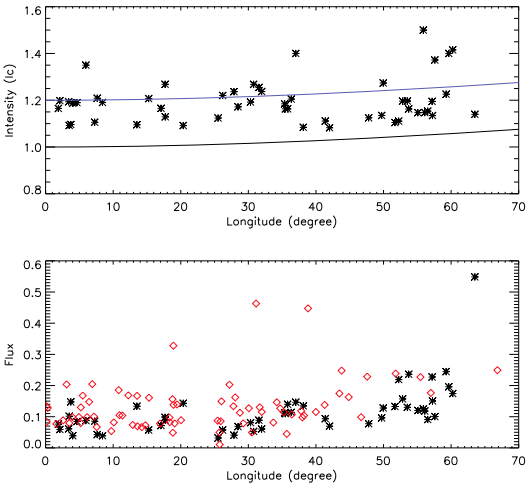

Figure 9. Top: Faculae intensity with longitude. The solid black line represents the dependence of solar facula intensity on heliocentric angle, whereas the blue line is this model with an extra 0.2 added for the case of Kepler-71. Bottom: Facula (black asterisk) and spot (red diamond) fluxes as a function of stellar topocentric longitude.

higher contrasts than faculae, with contrast differences smaller towards disc centre and increasing towards the limb. The contrast is especially high for magnetic flux larger than 300 G, being twice as much for features close to the limb.

Kobel, Hirzberger & Solanki (2018) concur that faculae contrast increases towards the limb but differ as to the contrast near disc centre. Using *G*-band and G-continuum filtergrams from the 1m-Swedish Solar Telescope, they evaluated the properties of photometric features classified as bright points or faculae with respect to heliocentric angle and found that the centre-to-limb variations for both bright points and faculae is non-zero at disc centre and increase with an equivalent trend towards the limb. While the orientation of faculae towards the limb were radial, the orientation near disc centre showed a varied distribution in direction, indicating a hot wall effect induced by inclined fields. Such fields would produce an inclined view of the facular wall. We propose that the faculae observed on Kepler-71 near disc centre are due to very strong and/or inclined magnetic fields.

4.2 Rotation period at the transit latitude

The movement of starspots in and out of the observer's view with stellar rotation has been used to measure the stellar rotation rate

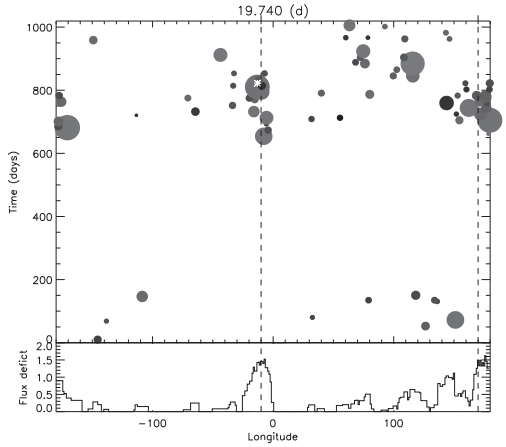

Figure 10. Top: A spot map of the stellar surface with time, i.e. the location of spot longitudes in the rotating frame of the star (with a latitudinal rotation period of 19.74 d) for all transits. The size of the circles represents starspot radius. The spot marked by asterisks is discussed in Section 4.3. Bottom: The total flux deficit caused by the spots. The dashed vertical lines are 180° apart in longitude and roughly indicate the maximum of the spot flux deficit.

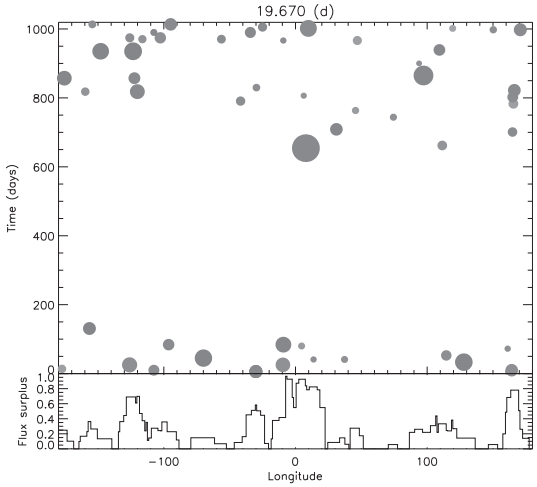

Figure 11. Same as Fig. 10 but for faculae with a stellar rotation period of 19.67 d at the transit latitude. Bottom: Faculae excess flux as a function of longitude.

at the transit latitude and estimate the stellar surface differential rotation (Silva-Valio & Lanza 2011; Valio 2013; Netto & Valio 2016; Valio et al. 2017). The procedure used in those studies employed autocorrelation of flux deficit, the intensity difference due to the presence of spots at different longitudes, to determine stellar rotation rate at the transit latitude. The period was taken as that which corresponded to the autocorrelation function (ACF) with the smallest FWHM.

To estimate the stellar rotation period at the transit latitude, we first considered the 76 starspots identified for all transits. The FWHM of the ACF of the flux deficit caused by the presence of the spots calculated for several latitudinal rotation periods yields a rotation period of 19.74 ± 0.05 d. This rotation period corresponds to the minimum width and is, thus, assigned to the rotation period of the star at latitude −5.4° as far as starspots are concerned. Once the stellar rotation period at the transit latitude band has been calculated, a map of the spot locations in time may be built. Such a map is shown in Fig. 10 for $P_{\rm star}$ = 19.74 ± 0.05 d. Starspot longitudes have been converted from the topocentric coordinate system to one that rotates with the star. The difference in flux estimated by equation (6) is shown in the bottom panel.

The same calculation was performed for the 52 observed faculae. The result is shown in Fig. 11. In this case, the autocorrelation of the flux surplus reaches a minimum at a rotation period of 19.67 ± 0.05 d. The flux surplus estimated by equation (5) is shown in the bottom panel.

The rotation periods estimated here agree with that obtained from the tracking of a facula and a starspot identified in every fifth transit shown in Fig. 5. For these magnetic features to be displayed on the same longitude after five transits, displacements commensurate with a rotation period of 19.71 d were added. Hence, we adopt a latitudinal rotation period of 19.71 d from the mean of the rotation periods calculated for starspots and faculae.

4.3 Obliquity

Since we are detecting the same features in later transits, the obliquity must be very small. However, we cannot use the data from transits five periods apart due to the 1:5 resonance, since the same hemisphere of the star will be facing Earth every five orbital periods, which is approximately $P_{\rm star}$. On the other hand, the fact that we see the same feature on a later transit that is not a multiple of five does prove that the obliquity is close to zero.

To estimate its maximum value, we can use the position of a spot identified on two consecutive transits (208 and 209) at longitude −13° in the frame that rotates with the star, marked by asterisks on Fig. 10 (both spots are overlaid and cannot be discerned in this figure due to the vertical scale). However, as seen from Earth, the topocentric longitudes are −29.5° and +41.8° for transits 208 and 209, respectively. These transits are plotted in Fig. 12 with the spot signatures marked by dashed vertical lines and separated by about 1.4 h, which corresponds to 71°. During each planetary orbit, the star rotates $360^\circ P_{\rm orb}/P_{\rm star} = 71^\circ$.

The planet radius, $R_{\rm p}$, is $0.1358\,R_{\rm star}$, and so the planet eclipses about $2\,R_{\rm p}\,90^\circ \sim 24.5^\circ$ in latitude. In the extreme case that the bottom half of the spot is eclipsed in the bottom transit of the figure and then the top half of the spot is eclipsed in the top transit, we have for the obliquity, Ψ:

$$\Psi = \arctan(24.5/431) \sim 3^\circ. \quad (7)$$

Thus, the obliquity of the planet orbit in this case is less than 3°.

4.4 Average rotation period and active longitudes

The rotation period of the star can be determined from the modulation seen in the light curve of the star as dark spots and bright faculae rotate in and out of view. However, this will be an average period since the star rotates differentially. This average rotation period can be estimated from the out-of-transit light curve.

To confirm the mean stellar rotation period of 19.77 d obtained previously by McQuillan et al. (2013), we applied the autocorrelation technique for period detection described in McQuillan et al.

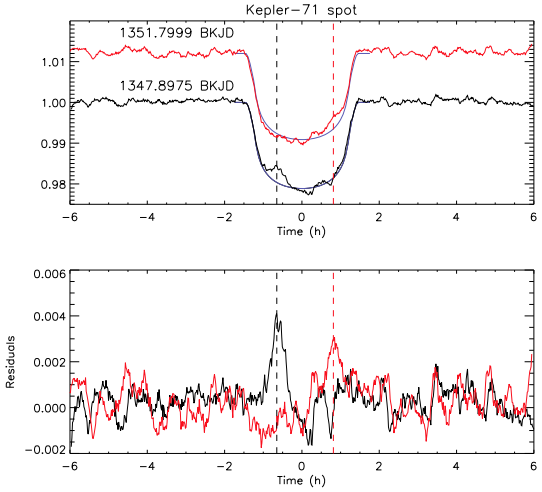

Figure 12. Top: Repeat presence of a spot in two consecutive transits, as indicated by the dashed vertical lines. The bottom light curve is Transit 208 (black curve), whereas the top curve is consecutive Transit 209 (red curve). Mid-transit time is given in BKJD. The solid curve is an unspotted model. Bottom: Residuals after subtraction of the spotless model from the transit light curves, The vertical lines mark the spot signatures in the residuals for Transits 208 and 209. The temporal separation of the occurrences of the spot is 1.4 h or approximately 71°.

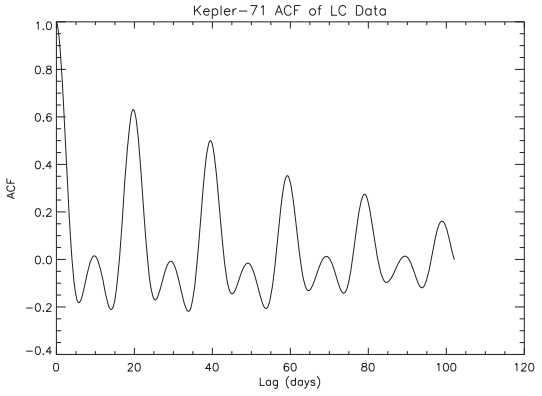

Figure 13. ACF of LC data for Quarters 3–16 after removal of transits. The series of high peaks indicate the stellar rotation period, while the series of low peaks reflect a secondary period possibly due to opposing active longitudes.

(2014) to LC data for Quarters 3–16. McQuillan et al. (2013) utilized the light curves from Quarters 3–14 to arrive at a rotation period of 19.768 ± 0.096 d. We additionally considered the data from full Quarters 15 and 16 but did not include the data from Quarter 17 due to the early termination of that quarter caused by reaction wheel failure. All transits were removed from the LC data before normalizing each quarter and re-gridding the complete data set in continuous time-steps of 29.4 min. The output of the ACF is given in Fig. 13. The ACF clearly shows two distinct periods. The series of high peaks are indicative of the stellar rotation period, while the low peaks reflect a secondary period possibly caused by opposing active regions. The slopes of straight lines fit to the first four peaks for each period yield rotation periods of 19.773 ± 0.008 d and 9.92 ± 0.05 d. We are, thus, confident in a mean stellar rotation period of 19.77 d for Kepler-71.

The peak at 9.92 d is most likely a harmonic of the stellar rotation frequency that corresponds to the 19.77 d period. Such a harmonic may occur when there are active longitudes on the surface of the star, where spots tend to appear, separated by 180° degrees in longitude.

To search for active longitudes on the surface of the star, we examined the stellar surface maps at the transit latitude for both magnetic features, starspots and faculae (Figs 10 and 11). The spot map in Fig. 10 indicates the presence of active longitudes. To guide the eye, vertical dashed lines have been drawn roughly matching the peaks in flux deficit . The flux deficit peaks at approximately -10° and 170°, displaced by 180°. Thus, we confirm the second peak in the ACF at 9.92 d.

4.5 Differential rotation

All the stellar rotation periods calculated above at latitude −5.4° are shorter than the out-of-transit period of 19.77 d. Assuming that the rotational profile is similar to that of the Sun, we calculated the differential rotation of Kepler-71 by fitting the estimated latitudinal rotation period to a solar profile. Differential rotation of the Sun is described by the following simplified solar law.

$$\Omega(\alpha) = \Omega_{\rm eq} - \Delta\Omega\ \sin^2(\alpha), \tag{8}$$

where Ω is the angular velocity, $\Omega_{\rm eq}$ is the equatorial angular velocity, $\Delta\Omega$ is rotational shear, or the difference in angular velocity between the equator and pole, and α is stellar latitude.

Assuming a similar profile for Kepler-71, the equatorial angular velocity and rotational shear can be estimated by fitting a generic differential rotation profile.

$$\Omega(\alpha) = A - B\ \sin^2\alpha \tag{9}$$

where A and B are the stellar equatorial angular velocity and rotational shear, respectively.

The average rotation is obtained by integrating equation (9) from the minimum latitude to the maximum latitude where spots (or faculae) emerge.

$$\bar{\Omega} = \frac{1}{(\alpha_2 - \alpha_1)} \int_{\alpha_1}^{\alpha_2} \left(A - B\ \sin^2\alpha\right) {\rm d}\alpha, \tag{10}$$

where α_1 and α_2 are the minimum and maximum latitudes, respectively. For the Sun, we can assume that spots emerge from latitudes near the equator to a maximum of ±35°. Young stars have spots all the way to the poles, i.e. from 0° to 90° latitudes.

Thus we have two equations, given by the rotation at the transit latitude (equation 9) and the average out-of-transit rotation (equation 10), and two unknowns, A, the rotation at the equator, and B, the shear. Considering that the minimum latitude of spot (or faculae) occurrence is the equator, we now have to estimate the maximum latitude for the magnetic features.

Similar to the Sun, the emergence of starspots on Kepler-71 should replicate the butterfly trend of sunspots, appearing within latitude bands on either side of the solar equator. The rotation of stars younger than the Sun with shorter rotation periods will produce a Coriolis force that deflects flux tubes to higher latitudes (Granzer 2004). The mean stellar rotation period of Kepler-71 is approximately 75 per cent of that for the Sun, and thus, the maximum emergence latitude of spots on Kepler-71 will be greater than

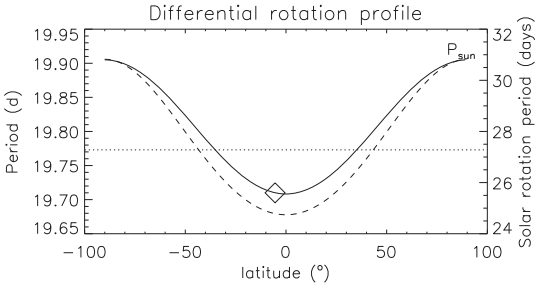

Figure 14. Differential rotation profiles for Kepler-71 (solid line) and the Sun (dashed line). The diamond represents the period of 19.71 d at latitude −5.4° found from temporal starspot and facula mapping.

solar. For a star with equivalent solar mass, the maximum emergence latitude will be ±65°.

The differential rotation profile we generated for Kepler-71 over the latitude range [0.0°, 65.0°] using the mean stellar rotation period of 19.71 d at the transit latitude of −5.4° is depicted in Fig. 14. The diamond marks the profile location for transit latitude −5.4° and rotation period 19.71 d. Considering the rotation of 19.74 d obtained from spots, we calculate a rotational shear of $\Delta\Omega = 0.0015 \pm 0.0025$ rad d^{-1} and a relative differential rotation of $\Delta\Omega/\bar{\Omega} = 0.5 \pm 0.8$ per cent, where $\bar{\Omega} = 2\pi/P_{\rm star}$ and $P_{\rm star}$ is the out-of-transit mean stellar rotation period of 19.77 d. If we consider the slightly smaller rotation period obtained from faculae only, 19.67 d, the shear is $\Delta\Omega = 0.0052 \pm 0.0025$ rad d^{-1} with a relative differential rotation of $\Delta\Omega/\bar{\Omega} = 1.6 \pm 0.8$ per cent. Hence, Kepler-71 star apparently has very little differential rotation.

5 DISCUSSION

Kepler-71b is a hot Jupiter orbiting a solar-type G-star younger than the Sun. The mean stellar rotation period of Kepler-71 at 19.77 d is consistent with that of a G-class star somewhat younger than the Sun (Guinan & Engle 2009). Rotational evolution of main-sequence stars is closely related to changes in angular momentum. In particular, the proximity of hot Jupiters to their host stars contributes to significant angular momentum loss in G-type stars and as such affects the early evolution of stellar rotation (Lanza 2010). The orbit of a hot Jupiter through the closed magnetic field lines of the stellar corona of its host star induces a greater loss of angular momentum through coronal mass ejections rather than through a magnetized wind. As a star ages and slows, the effect of the hot Jupiter may not be as impactful. The current rotation rate of Kepler-71 may be assigned to early coronal mass eruptions followed by angular momentum loss through stellar winds. Lanza (2010) observed trends in the synchronization of stellar rotation and planetary orbit relative to stellar effective temperature. For cool stars with $T_{\rm eff} < 6000$ K, the stellar rotation period is much longer than the planetary orbital period, and the spin–orbit synchronization ratio can be as great as 1:6 (Lanza 2010). Kepler-71 is a cool star at $T_{\rm eff} = 5540$ K. The synchronization ratio of the Kepler-71 system is approximately 1:5, given a mean stellar rotation period of 19.77 d and planetary orbital period of 3.91 d, and exemplary of the trend observed by Lanza.

The photometric variations of Kepler-71 are characteristic of a solar-type star with an internal magnetic dynamo driven by the interplay of stellar rotation and plasma convection. We have estimated the stellar rotation period and derived therefrom differential rotation of Kepler-71 at the transit latitude of −5.4° by mapping the positions of faculae and starspots along the transit chord. The stellar rotation period at the transit latitude, as determined by the longitudinal change in position of faculae, is 19.67 ± 0.05 d, slightly smaller than the mean stellar rotation period of 19.77 d. Further, the value for differential rotation from faculae is supported by the differential rotation derived from the mapping of starspots. The stellar rotation period calculated from the longitudinal movement of starspots yields a rotation period of 19.74 ± 0.05 d, again less than the mean stellar rotation period of 19.77 d. Thus, the rotation period from faculae and that from starspots are complementary, differing by less than 1 per cent. Given the latitudinal rotation periods derived for faculae and starspots, we calculate a rotational shear bounded by $\Delta\Omega = 0.0015$ and 0.0052 rad d^{-1} and a relative differential rotation within $\Delta\Omega/\bar{\Omega} = 0.5$ per cent and 1.6 per cent.

The rotational shear of Kepler-71 is significantly smaller than the solar value of 0.055 rad d^{-1} (Berdyugina 2005) and indicative of likely rigid body rotation. Recent stellar models, e.g. the Küker & Rüdiger (2011) models, predict the variation of rotational shear with temperature but are lacking to predict the relationship between shear and rotation rate for G-stars (Balona & Obedigamba 2016). Observational data differs from predicted values. Reinhold et al. (2013) calculated the differential rotation of *Kepler* stars by associating Lomb–Scargle periods from light curves of different *Kepler* quarters with a secondary period being within 30 per cent of the primary rotation period. Assuming that changes in stellar rotation period are due to the appearance of starspots at differing latitudes between quarters, Reinhold et al. (2013) computed differential rotation values for more than 18 000 stars. Similar to the values presented by Barnes et al. (2005), the computations indicate a weak dependence of rotational shear $\Delta\Omega$ on rotation period and a slight increase in $\Delta\Omega$ over the temperature range $T_{\rm eff} = 3500$–6000 K. The values of rotational shear are bounded by the lower detection limit of 0.03 rad d^{-1} due to the subset of stars having only one detectable period. Instrumental effects of the *Kepler* telescope for slow rotators reduce the ability to detect a secondary period. Still, the values from Reinhold et al. (2013) demonstrate the weak correlation of rotational shear and rotation rate proposed by Küker & Rüdiger (2011), who modelled the rotational shear for Zero-Age Main-Sequence (ZAMS) stars of varying solar masses. From $T_{\rm eff} = 5400$–6800 K, there is a steady increase in rotational shear with temperature. At $T_{\rm eff} = 5500$ K, the predicted rotational shear is approximately 0.01 rad d^{-1} for a ZAMS star.

Unlike the photometric method of Reinhold et al. (2013), which is based upon the overall motion of magnetic features to set a lower limit on differential rotation, we have employed the technique of transit photometry mapping to characterize individual starspots and faculae and trace their positions along the transit latitude. We consider our value of differential rotation to be accurate though the result is lower than seen in other studies.

While the evidence for a rigidly rotating solar-type star younger than the Sun is perhaps surprising, various researchers offer physical mechanisms for this type of behaviour. Relatively rigid rotation may be attributed to processes that include angular momentum transport during Kepler-71's evolutionary development, planet–star interactions, or the generation of stresses in the convective zone. Adopting a model in which the radiative core and convective zones rotate at different rates as a result of angular momentum loss in the convective zone due to magnetized stellar winds, MacGregor & Brenner (1991) proposed that angular momentum transport in the stellar interior acts to redistribute angular velocity

at the tachocline. The time-scale during which angular momentum is transferred between the radiative core and convective zone, i.e. the core-coupling time-scale, and the amount of angular momentum exchanged affect the angular velocity gradients at the tachocline. A short coupling time-scale infers an efficient transfer of angular momentum, resulting in rigid body rotation (Bouvier 2013).

Kepler-71b is a hot Jupiter orbiting its host star at a distance of 0.047 au in a circular orbit. The planet and star each exert forces on its companion. In particular, the planet's gravitational potential generates a stellar tidal flow and may additionally be responsible for inertial waves in the convective zone. While the tidal force has been studied as to its effects on the evolution of the planet–star system structure, the effect of inertial waves on Sun-like stars and the interplay between internal stellar oscillation modes and differential rotation are new areas of investigation (Guenel et al. 2016).

The solar dynamo model states that magnetic fields generated at the tachocline are frozen in the convective zone plasma. The movement of the ionized plasma through the magnetic field creates electric currents. The magnetic field will in turn react back on the current flow through the Lorentz force. The reactive magnetic field may inhibit differential rotation (Ammler-von Eiff & Reiners 2012), resulting in lower measurements of differential rotation.

With respect to the large-scale electromagnetic fields, Varela, Strugarek & Brun (2016) propose that Maxwell stresses will decrease differential rotation due to their quenching effect on stellar magnetic fields. Varela et al. (2016) simulated the differential rotation of G and K solar-type stars of varying masses and rotation rates under the effect of magnetic fields and found that the interplay of angular momentum redistribution in the convective zone and changes in the magnetic field may cause differential rotation to become rigid. The latitudinal component angular momentum flow of meridional circulation is subject to Coriolis forces and turbulent Reynolds and Maxwell stresses. Maxwell stresses weakening the magnetic field are opposed by Reynolds stresses resulting in variance of the magnetic field and differential rotation. The differential rotation of Kepler-71 may be evidence of dominant Maxwell stresses.

There are, indeed, multiple ways to explain the almost rigid rotation observed. Given the potential impacts of core-coupling, star–planet interaction, Lorentz force effects, and Maxwell stresses, the essentially rigid rotation observed suggests that one or more of these physical mechanisms may be at work in the Kepler-71 system.

6 CONCLUSIONS

We have estimated the differential rotation of Kepler-71 by correlating the facula and starspot activity observed in sequential transits of Kepler-71b. Using the transit model described in Silva (2003), we detected and characterized 76 starspots and 52 faculae in 117 complete transits of Kepler-71 for 7 *Kepler* quarters. The photometric data noise limited the number of starspots and faculae which were discernable.

Our analysis presents the first use of faculae to measure stellar rotation period. The evidence of faculae, bright features seen on the transit light curves as a decrease in intensity as the planet transits over them, can be assured by (i) an increasing flux for faculae closer to the stellar limb, (ii) differing longitude distribution for spots and faculae, the latter being more prone to be detected closer to the limb, (iii) the area ratio of facula to spot is approximately 2, similar to the ratio found for solar-like active stars, and (iv) the rotation period estimated from faculae only is within 1 per cent of that obtained from spots. The properties listed as (i) and (ii) are those observed for solar faculae.

From autocorrelation of flux surplus for faculae as a function of longitude, we estimate the stellar rotation period to be 19.67 ± 0.05 d at the transit latitude. Autocorrelation of flux deficit for starspots yields the value 19.74 ± 0.05 d, within 1 per cent of the rotation period from faculae. Further, monitoring the signature of faculae and spots on four transits separated by five orbital periods each yields the rotation period of 19.71 d, whereas the out-of-transit mean rotation period is 19.77 d. Assuming a solar-like differential rotation profile (with increased rotation period away from the stellar equator), we calculate from faculae a weak rotational shear of $\Delta\Omega = 0.0052 \pm 0.0025$ rad d^{-1} and a relative differential rotation of $\Delta\Omega/\bar{\Omega} = 1.6 \pm 0.8$ per cent. The rotational shear and relative differential rotation calculated from spots yield similar values, $\Delta\Omega = 0.0015 \pm 0.0025$ rad d^{-1} and a relative differential rotation of $\Delta\Omega/\bar{\Omega} = 0.5 \pm 0.8$ per cent. Such low shear is in agreement with the presence of active longitudes that may be inferred from the spot transit mapping.

The rotational shear of Kepler-71 is relatively low as compared to the modest solar value of 0.055 rad d^{-1}. Multiple mechanisms which may result in the comparatively rigid rotation of Kepler-71 should be considered as contributors to this solar-type star's remarkably low differential rotation as compared to that of the Sun today.

ACKNOWLEDGEMENTS

The authors thank the anonymous referee for comments and suggestions that extended calculations and improved the content herein.

We also thank P. Wilson Cauley for providing an IDL implementation of the Goodman & Weare Monte Carlo Markov Chain.

AV acknowledges partial financial support from the Brazilian Research Funding Agency of the São Paulo State (FAPESP), # 2013/10559-5.

This paper includes data collected by the *Kepler* mission. Funding for the *Kepler* mission is provided by the NASA Science Mission directorate. *Kepler* light curve data was obtained from the NASA Exoplanet Archive, which provides public access to *Kepler* Mission data. The primary archive of all *Kepler* data is provided by the Mikulski Archive for Space Telescopes (MAST). STScI is operated by the Association of Universities for Research in Astronomy, Inc,. under NASA contract NAS5-26555. We thank the *Kepler* team for their efforts in providing the data and interfaces used in preparing this paper.

REFERENCES

Aigrain S. et al., 2015, MNRAS, 450, 3211
Ammler-von Eiff M., Reiners A., 2012, A&A, 512, A116
Balona L. A., Abedigamba O. P., 2016, MNRAS, 461, 497
Barnes J. R., Collier Cameron A., Donati J. -F., James D. J., Marsden S. C., Petit P., 2005, MNRAS, 357, L1
Berdyugina S. V., 2004, Sol. Phys., 224, 123
Berdyugina S. V., 2005, Living Rev. Sol. Phys., 2, 8
Bonomo A. S., Lanza A. F., 2012, A&A, 547, A37
Borucki W. J., 2010, Science, 327, 977
Bouvier J., 2013, Observational Studies of Stellar Rotation, EAS Publ. Ser. Vol. 62, Cambridge Univ. Press, Cambridge, p. 143
Carter B. D., , Marsden S. C., Waite I. A., 2015, in van Belle G. T., Harris H. C., eds, 18th Cambridge Workshop, Proceedings of conference held at Lowell Observatory, 8-14 June 2014, Cool Stars, Stellar Systems, and the Sun, p. 209

Christiansen J. L., Jenkins J. M., Caldwell D. A., 2012, PASP, 124, 1279
Covas E., 2017, A&A, 605, A44
Criscuoli S., Norton A., Whitney T., 2017, ApJ, 847, 93
Davenport J. R. A., Hebb L., Hawley S. L., 2015, ApJ, 806, 212
Estrela R., Valio A., 2016, ApJ, 831, 57
Foreman-Mackey D., Hogg D., Lang D., Goodman J., 2013, PASP, 125, 306
Giles H. A. C., Collier Cameron A., Haywood R. D., 2017, MNRAS, 472, 1618
Goodman J., Weare J., 2010, Commun. Appl. Math. Comput. Sci., 5, 68
Granzer. T., 2004, Astron. Nachr., 325, 417
Guenel M., Baruteau C., Mathis S., Rieutord M., 2016, A&A, 589, A22
Guinan E. F., Engle S. G., 2009, Proc. IAU Symp. 258, The Ages of Stars. Kluwer, Dordrecht, 395
Hackman T., Lehtinen J., Rosen L., Kochukhov O., Kapyla M., 2016, A&A, 593, A35
Hathaway D. H., 2015, Living Rev. Solar Phys., 12, 2
He H., Wang H., Yun D., 2015, ApJS, 221, 1
Hogg D. W., Foreman-Mackey D., 2018, ApJS, 236, 11
Holczer T. et al., 2015, ApJ, 807, 170
Howell S. B. et al., 2010, ApJ, 725, 1633
Hubbard A., Rheinhardt M., Brandenburg A., 2011, A&A, 536, A48
Isik E., Schmidtt D., Schussler L., 2011, A&A, 527, A135
Jenkins J. M. et al., 2010, ApJ, 173, L87
Kipping D. M., 2013, MNRAS, 435, 2152
Kobel P., Hirzberger J., Solanki S. K., 2018, preprint (arxiv:1410.5354)
Küker M., Rüdiger G., 2005, A&A, 422, 1023
Küker M., Rüdiger G., 2011, Astron. Nachr., 332, 933
Lanza A. F., 2010, A&A, 512, A77
Lanza A. F. et al., 2009, A&A, 506, 255
Lanza A. F. et al., 2009a, A&A, 493, 193
Lanza A. F. et al., 2011, A&A, 525, A14
MacGregor K. B., Brenner M., 1991, ApJ, 376, 204
Marsden S. C. et al., 2011, MNRAS, 413, 1939
Mathur S. et al., 2016, ApJS, 229, 30
Matt S. P., Do Cao O., Brown B. P., Brun A. S., 2011, Astron. Nachr., 332, 897
Maunder E. W., 1904, MNRAS, 64, 747
McQuillan A., Aigrain S., Roberts S., 2012, A&A, 538, A137
McQuillan A., Mazeh T., Aigrain S., 2013, ApJS, 775, L11
McQuillan A., Mazeh T., Aigrain S., 2014, ApJS, 211, 24
Mehrabi A., He H., Khosroshahi H., 2017, ApJ, 834, 207
Meibom S., Barnes S. A., Platais I., Gilliland R. L., Latham D. W., Mathieu R. D., 2015, Nature, 517, 589
Müller H. M. , Huber K. F. , Czesla S., Wolter U., Schmitt J. H M. M., 2013, A&A, 560, A112
Netto D. Y. S., Valio A., 2016, Young Stars & Planets Near the Sun, Proceedings of the International Astronomical Union, IAU Symp., vol. 314, p. 259
Ortiz A., Solanki S. K., Domingo V., Fligge M., Sanahuja B., 2002, A&A, 388, 1036
Press W. J., Teukolsky S. A., Vetterling W. T., Flannery B. P., 1992, Numerical Recipes in FORTRAN, The Art of Scientific Computing, 2nd edn. Cambridge Univ. Press, Cambridge
Reiners A., Schmitt J. H. M. M., 2002, A&A, 384, 155
Reinhold T., Reiners A., Basri G., 2013, A&A, 560, A4
Shapiro A. I., Solanki S. K., Krivova N. A., Yeo K. L., Schmutz W. K., 2016, A&A, 589, A46
Silva-Valio A., Lanza A. F., 2011, A&A, 529, A36
Silva-Valio A., Lanza A. F., Alonso R., Barge P., 2010, A&A, 510, A25
Silva A. V. R., 2003, ApJ, 585, L147
Smith J. C. et al., 2012, PASP, 124, 919
Spruit H. C., 1997, Mem. Soc. Astron. Ital., 68, 397
Spruit H. C., 2011, in Paz Miralles M., Sanchez Almeida J., eds, The Sun, the Solar Wind, and the Heliosphere, p. 39
Stumpe M. C. et al., 2012, PASP, 124, 984
Thomson, S. E., 2016, Kepler Data Release Notes (KSCI-19065-002)
Uzdensky D. Arons J., Balbus S., Blackman E., Goodman J., Medvedev M., Spitkovsky A., Stone J., 2010, Astro-2010 Decadal Science White Papers, Life Cycles of Magnetic Fields in Stellar Evoltuion
Valio A., 2013, ASP Conf. Ser. Vol. 472, New Quests in Stellar Astrophysics III: A Panchromatic View of Solar-Like Stars, With and Without Planets. Astron. Soc. Pac., San Francisco, 239
Valio A., Estrela R., Netto Y., Bravo J. P., de Medeiros J. R., 2017, ApJ, 835, 2
Varela J., Strugarek A., Brun A. S., 2016, Adv. Space Res., 58, 1507
Waite I. A., Marsden S. C., Carter B. D., Alecian E., Brown C., Burton D., Rhodes H., 2011, MNRAS, 413, 1939

This paper has been typeset from a TEX/LATEX file prepared by the author.

The results from Zaleski et al. (2019) show that the photospheric variability of Kepler-71 is indicative of solar-type dynamo processes. The faculae on Kepler-71 are similar to solar faculae, being more detectable closer to the stellar limbs where their flux intensity is greater. A spot map of the stellar surface shows the existence of active longitudes separated by 180°. The results also demonstrate the first known use of faculae to successfully resolve rotation period. Thus, the rotation period at the transit latitude is measurable from either starspots or faculae.

The unexpected result is the small rotational shear of Kepler-71. When compared to a solar-type differential rotation profile, the results from both starspot and facula analysis indicate a rotational shear less than about 0.005 rad d^{-1}, or a relative differential rotation less than 2%. This rotational shear is lower than the modest shear of the present-day Sun and largely indicative of almost rigid rotation. This limited differential rotation thus raises the prospect of various physical mechanisms such as planet-star interactions, angular momentum transport during planetary development, or stress forces in the convective zone.

> The observer is never entirely replaced by instruments; for if he were, he could obviously obtain no knowledge whatsoever ... They must be read! The observer's senses have to step in eventually. The most careful record, when not inspected, tells us nothing.
>
> Edwin Schrödinger

Chapter 3 Activity and Differential Rotation of the Early M Dwarf Kepler-45

Early in their lives on the main sequence, red dwarf, or M-type, stars possess an internal solar-type structure that is partially radiative and partially convective. M dwarfs are much smaller than the Sun having masses of 0.60 $M_\odot$ for spectral type M0 to 0.08 $M_\odot$ for spectral type M8. At mid-age around spectral type M3V and mass 0.35 $M_\odot$, these stars transition from an $\alpha\Omega$ dynamo to a fully convective α^2 dynamo (Jao et al., 2018).

M dwarfs are cool stars (2000 - 4000 K) that slowly burn hydrogen through thermonuclear fusion. A steady and moderate hydrogen consumption results in a constant but low luminosity that makes M dwarfs difficult to detect in the optical regime. Magnetic activity in the form of flares however can cause large, temporary brightening.

Core-accretion models of planetary formation predict that the existence of Jovian exoplanets is not favored in M dwarf systems due to evolutionary timescales and limited material in the circumstellar disk for the creation of Jupiter-sized planets (Adams et al., 2005; Apai & Pascucci, 2010). A mere 4 hot Jupiters in M dwarf systems have

been discovered: Kepler-45b (Johnson et al., 2012), NGTS-1b (Bayliss et al., 2018), and HATS-71b (Bakos et al., 2018) via transit, and HD41004B-b (Zucker et al., 2003) via radial velocity.

For the study of a solar-stellar connection using Jupiter-hosting cool stars in the *Kepler* dataset, Kepler-45 (M1V, mass $0.59 M_{\odot}$, radius $0.624 R_{\odot}$, T_{eff} = 3820 K) was chosen as the second target star to address the question 'Do the cool early M dwarfs exhibit the activity indicative of a solar-type dynamo?' Though it is a faint star (*Kepler* magnitude K_p = 15.979), the depth of the Kepler-45b's SC transits in combination with a high signal-to-noise ratio allow the examination of the occulted stellar surface at the transit latitude via the interpretation of flux amplitude modulations. From the derived physical characteristics of starspots and faculae along the transit chord, this works presents the premier photometric analysis of stellar activity for an M1V dwarf, to include latitudinal and differential rotation, spot coverage, starspot and facula temperatures, and magnetic activity cycle. Analytic methods and results are set forth in the following paper, "Activity and Differential Rotation of the Early M Dwarf Kepler-45 from Transit Mapping" (Zaleski et al., 2020a).

3.1 Zaleski et al. (2020a) "Activity and Differential Rotation of the Early M Dwarf Kepler-45 from Transit Mapping"

The published paper Zaleski et al. (2020a), "Activity and Differential Rotation of the Early M Dwarf Kepler-45 from Transit Mapping", follows.

Monthly Notices of the ROYAL ASTRONOMICAL SOCIETY

MNRAS **492,** 5141–5151 (2020) doi:10.1093/mnras/staa103
Advance Access publication 2020 January 15

Activity and differential rotation of the early M dwarf Kepler-45 from transit mapping

S. M. Zaleski [1]★ A. Valio,[2] B. D. Carter[1] and S. C. Marsden[1]

[1] *Centre for Astrophysics, University of Southern Queensland, Toowoomba, QLD 4350, Australia*
[2] *Center for Radio Astronomy and Astrophysics, Mackenzie Presbyterian University, Rua da Consolaçao, 896, São Paulo, SP 01302-907, Brazil*

Accepted 2020 January 6. Received 2019 December 17; in original form 2019 October 31

ABSTRACT

Little is known of the activity and differential rotation of low luminosity, early M dwarfs from direct observation. We present the first stellar activity analysis of star-spots and faculae for the hot Jupiter hosting M1V dwarf Kepler-45 from *Kepler* transit light curves. We find star-spot and facula temperatures contrasting a few hundred degrees with the quiet photosphere, hence similar to other early M dwarfs having a convective envelope surrounding a radiative core. Star-spots are prominent close to the centre of the stellar disc, with faculae prominent towards the limbs, similar to what is observed for the Sun. Star-spot and facula mean sizes are about 40 and 45 $\times$ 10^3 km, respectively, and thus faculae occupy a 10 per cent larger surface area than the star-spots. A short-term activity cycle of about 295 d is observed that is reminiscent of those seen for other cool dwarfs. Adopting a solar-type differential rotation profile (faster equatorial rotation than polar rotation), our star-spot and facula temporal mapping indicates a rotation period of 15.520 $\pm$ 0.025 d at the transit latitude of -33.2°. From the mean stellar rotation of 15.762 d, we estimate a rotational shear of 0.031 $\pm$ 0.004 rad d^{-1}, or a relative differential rotation of 7.8 $\pm$ 0.9 per cent. Kepler-45's surface rotational shear is thus consistent with observations and theoretical modelling of other early M dwarfs that indicate a shear of less than 0.045 rad d^{-1} and no less than 0.03 rad d^{-1} for stars with similar stellar rotation periods.

Key words: stars: activity – stars: solar-type – starspots.

1 INTRODUCTION

M dwarfs are the most plentiful stars in the Galaxy. These cool, faint stars, having smaller radii and masses than the Sun, are found throughout the Solar neighbourhood, comprising 70 per cent of the stellar population (Bochanski et al. 2010). M dwarfs fill the lower end of the main sequence on the Hertzsprung–Russell (H–R) diagram with an effective temperature scale of roughly 4000 K for early M dwarfs to 2000 K for late (ultracool) M dwarfs (Rajpurohit et al. 2013). Their abundance and physical properties have made M dwarfs popular targets in the search for Earth-sized and Earth-like exoplanets in the habitable zone, where radiation heating and greenhouse effects favour the existence of liquid water on a planet's surface. Since M dwarfs are small low-mass stars, the ratios of exoplanet radius and mass to stellar radius and mass will be greater than for other cool stars targeted for planet searches. This will produce a more notable flux reduction in photometric time series as a planet blocks light from the star and a larger variation in Doppler measurements of stellar motion.

Radial velocity surveys were the first technique used for discovering planets around M dwarfs. In 1998, the first Jupiter mass planet was discovered orbiting the M dwarf GJ 876 (M4V) (Delfosse, Forveille & Mayor 1998; Marcy et al. 1998). Since then, radial velocity searches including M dwarf stars have been augmented by information from star-spots via targeted photometric follow-up. The presence of star-spots plays a discriminating role in the confirmation of candidate exoplanets orbiting M dwarfs, as well as other stars. The stellar rotation that brings star-spots in and out of view produces photometric variability useful to measure rotation period but will distort absorption line profiles and create radial velocity jitter (Saar & Donahue 1997; Barnes, Jeffers & Jones 2011). Nevertheless, a planet may be identified if its radial velocity signature is greater than spot induced jitter and a stellar rotation period measured from spot modulation can be used to separate the effects of activity from reflex motion due to a planet (Boisse et al. 2011; Diez Alonso et al. 2019).

The *Kepler* mission revolutionized the search for exoplanets by introducing the transit method as a new application of photometry (Borucki 2010). Though the main objective of the *Kepler* mission was to discover Earth-sized planets in the habitable zones of Sun-like stars via the loss of stellar flux due to planetary transits, the abundance of photometric data collected for a vast assortment of

★ E-mail: shelley.zaleski@usq.edu.au

stellar spectral types at different ages has provided for the broad analysis of stellar behaviour. Listed in the NASA Exoplanet Archive are 418 confirmed hot Jupiters from programs including the *Kepler* mission (Thompson et al. 2016). Of those gas giants, 375 transit their host stars. The majority of confirmed hot Jupiters orbit F, G, and K stars (Bakos et al. 2018). The dearth of hot Jupiters found in M dwarf star–planet systems is not surprising in view of a favoured formation of small planets around low-mass, cool stars (Apai & Pascucci 2010). Only five hot Jupiters are known to orbit M dwarfs. Kepler-45b (Johnson, Gazak & Apps 2012), HATS-6b (Hartman et al. 2015), NGTS-1b (Bayliss et al. 2018), and HATS-71b (Bakos et al. 2018) were discovered via transit surveys, whereas HD 41004B-b (Zucker et al. 2003) was discovered from radial velocity measurements.

Kepler-45b transits an M1V dwarf in a single planet system. The Kepler-45 system offers an uncommon opportunity to investigate the magnetic activity of an early M dwarf (a low-mass star hosting a hot Jupiter) through precise measurement of star-spot and facula physical parameters, which include radius, intensity, longitude, and latitude, for those features occulted during planetary transits. The transit depth resulting from the occultation of the stellar surface by a Jovian-sized planet provides the resolution necessary to distinguish the bumps and dips in transit light curves caused by star-spots and faculae, the features appearing in the photosphere that witness the action of an internal dynamo. Moreover, the area coverage of spots, at least within the transit band, can be associated with the observed total out-of-transit variability of the light curve (Basri et al. 2011).

Early M dwarfs, such as Kepler-45, have an internal Sun-like structure comprised of a large convective envelope surrounding a small radiative core. The magnetic activity in stars of this structure is thought to be induced by an $\alpha\Omega$ dynamo. The $\alpha\Omega$ dynamo based on our knowledge of the Sun is the accepted benchmark for magnetic activity in main-sequence F, G, and K solar-type stars (Fabbian et al. 2017). Magnetic fields are stretched by differential rotation (Ω-effect), twisted by the Coriolis force (α-effect), and pumped via magnetic buoyancy to the stellar surface. Magnetic fields appear as cool, dark star-spots and hot, bright faculae. The apparent motion of these emanating regions is driven by stellar rotation. The rotation periods of star-spots and faculae on the surface of solar-type stars vary with latitude. This differential rotation is a fundamental descriptor of the rotation profile of Sun-like stars (Charbonneau 2010). Rotational shear is greatest at the tachocline, the boundary between the radiative and convective zones. A transition from partially to fully convective stars occurs around spectral type M3V, where a notable gap in the H–R diagram marks the conversion from an $\alpha\Omega$ dynamo to an α^2 dynamo (Jao et al. 2018). A fully convective dynamo lacks a tachocline, a fundamental element of a solar-type dynamo model responsible for magnetic field generation. Late-type M dwarfs are also magnetically active (West et al. 2011), but star-spots on the surface of these fully convective stars may instead be due to a magnetic field generated by helical turbulence (Durney, De Young & Roxburgh 1993) or radiative diffusive heat flux (Fan & Fang 2014).

Does a standard for the behaviour of FGK solar-type stars based on stellar age or effective temperature extend to include early M dwarf spectral types? Hartman et al. (2011) propose that the correlation between period and photometric activity for FGK and early M dwarfs is consistent with rotation age–activity mass relations. As FGK stars age, their angular velocity decreases. This results in reduced shearing of magnetic field lines at the tachocline, lessening spot coverage, changes in spot stability, and decreasing differential rotation. M dwarfs also exhibit slowing rotation accompanied by a decline in magnetic activity as their ages increase. However, the trend for solar-type stars is not as pronounced in M dwarfs (Barnes et al. 2011; West et al. 2008, 2011). Slowly rotating early M dwarfs seem to follow the trend of solar-type stars, but their rotation age–activity relation has not yet been well established (Kiraga & Stępień 2011). Changes in stellar age and behaviour do not necessarily occur at the same rates among spectral types. An M dwarf of the same age as a G star will have a longer rotation period due to the faster rotational braking of low-mass stars (Guinan & Engle 2009).

Barnes et al. (2005) and Balona & Obedigamba (2016) also found that decreasing stellar effective temperature and mass yield decrease shear and differential rotation. Quenching of the diffusive strength of the dynamo may result in star-spots decaying slower on cool, early M stars than they do on hotter FGK stars with equivalent rotation periods (Giles, Collier Cameron & Haywood 2017). Star-spot lifetimes on early M dwarfs derived from observation have not yet been well documented, thus restricting their discussion relative to star-spot lifetimes on other solar-type stars. Giles et al. (2017) estimated star-spot lifetimes for approximately 2200 Kepler stars divided into two sample groups with stellar rotation periods of 10 and 20 d. Though the number of M dwarfs in the samples was limited, they projected star-spot lifetimes of roughly 50–275 d for the faster rotators and roughly 10–450 d for the slower rotators. A comparison may be made between the star-spot lifetime of 100–300 d for G-type stars estimated by Mehrabi, He & Khosroshahi (2017) and the observed star-spot lifetimes on the mid-type dwarf GJ 1243 (M4V) (Davenport, Hebb & Hawley 2015). From photometric analysis, Davenport et al. (2015) report a long-lived star-spot (on the order of years) and multiple appearances of a spot lasting 100–500 d. This may be indicative of slower star-spot decay for M dwarfs.

Due to the difficulty of observation, much remains to be learned about the morphology of star-spots and faculae on low luminosity, slowly rotating M dwarfs. Examination of star-spot and facula sizes, distributions, and temperatures on those stars will provide valuable information on the effect of stellar mass and effective temperature on the dynamo and a basis for comparison with the dynamic processes in solar-type stars. We propose that transit photometry mapping is an effective means of determining stellar rotation and differential rotation for early M dwarfs. The light curve of an exoplanet transiting an active stellar surface has small, in-transit variations due to the crossing of star-spots and faculae. The width, height, and time of these variations may be converted into the physical characteristics of star-spots and faculae, i.e. radius, intensity, and longitudinal position (Silva 2003). Via transit photometry mapping, the characteristics of individual star-spots and faculae cumulatively build magnetic activity maps of the stellar surface. This technique (see Section 3) has been used to evaluate stellar activity and rotation at transit latitudes for solar-type stars CoRoT-2 (G7V) (Silva-Valio et al. 2010; Silva-Valio & Lanza 2011), Kepler-17 (G2V) (Valio et al. 2017), Kepler-63 (G5V) (Estrela & Valio 2016), and Kepler-71 (G7V) (Zaleski et al. 2019).

We have analysed the photometry of the red dwarf Kepler-45 and present the first compilation of individual star-spot and facula physical parameters for an early M dwarf. The observations are described in Section 2, and the model is explained in Section 3. The results are shown in Section 4, beginning with the modelled characteristics of the spots and faculae in Section 4.1. Photosphere to star-spot and facula temperature contrasts and magnetic activity cycle are presented in Sections 4.2 and 4.4. Mean stellar rotation period and rotational velocity are discussed in Section 4.5. We further provide an estimate of stellar rotation period and differential rotation at the transit latitude from the mapping of star-spot and facula longitudes along the transit chord, which is typically non-

Table 1. Kepler-45 system parameters.

Parameter	Value	Ref
Star		
Spectral type	M1V	1
Kepler magnitude (K_p)	15.979	2
Mass ($M_\odot$)	0.59 ± 0.06	1
Radius ($R_\odot$)	0.624 ± 0.019	3
Effective Temp (K)	3820 ± 90	1
Rotation Period (d)	15.762 ± 0.016	4
Rotational Velocity (km s^{-1})	$2.009^{+0.019}_{-0.07}$	4
Age (Gyr)	0.5	1
Limb darkening coeff 1, c_2	$1.45^{+0.04}_{-0.03}$	4
Limb darkening coeff 2, c_3	$-1.349^{+0.013}_{-0.012}$	4
Limb darkening coeff 3, c_4	$0.776^{+0.009}_{-0.010}$	4
Planet		
Mass ($M_{\rm Jup}$)	0.505 ± 0.090	1
Radius ($R_{\rm Jup}$)	$1.133^{+0.012}_{-0.011}$	4
Radius ($R_{\rm star}$)	$0.1823^{+0.0020}_{-0.0018}$	4
Semimajor axis (au)	$0.0314^{+0.0009}_{-0.0008}$	4
Semimajor axis ($R_{\rm star}$)	$10.82^{+0.32}_{-0.28}$	4
Inclination angle (°)	$87.10^{+0.32}_{-0.20}$	4
Orbital period (d)	2.455239 ± 0.000004	1
Eccentricity	$0.11^{+0.10}_{-0.09}$	1

Note. 1: Johnson et al. (2012), 2: Brown et al. (2011), 3: Berger et al. (2018), 4: Fit by authors in this work

equatorial, in Section 4.6. A summary and discussion of our results relative to the solar standard is given in Section 5.

2 KEPLER-45

Kepler-45 is an M1 dwarf star introduced by Borucki (2011) as Kepler Object of Interest KOI-254 (Kepler ID# 5794240) and studied by Johnson et al. (2012). Kepler-45 is a dim, cool dwarf with Kepler-band magnitude = 15.979 and $T_{\rm eff}$ = 3820 K. Its mass and radius are approximately 60 per cent of those of the Sun. Johnson et al. (2012) estimated a stellar rotation period of 15.8 ± 0.2 d and age of 0.5 Gyr, derived using the rotation period and gyrochronology relations published by Barnes (2010). A full set of system parameters is given in Table 1.

Kepler-45 is transited by a single hot Jupiter, Kepler-45b, with mass 0.505 $M_{\rm J}$ and radius 1.133 $R_{\rm J}$, in a 2.455 d orbit (refer to Table 1). Kepler-45b orbits its host star at a distance of 0.03 au, making it an excellent target for future study of the atmosphere of a planet receiving energy emitted from a cool host star (Shields, Ballard & Johnson 2017). A planet the size of Kepler-45b crossing a star whose radius is 60 per cent of the Sun's results in a transit depth up to 150 times greater than that due to an Earth-sized planet transiting the same sized star. The mean transit depth of Kepler-45b smoothed light curves is 3.52 per cent of normalized flux, with a maximum depth of 3.99 per cent. This significant transit depth increases the probability of extracting star-spots and faculae from noise in the transit light curve since these magnetic features generally cause less than a 0.5 per cent variation in stellar flux.

Kepler-45b transit light curves are contained in the NASA Exoplanet Archive at MAST, which is a repository of raw and pre-conditioned light curve data spanning the almost 4 yr of the *Kepler* mission (Thompson et al. 2016). The available pre-conditioned data, or Pre-search Data Conditioning Simple Aperture Photometry (PDCSAP), has been cleansed of systematic noise due to *Kepler*

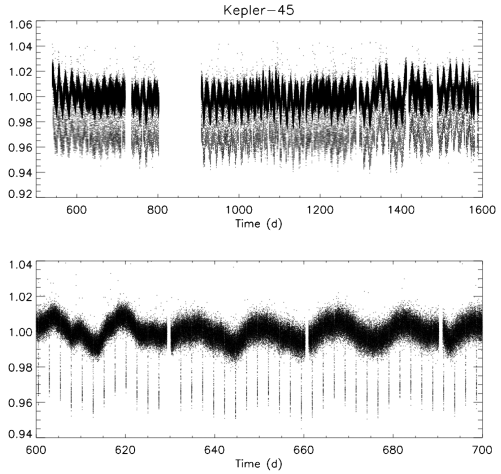

Figure 1. *Top:* Kepler-45 SC light curves for Quarters 6–8 and 10–17. Time in days corresponds to Barycentric Kepler Julian Date (BKJD). Observation began on 539.4608 BKJD and ended on 1591.0013 BKJD (2010 June 24–2013 May 11). *Bottom:* Enlargement of 100 early days of observation of Kepler-45.

telescope instrumentation (Jenkins et al. 2010; Smith et al. 2012; Stumpe et al. 2012). Data were recorded at the two sampling rates of the *Kepler* spacecraft, a long cadence (LC) mode of 29.4 min and a high temporal precision short cadence (SC) mode of 58.85 s. The PDCSAP SC data provide the temporal resolution required for the assessment of star-spots and faculae, whose presence lasts only minutes during a transit.

Johnson et al. (2012) used LC data from *Kepler* quarters 1 and 2, with supporting radial velocity measurements, adaptive optics imaging, and NIR spectroscopy to confirm the parameters of the Kepler-45 system. The unavailability of SC data for those early quarters precluded a detailed study of stellar magnetic activity. Thus, we augment the earlier work of Johnson et al. (2012) with our analysis of Kepler-45's photospheric activity and an estimate of stellar differential rotation at our computed transit latitude of −33.2°. Of interest to our investigation are the detrended PDCSAP SC light curves. Our analyses utilized the SC data in Kepler Data Release 25 (Thompson et al. 2016) available for 11 quarters: 6 through 8, beginning 2010 June 24 and ending 2011 March 24, and 10 through 17, beginning 2011 June 28 and ending 2013 May 11. The SC light curves for those quarters, as shown in Fig. 1, constitute observation for approximately 1000 d and contain 351 recorded transits out of 428 possible transits from the beginning of Quarter 6 to the end of Quarter 17. The depth of the transits and stellar rotation are evident.

2.1 Kepler-45b light curves

Kepler-45b probes the surface of its host star in a well-aligned, low obliquity orbit (Dai et al. 2018). The planet crosses its host star at stellar latitude $-33.2^\circ\ ^{+1.0}_{-0.9}$ (refer to Table 2 in the following section). The in-transit portion of each SC light curve is examined for potential star-spots and faculae, i.e. bumps and dips, along the transit chord. Figs 2 and 4 demonstrate the modulation in transit light curves due to the passage of the planet over star-spots and faculae. The normalized transit depth in both examples is 3.65 per cent, and

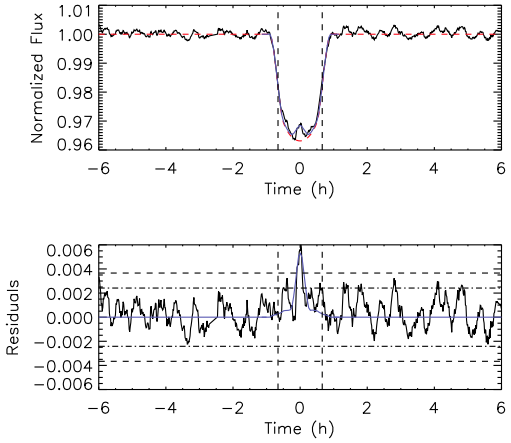

Figure 2. *Top:* SC light curve for Transit 97. The solid black line represents the observed data after 10 point smoothing. A potential star-spot is centred about $t = 0$, corresponding to 801.819 BKJD. The red dashed curve corresponds to the model of a spotless star, whereas the blue one is the result of the one spot fitting. The dashed vertical lines are $\pm 70^\circ$ from the centre of the stellar disc at $t = 0$. *Bottom:* Residuals resulting from the subtraction of the unspotted model from the smoothed transit data are shown by the solid black line. Star-spot residuals greatly exceed the rms noise, where the horizontal lines are ± 100 per cent (dashed) and ± 67 per cent (dash–dotted) of the unsmoothed out-of-transit rms noise, respectively. The blue line highlights the fit to the modelled spot.

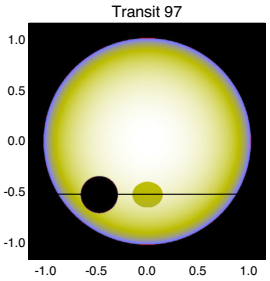

Figure 3. Image of the modelled star during Transit 97 with a single, big spot near the star's central meridian shown in grey. This spot is the result of the fit represented by the blue curves of Fig. 2. The planet is pictured as a black circle, with the horizontal line marking its transit path at -33.2°.

the transit duration is 1.820 ± 0.004 h. The example in Fig. 2 for Transit 97 shows a large star-spot centred at mid-transit ($t = 0$), pictured in Fig. 3. The time at mid-transit corresponds to 801.819 BKJD (Barycentric Kepler Julian Date defined as Barycentric Julian Day (BJD) minus an offset of 2454833 corresponding to 12:00 on 2009 January 1 UTC). In the upper panel of Figs 2 and 4, the irregular black curve represents observed data, which has been normalized and smoothed every 10 points. The smooth, U-shaped red dashed curve is the transit model for a spotless stellar surface as generated from system parameters. This model is detailed in Section 3. The blue curve is the result from one spot fitting, whose result is depicted in Fig. 3. The residuals resulting from the subtraction of the unspotted model from the smoothed data are shown in the lower panel in black and accentuate the star-spot's presence. The

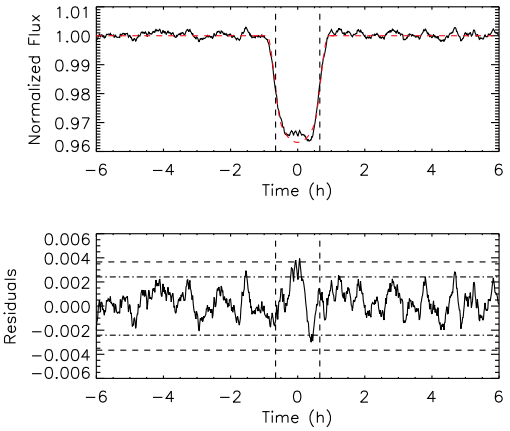

Figure 4. *Top:* SC light curve for Transit 5. The plotted quantities are the same as those defined for Fig. 2. The transit centre ($t = 0$) corresponds to 551.384 BKJD. *Bottom:* The residuals of potential star-spots near $t = 0$ exceed 100 per cent of the unsmoothed out-of-transit rms noise (dashed line). One potential facula near $t = 0.5$ h exceeds 67 per cent of the unsmoothed out-of-transit rms noise (dash–dotted line).

amplitude of its modulation is approximately 0.6 per cent. The model residual, depicted by the blue curve in the lower panel of Fig. 2, visualize our ability to replicate star-spot characteristics.

A spot group and a facula are evident in the Transit 5 light curve shown in Fig. 4. The star-spots appear near mid-transit, or 551.384 BKJD, with an amplitude of roughly 0.4 per cent, while the facula is apparent closer to the stellar limb with a dip of smaller amplitude of approximately 0.3 per cent.

3 THE MODEL

We have applied the model developed by Silva (2003), which simulates the passage of an exoplanet across a stellar disc. The stellar surface is defined as a 2D white light pixelated image. A three parameter limb darkening law is applied to the image (Sing et al. 2009) as given by

$$\frac{I(\mu)}{I(1)} = 1 - c_2(1-\mu) - c_3(1-\mu)^{3/2} - c_4(1-\mu)^2, \quad (1)$$

where $I(1)$ is the maximum intensity at disc centre, c_2, c_3, and c_4 are the limb darkening coefficients, and $\mu = \cos(\theta)$, where θ is the angle between the line of sight and the emergent intensity.

The planet is represented as a dark, opaque disc, with radius defined in units of stellar radius (depicted as the black circle in Fig. 3). Using the semimajor axis, period, and inclination angle of the planet's orbit (black horizontal line in Fig. 3), the planet's orbital position is calculated in 2 min increments from $t = -2$ h to $t = 2$ h, where $t = 0$ corresponds to mid-transit. At each time interval, the stellar intensity is calculated as the sum of all pixels in the stellar image. This produces a smooth transit light curve as a function of time (red dashed curves of Figs 2 and 4).

In light of the small eccentricity and low obliquity of the Kepler-45 system, we set two initial conditions for simulating the planet's orbit:

(i) The planet's orbit is circular (null eccentricity);
(ii) The planet's orbit is coplanar with the stellar equator (null obliquity).

Table 2. Secondary transit parameters of the Kepler-45 system.

Parameter	Value
Transit latitude (°)	$-33.2\ ^{+1.0}_{-0.9}$
Impact parameter	$0.548\ ^{+0.016}_{-0.014}$
Transit duration (h)	1.820 ± 0.004

With these conditions, the values for planet radius, semimajor axis, and inclination angle published by Johnson et al. (2012) were used to generate a preliminary model light curve. The model was then fit to an average of normalized and phase folded transits for all 11 *Kepler* quarters using an interactive data language (IDL) implementation of the Goodman & Weare (2010) Monte Carlo Markov Chain (MCMC) ensemble sampler to obtain the most probable parameter values and their uncertainties. The limb darkening coefficients were additionally fit in accordance with Kipping (2016)'s implementation of the three parameter limb darkening law (equation 1), which is based on analytic criteria for limiting combinations of coefficients to those that are physically plausible. The optimized parameters and coefficients are included in Table 1. Each value represents the median (50 per cent) of its sampling, with lower and upper 1σ errors corresponding to the 16 per cent and 84 per cent quantiles (Hogg & Foreman-Mackey 2018). We revised the values for planet radius, semimajor axis, and orbital inclination angle published by Johnson et al. (2012). The mean planet radius increased approximately 18 per cent from the value of 0.96 from Johnson et al. (2012) to 1.13 $R_{\rm Jup}$. The mean planet to stellar radius ratio increased 1.7 per cent from 0.179 to 0.182, and the scaled semimajor axis also increased 2.12 per cent from 10.6 to 10.82 stellar radii. The estimated mean stellar radius of 0.624 $R_\odot$ from Gaia Data Release 2 (DR2) was used for parameter scaling (Berger et al. 2018). The value from *Gaia* is approximately 13.5 per cent larger than the value of 0.55 $R_\odot$ first published by Johnson et al. (2012). The two values agree, however, within 1σ uncertainty. We also found that our estimate of $87.10^\circ\ ^{+0.32}_{-0.20}$ for orbital inclination angle agrees well with the value of $87.0^\circ \pm 0.7$ given by Johnson et al. (2012).

Impact parameter, transit latitude, and transit duration were computed from the fitted parameters and are given in Table 2. Impact parameter and transit latitude depend on inclination angle and semimajor axis as given by

$$b = \frac{a\cos(i)}{R_{\rm star}} \tag{2}$$

$$lat_{\rm tran} = \arcsin\left[\frac{a}{R_{\rm star}\cos(i)}\right], \tag{3}$$

where a is the semimajor axis, $R_{\rm star}$ is the stellar radius, and i is the inclination of the planet's orbit. The choice for transit projection to be in the Southern hemisphere is arbitrary (see Fig. 3). Transit duration is the difference between the times of ingress and egress in the model.

The smooth dashed red curves shown in the upper panels of Figs 2 and 4 represent the optimized model of a star without spots or faculae on its surface. The solid, irregular black curve represents the observed data after 10 point smoothing. When the model is subtracted from smoothed data, the residuals in the lower panels are obtained. The acceptance criteria which magnetic features must meet in order to be discerned from noise are represented by the horizontal lines in the lower panels, the double dot–dashed and dashed lines marking 67 per cent and 100 per cent of the out-of-transit rms, respectively. The rms noise for smoothed and unsmoothed data, both in and out-of-transit, is given in Table 3.

Table 3. RMS noise of Kepler-45 SC data.

Data	RMS
Unsmoothed	
In-transit	0.00379
Out-of-transit	0.00366
Smoothed	
In-transit	0.00145
Out-of-transit	0.00125

For both smoothed and unsmoothed data, the rms of the in-transit portion of all light curves is greater than the rms out-of-transit, inferring the existence of star-spots and faculae with amplitudes exceeding the noise. As may be noted from Figs 2 and 4, the out-of-transit residuals exceed rms values for smoothed data. Thus, we adopted the out-of-transit light-curve rms as a benchmark for evaluating potential star-spots and faculae in the residuals. Star-spot and facula residuals must either exceed ± 100 per cent of the unsmoothed out-of-transit rms, or meet or pass ± 67 per cent of the unsmoothed out-of-transit rms when transit noise is contained within ± 67 per cent of the rms.

To determine the physical characteristics of magnetic features in a specific transit, those features are added to the surface of the modelled star to synthesize a spotted star transit model. A maximum of four features, either star-spots, faculae, or a combination of both, may be added as needed to fit an observed transit. While the number of features is variable, we found that a maximum of four features was enough to match the variations in observed transits. Star-spots and faculae are represented as dark and bright discs, respectively, and defined by radius, intensity, and longitude. Their latitude defaults to the transit projected latitude. The spotted model is fit to the observed transit light curve using an MCMC algorithm to determine probable values for these three physical characteristics for each spot. Intensity is defined relative to the stellar central intensity, $I(1) = 1$. Star-spot intensity must be less than $I(1)$ and greater than 0, and facula intensity must be greater than 1 but limited to 2. Mid-range values for intensity, 0.5 $I(1)$ for star-spots and 1.5 $I(1)$ for faculae, are inputs to the MCMC fit. Planet radius, $R_{\rm P}$, is defined in units of stellar radius, with an initial guess value of 0.5 $R_{\rm P}$. Longitude is defined with respect to 0° stellar topocentric longitude, which corresponds to the middle of the planet's projection on to the stellar disc at $t = 0$. Longitude is constrained to $\pm 70^\circ$ to avoid steep variations in intensity near the stellar limbs (Silva-Valio et al. 2010). The starting longitude for the fit is determined from the transit time at the centre of each star-spot or facula signature by

$$lon_{\rm sf} = \arcsin\left[\frac{a\cos\left(90^\circ - \frac{360^\circ\ t_{\rm sf}}{24\ P_{\rm orb}}\right)}{\cos(lat_{\rm tran})}\right], \tag{4}$$

where a is the semimajor axis, $P_{\rm orb}$ is the orbital period, $lat_{\rm tran}$ is the transit latitude, and $t_{\rm sf}$ is the time at star-spot or facula centre signature.

4 RESULTS

4.1 Star-spot and facula characteristics

The depth of Kepler-45b transits is variable, inferring photospheric activity. Does the M dwarf Kepler-45 indeed display the activity expected on cool stars with solar-type internal structure (Berdyugina 2004; Balona & Obedigamba 2016)? The presence of star-spots

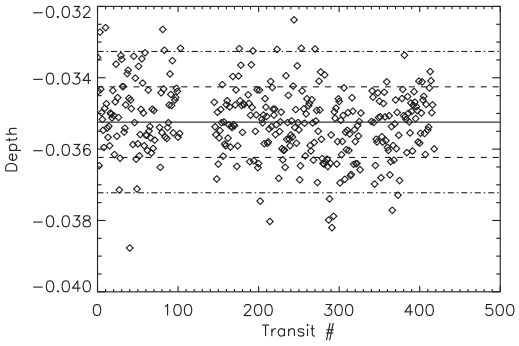

Figure 5. Change in transit depth as a function of transit number. All values are the difference relative to normalized flux (= 1). The solid line is the mean transit depth. The dashed and dash–dotted lines denote $\pm 1\sigma$ and $\pm 2\sigma$, respectively. Approximately 95 per cent of the transit depths are within $\pm 2\sigma$ of the mean.

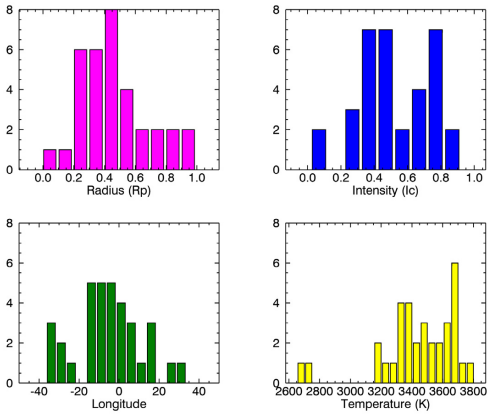

Figure 6. Histograms of star-spot parameters: radius and intensity (top row), and longitude in the observer's reference frame and temperature (bottom row).

will decrease the observed stellar flux, while faculae will add to the irradiance. Transit photometry mapping requires that the probing planet cross star-spots and/or faculae at the projected transit latitude. The depth variations observed for Kepler-45b at transit latitude -33.2° indicate such crossings.

The mean depth of Kepler-45b transits is 3.52 ± 0.10 per cent of normalized flux (= 1). Fig. 5 pictures the change in transit depth with transit number. A dispersion of estimated depths is anticipated since observed transit data have been smoothed every 10 points to preserve magnetic features and/or the irradiance of the observed stellar surface can vary with rotation. Close to 95 per cent of transit well depths fall within $\pm 2\sigma$ of the mean. The minimum and maximum transit depths are 3.238 per cent and 3.877 per cent, respectively. Transits are examined individually to determine (1) if the estimated depths are caused by noise or discontinuities, (2) if there are incomplete transits to eliminate, or (3) if magnetic signatures appear in complete and unbroken transits of any depth. Each continuous and complete transit is plotted against an unspotted model (red dashed curves of Figs 2 and 4) generated using the optimized orbital and

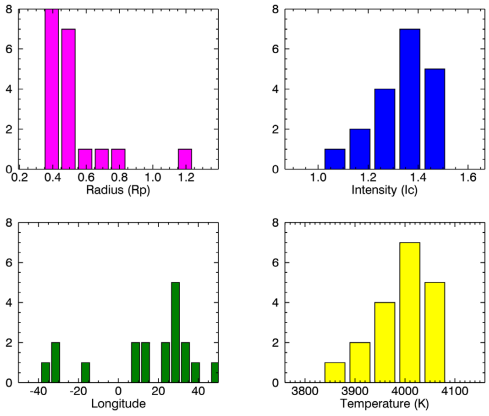

Figure 7. Histograms of facula parameters: radius and intensity (top row), and longitude in the observer's reference frame and temperature (bottom row).

stellar parameters. For those transits showing possible activity, the residuals resulting from the subtraction of the model from observed data are evaluated against the rms criteria given in Section 3. Star-spots and/or faculae in positively assessed transits are added to the spotless model and fit to the observed data on a per transit basis (see the preceding section, especially Figs 2, 3, and 4).

Star-spots and/or faculae were identified in 40 transits using the rms criteria and fit using MCMC. In total, 34 star-spots were found in 22 transits, and 19 faculae were detected in 18 transits. All but one facula appear as a single feature. Large star-spots suggesting spot groups were divided into multiple spots whenever possible. 14 of the star-spots fit were singletons, with the remaining star-spots divided among 6 pairs of spots, 2 sets of 3 spots, and 1 set of 2 spots with 1 facula.

Histograms of radius, intensity, and longitude are shown in Fig. 6 for star-spots and Fig. 7 for faculae. Star-spot mean radius is $0.51 \pm 0.22\ R_{\rm p}$, or equivalently $(40 \pm 17) \times 10^3$ km. The minimum and maximum star-spot radii are 0.04 and 0.98 $R_{\rm p}$, or 3×10^3 and 78×10^3 km. Faculae are approximately 10 per cent larger than the star-spots, with a mean radius of $0.57 \pm 0.20\ R_{\rm p}$, or $(45 \pm 16) \times 10^3$ km. The smallest facula has a radius of 0.39 $R_{\rm p}$, or 31×10^3 km, and the largest has a radius of 1.23 $R_{\rm p}$, or 98×10^3 km.

Mean star-spot intensity is 0.57 ± 0.22 I(1), and mean facula intensity is 1.37 ± 0.12 I(1), where $I(1)$ is the central intensity of the photosphere ($\mu = 1$). The intensities of star-spots are within the range of 0.07–0.96 $I(1)$. Facula intensities are within 1.07 and 1.49 $I(1)$. The intensity equivalent temperatures are discussed in Section 4.2.

Star-spot observation is generally greater in the central area of the stellar disc, while facula are perceived more commonly towards the stellar limbs. Star-spots are seen at longitudes spanning -34° to $+33^{\circ}$ along the transit chord in the reference frame of an observer on Earth, where 0° longitude is the central meridian of Kepler-45 at mid-transit. Faculae are discerned at longitudes -37° to $+49^{\circ}$. As may be noted in the longitude histograms, the majority of star-spots are observed within $\pm 20^{\circ}$ of the central meridian. Conversely, most faculae have longitudes $<-20^{\circ}$ or $>20^{\circ}$. This behaviour replicates that of their solar counterparts, where solar faculae are best observed close to the limb.

4.2 Star-spot and facula temperatures

Star-spot temperatures are one element in the understanding of convective flow suppression due to magnetic fields in active regions (Biazzo et al. 2006). From a compilation of star-spot contrasts, i.e. the temperature difference between star-spots and the photosphere, versus photosphere temperature for active stars, Berdyugina (2005) noted that contrast between star-spots and the photosphere decreases with decreasing stellar effective temperature. For example, star-spot contrast was approximately 500 K for a photosphere temperature of 3800 K and decreased to 200 K for a photosphere temperature of 3300 K. A later study of star-spot contrasts for dwarf stars by Mancini et al. (2017) contradicts this trend. They found no obvious dependence between contrast and effective temperature, or spectral class. Example dwarf stars of spectral types M2 and M4 had contrasts up to 850 K, comparable to the roughly 850 K contrast of the Sun, while hotter M dwarfs did not exceed contrasts of 600 K.

Much of what is known about star-spot physical properties on M dwarfs has come from TiO band spectroscopy (Fang et al. 2016). The transit method has provided a newer technique for determining physical properties. Of particular interest is the conversion of derived star-spot photometric intensity to temperature. Under the assumption that star-spots and the unspotted photosphere radiate as theoretical blackbodies, Planck's Radiation Law can be used to solve for star-spot temperature (Silva 2003). The ratio between star-spot and photosphere intensities is given by

$$\frac{I_{\rm spot}}{I_{\rm phot}} = \frac{\exp\left(\frac{hc}{\lambda K_{\rm B} T_{\rm eff}}\right) - 1}{\exp\left(\frac{hc}{\lambda K_{\rm B} T_{\rm spot}}\right) - 1}, \tag{5}$$

where h is Planck's constant, c is the speed of light, λ is the Kepler-band observation wavelength, $K_{\rm B}$ is Boltzmann's constant, and $T_{\rm eff}$ and $T_{\rm spot}$ are the photosphere and spot temperatures, respectively. The *Kepler* telescope's broad bandpass ranges from 420 to 900 nm, with optimal response at 600 nm.

Solving the above equation for $T_{\rm eff} = 3820$ K and $\lambda = 600$ nm yields a mean star-spot temperature of 3470 ± 250 K. As shown in the lower, right hand panel of Fig. 6, all but two star-spot temperatures lie within 3150–3800 K. The temperature contrast between the unspotted photosphere and the star-spots is $350\ ^{+260}_{-110}$ K. Berdyugina (2005) attributed low contrast in M dwarfs to either a larger contribution from the star-spot penumbra than from the umbra or small star-spot sizes. While we can estimate star-spot radii, the observed data do not permit delineation of umbral regions.

The mean temperature of the 19 modelled faculae calculated via equation (5) is 4020 ± 60 K, whereas the photospheric contrast is 200 ± 150 K. Solar faculae exhibit a similar contrast, differing from the quiet photosphere by a few hundred Kelvin (Solov'ev et al. 2019).

The star-spot to photosphere temperature ratio, $T_{\rm spot}/T_{\rm phot}$, falls in the range 0.68–0.97. These values are high compared to the ratio of 0.70 ± 0.05 for active G and K stars derived by O'Neal et al. (2004, 2006) from TiO band modelling. This may indeed infer a relatively moderate activity level for Kepler-45 as seen by the small number of star-spots at the transit latitude. From a study of all *Kepler* M dwarfs, Hawley et al. (2014) found that inactive early M dwarfs are less spotted than active mid M dwarfs.

4.3 Spot area coverage

While Kepler-45's photometric variability amplitude is significant, it cannot be used to predict the spot coverage of the entire stellar surface (Apai et al. 2018). The area covered by spots in time within the transit band of Kepler-45 is plotted in Fig. 8. Kepler-45 has a mean spotted area of 4.1 ± 2.5 per cent of the stellar surface (dashed horizontal line), which may contribute to the 3 per cent light-curve variability. The star-spots on Kepler-17, an active G2 star, are slightly larger than those on Kepler-45 (mean radius $(49 \pm 10) \times 10^3$ km) and cover an average area of 6 ± 4 per cent within the transit band 0° to -10° (Valio et al. 2017). Thus, the activity level of Kepler-45 is less than that of active G stars but greater than that of the current Sun.

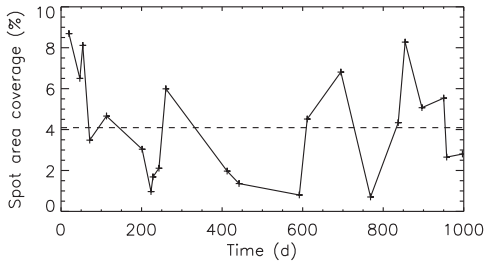

Figure 8. Area covered by spots within the occulted transit band of the surface of Kepler-45 for the whole observing period.

Doppler images of active early M dwarfs have shown that star-spots are distributed across the stellar surface, with no indication of dominant polar spots (Barnes et al. 2017 and references therein). In a Zeeman Doppler Imaging study of five slowly rotating, moderately active early M dwarfs (M0–M2), Hébrard et al. (2016) found that dark spots concentrate either close to the stellar magnetic pole or magnetic equator. Spots on the M0 dwarf GJ 410, whose physical properties of mass, radius, and rotation period are similar to those of Kepler-45, were found to concentrate towards the magnetic equator. The large-scale magnetic fields of GJ 410 and Kepler-45 may act similarly to the Sun's magnetic field, dictating the emergence of spots at solar latitudes.

4.4 Activity cycle

The strong magnetic fields of early M dwarfs may result in flaring rather than in organized spot emergence and cycles (Bondar 1995; Hathaway 2015). Yet, high-resolution spectra containing the Hα and/or Ca II K chromospheric indicators in conjunction with photometric data have been used to measure early M dwarf long-term activity cycles (Gomes da Silva et al. 2011; Astudillo-Defru et al. 2017; Küker et al. 2019). Long-term activity cycles are generally less than 8 yr (Küker et al. 2019). Bucconi et al. (2011) reported an activity cycle of approximately 4 yr for the M1 flare dwarf GI 229 A and approximately 7 yr for the M2.5 star GI 752 A. There remains no obvious correlation between rotation rate and cycle length (Savanov 2012; Küker et al. 2019).

Long-term activity cycles have been well studied for non-Kepler stars including M dwarfs (Oláh et al. 2009; Gomes da Silva et al. 2012; Savanov 2012; Robertson et al. 2013). Little appears in the literature concerning short-term cycles. While the observation span of the *Kepler* mission is insufficient for long-term cycle study, it does allow for examination of short-term cycles. Short-term cycles provide further evidence of the nature of the dynamo operating in early M dwarfs. Short-term cycles are known to exist in the Sun (Hathaway 2015). If early M dwarfs are truly solar-type stars, they should exhibit similar short-term cycles driven by an $\alpha\Omega$ dynamo.

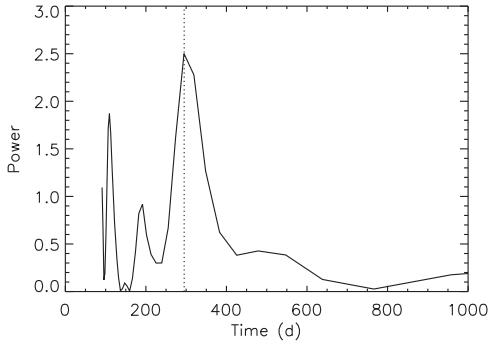

Figure 9. Activity cycle from Lomb–Scargle analysis of the total flux deficit due to star-spots per transit. The vertical dotted line intersects the curve at the peak power corresponding to a short activity cycle of 295 d.

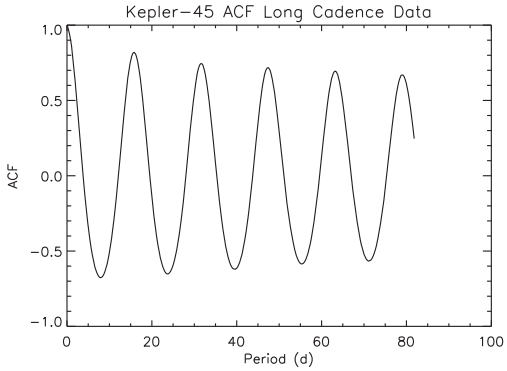

Figure 10. ACF of transit cleansed LC data for all quarters. The series of peaks corresponds to a mean stellar rotation period of 15.762 d.

Short-term cycles have been previously calculated from *Kepler* photometry (Vida, Oláh & Szabó 2014; Estrela & Valio 2016).

We see no evidence of flares in Kepler-45 light curves but do observe temporal recurrence of star-spots along the transit chord indicating possible cyclic behaviour. Short-term activity cycles may be derived from the temporal variation of the number of star-spots or the correlation of the total flux deficit per transit due to star-spots (Estrela & Valio 2017). Due to the sparsity of star-spots, we chose to employ the deficit method. Spot deficit is defined as effective spot area times surface intensity difference, or the central stellar intensity (= 1) minus spot intensity. The total flux deficit per transit is given by

$$F_{\rm def} = \sum r_{\rm spot}^2 (1 - I_{\rm spot}), \tag{6}$$

where $F_{\rm def}$ is the total flux deficit per transit due to spots, $r_{\rm spot}$ is spot radius, and $I_{\rm spot}$ is spot intensity.

Lomb–Scargle analysis of the total flux deficit per Kepler-45b transit yields a short magnetic activity cycle of 295 ± 50 d as shown by the dominant peak in Fig. 9. In comparison, the K4 dwarf HAT-P-11 (Kepler-3) has an activity cycle of 305 ± 60 d, derived from the flux deficit method (Estrela & Valio 2017), and the Sun has a short-term variability of roughly 154 d and quasi-biennial oscillation of 0.6–4 yr, deduced from daily sunspot numbers and sunspot areas (Zaqarashvili et al. 2010; Balogh et al. 2014; Hathaway 2015).

4.5 Mean stellar rotation period and rotational velocity

We verified the estimate of mean stellar rotation period for Kepler-45 published by Johnson et al. (2012), who used LC data from *Kepler* Quarters 1 and 2, and the later refined value of 15.816 ± 0.021 d published by McQuillan, Aigrain & Mazeh (2013), who used LC data from *Kepler* Quarters 1–4. The autocorrelation technique described in McQuillan, Mazeh & Aigrain (2014) was applied to all LC data for full Quarters 1 to 16 to recalculate the rotation period. The LC data were cleansed of transits and regridded to one continuous data set before performing the autocorrelation. The results are shown in Fig. 10. The slope of a line through the first four peaks yields a mean stellar rotation of 15.762 ± 0.016 d.

Using our estimate of mean stellar rotation period and the mean stellar radius of 0.624 $R_\odot$ from *Gaia* DR2, we calculate $v \sin i = 2^{+0.019}_{-0.070}$ km s^{-1}. Such low rotational velocities for early M dwarfs have been reported by Jeffers et al. (2018). They find that slow rotators of spectral type < M3.5V have $v \sin i < 5$ km s^{-1} and are Hα inactive.

4.6 Transit latitude rotation period and differential rotation

The model of a differentially rotating Sun, with rotation decreasing from the equator towards the poles, is the benchmark against which the latitudinal rotation of other stars is measured. If Kepler-45 rotates differentially, observed star-spots and faculae at latitudes less than 45° will move across the stellar face with a period less than the mean stellar rotation period. Thus, to evaluate the differential rotation of Kepler-45, first an estimate of the rotation at the transit latitude is needed. This was done using all the 53 features observed on the surface of Kepler-45.

Star-spot and facula longitudes are converted from the frame of an observer on Earth to the rotating frame of the star. The re-referenced longitudes are used to build a temporal map of the stellar surface at the mean stellar rotation period. The rotation period is then varied to find the one which best aligns the magnetic features with respect to longitude. The method is the same used previously for CoRoT-2 (Silva-Valio & Lanza 2011), Kepler-17 (Valio et al. 2017), and Kepler-71 (Zaleski et al. 2019).

The rotation period at the transit latitude of −33.2° that best aligns the magnetic features (star-spots and faculae) was found to be 15.520 ± 0.028 d. The reconstructed map of the stellar surface at that latitude, as a function of time, is shown in Fig. 11. Star-spot and facula concentrations are greatest at −110° and +10° as seen in the lower panel of Fig. 11. These concentrations may be indicative of active longitudes. The existence of active longitudes is anticipated on more active or rapidly rotating M dwarfs, paralleling the trend for young, solar-type stars (Lehtinen et al. 2016). Vida et al. (2010) located active regions separated by 120° on the M1-2 dwarf EY Dra ($v \sin i = 61$ km s^{-1}) (Jeffries, James & Bromage 1994).

Once the rotation period at the transit latitude has been determined, the differential rotation of the star can be estimated by assuming a differential rotation profile similar to the Sun's. In this case, we consider

$$\Omega(\alpha) = \Omega_{\rm eq} - \Delta\Omega \sin^2(\alpha), \tag{7}$$

where Ω is the angular velocity at a certain latitude, α, and $\Omega_{\rm eq}$ is the angular velocity at the stellar equator. $\Delta\Omega$ is the difference between the angular velocities at the equator and the pole, also known as rotational shear.

Assuming that the star-spots and faculae are present from the equator to the poles of the star, the resulting average rotation, $\bar{\Omega}$ is computed by integrating equation (7) from 0° to 90°. Thus the

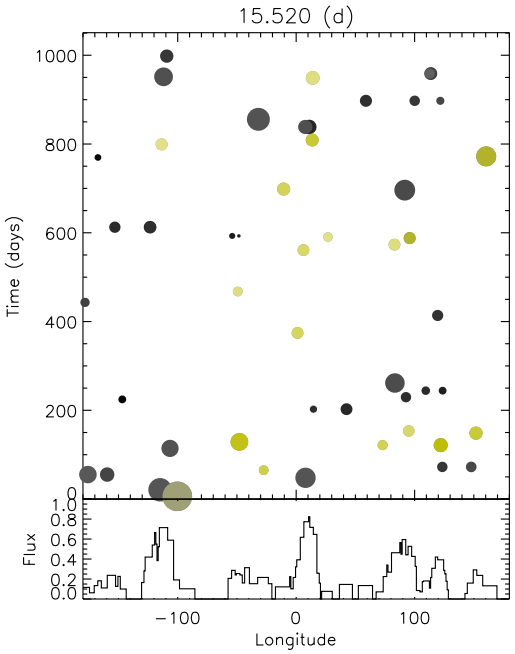

Figure 11. *Top:* Temporal map of the stellar surface at the transit latitude considering a period of 15.520 d. Star-spots are shown in shades of grey whereas faculae are shown in yellow. *Bottom:* The total flux difference from star-spots and faculae versus longitude.

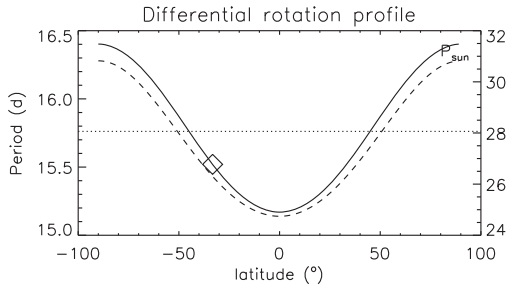

Figure 12. Differential rotation profiles of Kepler-45 (solid line) and the Sun (dashed line) as a function of latitude. The diamond marks the 15.520 d rotation period of Kepler-45 at transit latitude −33.2° estimated from transit mapping. The horizontal dotted line signifies the mean stellar rotation period of 15.762 d.

equation for the average angular rotation simplifies to

$$\bar{\Omega} = \Omega_{\rm eq} - \Delta\Omega/2. \quad (8)$$

The differential rotation profile of Kepler-45 is plotted in Fig. 12 as a function of latitude. The differential rotation profile of the Sun is included for comparison. The horizontal line indicates the 15.762 d mean stellar rotation period, and the diamond signifies the 15.520 d rotation period of Kepler-45 at the transit latitude.

Considering $\bar{\Omega} = 2\pi/P_{\rm rot}$, where $P_{\rm rot} =$ 15.762 d is the average rotation period estimated in Section 2, we estimated $\Omega_{\rm eq} = 0.4142 \pm 0.0018 \pm$ rad d^{-1} , or $P_{\rm eq} = 15.17 \pm 0.07$ d, and $\Delta\Omega = 0.031 \pm 0.004$ rad d^{-1} , which yields a relative differential rotation of $\Delta\Omega/\bar{\Omega}$ of 7.8 ± 0.9 per cent. In a spectropolarimetric study of a small sample of M0–M3 dwarfs, Donati et al. (2008) detected rotational shears of 0.06–0.12 rad d^{-1} . They estimated that the M2.5 dwarf CE Boo, which is somewhat younger and smaller than Kepler-45 and has a rotation period of approximately 14 d, rotates differentially at a rate of no less than 0.03 rad d^{-1}. Reinhold, Reiners & Basri (2013) and later Reinhold & Gizon (2015) computed a relative shear between 0.01 and 0.11 rad d^{-1} for M dwarfs with $T_{\rm eff}$ between 3000 and 4000 K and a rotation period of approximately 15 d. Most recently, Küker et al. (2019) calculated that for early M dwarfs (0.66 M$_\odot$, $T_{\rm eff} = 4038$ K) shear increases from 0.028 to 0.047 rad d^{-1} as rotation period increases from 1 to 10 d and then decreases for longer periods due to reduction in the α dynamo effect. Their shear value for a rotation period of approximately 15 d is 0.045 rad d^{-1}.

5 SUMMARY AND DISCUSSION

This work presents the first robust analysis of stellar activity for a faint, early M dwarf from transit photometry. Kepler-45 is an M1V star with radius 0.624 R$_\odot$ and effective temperature of 3820 K. Given its low luminosity at Kepler magnitude 15.979 and moderately slow rotation period of 15.72 d, transit photometry becomes the best and only method for studying stellar activity. The hot Jupiter Kepler-45b is an optimal probe of its host star's surface as it passes between the star and the observer in a coplanar orbit. Kepler-45b (1.13 $R_{\rm Jup}$) orbits with a 2.45 d periodicity at a distance of 0.03 au. Photometric observation of Kepler-45 benefits from the radial size of Kepler-45b and its relatively short periodicity, yielding 351 deep transits in *Kepler* SC mode over the observation time of less than 4 yr. Only slightly more than 11 per cent of these recorded transits display discernible surface activity having flux variation greater than noise that may be attributed to star-spots and faculae.

We verified the mean rotation period through autocorrelation of transit-cleansed LC data (see Section 2). From our estimated rotation period and the mean stellar radius from *Gaia* DR2, we calculate a rotational velocity of 2 km s^{-1}. Early M dwarfs generally appear to have low rotational velocity (Kiraga & Stępień 2011). Reiners, Joshi & Goldman (2012) observed that early M dwarfs in a sample of spectral types M0–M4.5 rarely have a rotation velocity greater than 3 km s^{-1}. When considering a rotation–activity relation by which activity increases commensurate with increasing stellar rotation, we expect Kepler-45 to demonstrate relatively moderate activity as witnessed by the degree of spottedness (Messina et al. 2003; Kiraga & Stępień 2011). We found a modest amount of star-spots and faculae along transit latitude −33.2°, but unfortunately our method cannot project latitude dependent spottedness in light of the planet's orbital obliquity. Yet, the out-of-transit full-amplitude variability of approximately 3 per cent infers that star-spots appear at latitudes outside of the transit band. The source of Kepler-45's variability may be caused by small spots peppering the stellar surface beyond the transit band. Dark spots on early M dwarfs (M0–M2) were found to appear either close to the stellar magnetic pole or magnetic equator (Hébrard et al. 2016). They noted that spots on the M0 dwarf GJ 410, a star similar to Kepler-45, were concentrated towards the magnetic equator. This might imply that the spot area coverage for Kepler-45 is higher closer to the equator, assuming a solar-like spot distribution pattern. The spot area coverage is 4.1 ± 2.5 per cent at transit latitude −33.2°, thus at the upper limit in latitude where sunspots are detected.

The longitudes of star-spots and faculae detected on Kepler-45 follow the observational distribution of their solar counterparts. Sunspots are observed away from the solar limbs, while solar faculae are brighter and more visible towards the solar limbs. In the observer's reference frame, Kepler-45's star-spots are seen closer to the stellar disc centre than the faculae which are seen closer to the stellar limbs. Most star-spots have longitudes within $\pm 20^\circ$ of the centre of the stellar face (Fig. 6), while most faculae longitudes are $< -20^\circ$ or $> 20^\circ$ and as great as 49° (Fig. 7).

Spectroscopic analysis has largely been the knowledge source for star-spot temperature. The transit method is now stepping to the forefront. Morris et al. (2018) modelled star-spot sizes and temperatures for the M8V star TRAPPIST-1 using *Kepler* and *Spitzer* light curves. *Spitzer* data served to constrain star-spot radii and temperatures. Using only *Kepler* data, we simultaneously modelled star-spot and facula radii and intensities. Assuming that the magnetic features radiate as black bodies, we converted intensity to temperature for each feature. The mean star-spot temperature is 3470 ± 250 K. Relative to the stellar effective temperature of 3820 K, the mean contrast between star-spots and the unspotted photosphere is -350 K. Similarly, the mean facula temperature is 4020 ± 60 K, yielding a mean temperature contrast of $+200$ K. The contrasts are modest in relation to the solar contrast of -850 K and typical of the contrasts observed for other M dwarfs (Mancini et al. 2017).

Lomb–Scargle analysis of the irradiance loss due to star-spots yields a short-term activity cycle of 295 ± 50 d. Estrela & Valio (2016) estimated short activity cycles for two solar-type stars, 460 ± 60 d for Kepler-63 and 410 ± 50 d for Kepler-17. They also found a cycle of 305 ± 60 d for HAT-P-11 (Kepler-3), a spotted K4 dwarf (Estrela & Valio 2017). The short cycles may parallel short-term solar activity. A periodicity of roughly 154 d has been observed in solar cycles during times of maximum activity. This cycle may be indicative of the interaction of the local magnetic field and differential rotation (Zaqarashvili et al. 2010 and references therein). Quasi-biennial oscillations observed for the Sun occur on time-scales of 200 d to 4 yr. A possible explanation for these oscillations is the interplay of magnetic field components (Balogh et al. 2014). We propose that a dynamic dynamo drives Kepler-45's short-term periodicity as it does in the Sun.

As predicted by Donati et al. (2008) for early M dwarfs, we find rotation period to be latitude dependent. The 15.520 ± 0.025 d rotation period at the transit latitude calculated from correlation of flux difference due to star-spots and faculae at longitudes mapped in a frame rotating with the star is smaller than the 15.762 d mean period. Applying a solar differential profile, we estimate a rotational shear of $\Delta\Omega = 0.031 \pm 0.004$ rad d^{-1} and relative differential rotation of $\Delta\Omega/\bar{\Omega}$ of 7.8 ± 0.9 per cent. Over a decade ago, Reiners & Schmitt (2003) noted that slowly rotating solar-type stars had the most noticeable differential rotation. Their conclusion did not include M dwarfs. The trend was later confirmed by Reinhold et al. (2013) and Reinhold & Gizon (2015) for Kepler stars including M dwarfs. They calculated relative shear values between 0.01 and 0.11 rad d^{-1} for cool stars with a rotation period of roughly 15 d. Küker et al. (2019) later proposed a relative shear value of 0.045 rad d^{-1} for early M dwarfs (0.66 $M_\odot$, $T_{\rm eff} = 4038$ K) with the same rotation period. Our value lies within the range published by Reinhold & Gizon (2015) and is in line with the relative shear offered by Küker et al. (2019) given that Kepler-45 is somewhat cooler and less massive (0.59 $M_\odot$, $T_{\rm eff} = 3820$ K).

To summarize, this work has provided the first analysis of *Kepler* transit light-curve data for the hot Jupiter hosting early M dwarf Kepler-45, including mapping of star-spot and facula features. The results are consistent with observed solar-type spot activity, differential rotation, and sometimes rapid activity cycles observed for other red dwarfs, and demonstrate the ability of transit mapping to detail surface activity even for relatively faint red dwarf targets. The Kepler-45 system also provides a particular opportunity for future study of the impacts of host star activity on a close-in giant planet.

ACKNOWLEDGEMENTS

The authors would like to thank the anonymous referee for comments and suggestions that improved the content herein.

AV acknowledges partial financial support from Brazilian agency FAPESP (São Paulo Research Foundation) (# 2013/10559-5).

This paper includes data from the *Kepler* mission. Funding for the *Kepler* mission is provided by the National Aeronautics and Space Administration (NASA) Science Mission directorate. *Kepler* light-curve data were obtained from the NASA Exoplanet Archive, which provides public access to *Kepler* Mission data. The primary archive of all *Kepler* data is provided by the Mikulski Archive for Space Telescopes at the Space Telescope Science Institute (MAST at STScI). The Kepler Time Series Program Interface provides access to Kepler parameters. We thank the *Kepler* team for their efforts in providing the data and interfaces used in preparing this paper.

REFERENCES

Apai D., Pascucci I., 2010, Astrobiology Science Conference 2010, Evolution and Life: Surviving Catastrophes and Extremes on Earth and Beyond, League City, Texas
Apai D. et al., 2018, preprint (arXiv:1803.08708)
Astudillo-Defru N., Delfosse X., Bonfils X., Forveille T., Lovis, C, Rameau J., 2017, A&A, 600, A13
Bakos G. et al., 2018, preprint (arXiv:1812.09406v1)
Balogh A., Hudson H. S., Petrovay K., von Steiger R., 2014, Space Sci. Rev., 186, 1
Balona L. A., Obedigamba O. P., 2016, MNRAS, 461, 497
Barnes S. A., 2010, ApJ, 722, 2222
Barnes J. R., Collier Cameron A., Donati J. -F., James D. J., Marsden S. C., Petit P., 2005, MNRAS, 357, L1
Barnes J. R., Jeffers S. V., Jones H. R. A., 2011, MNRAS, 412, 1599
Barnes J. R., Jeffers S. V., Haswell C. A., Jones H. R. A., Shulyak D., Pavlenko Ya. V., Jenkins J. A., 2017, MNRAS, 471, 811
Basri G. et al., 2011, ApJ, 141, 20
Baylis D. et al., 2018, MNRAS, 475, 4467
Berdyugina S. V., 2004, Sol. Phys., 224, 123
Berdyugina S. V., 2005, Living Rev. Sol. Phys., 2, 8
Berger T. A., Huber D., Gaidos E., van Saders J. L., 2018, ApJ, 866, 99
Biazzo K., Frasca A., Catalano S., Marilli E., Henry G. W., Taz G., 2002, Mem. Soc. Astron. Ital. Suppl., 2, 220
Bochanski L. L., Hawley S. L., Covey K. R., West A. A., Ried I. N., Golimowski D. A., Ivezic Z., 2010, AJ, 139, 2679
Boisse I., Bouchy F., Hébrard G., Bonfils X., Santos N., Vauclair S., 2011, Proc. IAU Symp. 273, The Physics of Sun and Star Spots. Kluwer, Dordrecht, p. 281
Bondar N. I., 1995, A&AS, 111, 259
Borucki W. J., 2010, Science, 327, 977
Borucki W. J. et al., 2011, ApJ, 728, 117
Brown T. M., Latham D. W., Everett M. E., Esquerdo G. A., 2011, AJ, 142, 112
Bucconi A. P., Diaz R. F., Luoni M. L., Abrevaya X. C., Mauas P. J. D., 2011, AJ, 141, 34
Charbonneau P., 2010, Living Rev. Sol. Phys., 7, 3

Dai F., Winn J. N., Berta-Thompson Z., Sanchis-Ojeda R., Albrecht S., 2018, AJ, 155, 177
Davenport J. R. A., Hebb L., Hawley S. L., 2015, ApJ, 806, 212
Delfosse X., Forveille T. S., Mayor M., 1998, A&A, 338, L67
Diez Alonso E. et al., 2015, ApJ, 621, A126
Donati J.-F. et al., 2008, MNRAS, 390, 545
Durney B. R., De Young D. S., Roxburgh I. S., 1993, Sol. Phys., 145, 207
Estrela R., Valio A., 2016, ApJ, 831, 57
Estrela R., Valio A., 2017, Proc. IAU Symp. 328, Living Around Active Stars. Kluwer, Dordrecht, p. 152
Fabbian D. et al., 2017, Astron. Nachr., 338, 753
Fan Y., Fang F., 2014, ApJ, 789, 1
Fang X.-S., Zhao G., Zhao J.-K., Chen Y.-Q., Kumar Y. B., 2016, MNRAS, 463, 2494
Giles H. A. C., Collier Cameron A., Haywood R. D., 2017, MNRAS, 472, 1618
Gomes da Silva J., Santos N. C., Bonfils X., Delfosse X., Forveille T., Udry S., 2011, A&A, 534, A30
Gomes da Silva J., Santos N. C., Bonfils X., Delfosse X., Forveille T., Udry S., Dumusque X., Lovis C., 2012, A&A, 541, A9
Goodman J., Weare J., 2010, Commun. Appl. Math. Comput. Sci., 5, 68
Guinan E. F., Engle S. G., 2009, Proc. IAU Symp. 258, The Ages of Stars. Kluwer, Dordrecht, p. 395
Hartman J. D. et al., 2011, ApJ, 141, 5
Hartman J. D. et al., 2015, AJ, 149, 166
Hathaway D. H., 2015, Living Rev. Sol. Phys., 12, 2
Hawley S. L., Davenport J. R. A., Kowalski A. F., Wisniewski J. P., Hebb L., Dietrick R., Hilton E. J., 2002, ApJ, 797, 121
Hébrard É. M., Donati J.-F., Delfosse X., Morin J., Moutou C., Boisse I., 2016, MNRAS, 461, 1465
Hogg D. W., Foreman-Mackey D., 2018, ApJS, 236, 11
Jao W.-C., Henry T. J., Gies D. R., Hambly N. C., 2018, ApJ, 861, L11
Jeffers S. V. et al., 2018, A&A, 614, A76
Jeffries S. D., James D. J., Bromage G. E., 1994, MNRAS, 271, 476
Jenkins J. M. et al., 2010, ApJ, 173, L87
Johnson J. A. et al., 2012, AJ, 143, 111
Kipping D. M., 2016, MNRAS, 455, 1680
Kiraga M., Stępień K., 2013, Acta Astron., 57, 149
Küker M., Rudiger G., Oláh K., Strassmeier K.-G., 2019, A&A, 622, A40
Lehtinen J., Jetsu L., Hackman T., Kajathari P., Henry G. W., 2016, A&A, 588, A38
Mancini L. et al., 2017, MNRAS, 465, 843
Marcy G. W., Butler R. P., Vogt S. S., Fischer D., Lissauer J. J., 1998, ApJ, 505, L147
McQuillan A., Aigrain S., Mazeh T., 2013, MNRAS, 432, 1203
McQuillan A., Mazeh T., Aigrain S., 2014, ApJS, 211, 24
Mehrabi A., He H., Khosroshahi H., 2017, ApJ, 834, 207
Messina S., Pizzolato N., Guinan E. F., Rodono M., 2003, A&A, 410, 671
Morris B. M., Agol E., Davenport J. R. A., Hawley S. L., 2018, ApJ, 857, 39
O'Neal D., 2006, ApJ, 645, 659
O'Neal D., Neff J. E., Saar S. H., Cuntz M., 2004, AJ, 128, 1802
Oláh K. et al., 2014, A&A, 501, 703
Rajpurohit A. S., Reylé C., Allard F., Homeier D., Schultheis M., Bessell M. S., Robin A. C., 2013, A&A, 556, A15
Reiners A., Schmitt J. H. M. M., 2003, A&A, 398, 647
Reiners A., Joshi N., Goldman B., 2012, AJ, 143, 93
Reinhold T., Gizon L., 2015, A&A, 583, A65
Reinhold T., Reiners A., Basri G., 2013, A&A, 560, A4
Robertson P., Endl M., Cochran W. D., Dodson-Robinson S. E., 2013, ApJ, 764, 3
Saar S. H., Donahue R. A., 1997, ApJ, 485, 319
Savanov I. S., 2012, Astron. Rep., 56, 716
Shields A. L., Ballard S., Johnson J. A., 2017, Phys. Rep., 663, 1
Silva A. V. R., 2003, ApJ, 585, L147
Silva-Valio A., Lanza A. F., 2011, A&A, 529, 36
Silva-Valio A., Lanza A. F., Alonso R., Barge P., 2010, A&A, 510, 25
Sing D. K., Désert J.-M., Lecavelier Des Etangs A., Ballester G. E., Vidal-Madjar A., Parmentier V., Hebrard G., Henry G. W., 2009, A&A, 505, 891
Smith J. C. et al., 2012, PASP, 124, 919
Solov'ev A. A., Kirichek E. A., 2019, MNRAS, 482, 5290
Stumpe M. C. et al., 2012, PASP, 124, 984
Thompson S. E. et al., 2016, Kepler Data Release Notes (KSCI-19065-002)
Valio A., Estrela R., Netto Y., Bravo J. P., de Medeiros J. R., 2017, ApJ, 835, 2
Vida K. et al., 2010, Astron. Nachr., 331, 250
Vida K., Oláh K., Szabó R., 2014, MNRAS, 441, 2744
West A. A., Hawley S. L., Bochanski J. J., Covey K. R., Reid I. N., Dhital S., Hilton E. J., Masuda M., 2008, AJ, 135, 785
West A. A. et al., 2011, AJ, 141, 97
Zaleski S. M., Valio A., Marsden S. C., Carter B. D., 2019, MNRAS, 484, 618
Zaqarashvili T. V., Carbonell M., Oliver R., Ballester J. L., 2010, ApJ, 709, 749
Zucker S., Mazeh T., Santos N. C., Udry S., Mayor M., 2003, A&A, 404, 775

This paper has been typeset from a TEX/LATEX file prepared by the author.

Magnetic activity maps of Kepler-45's surface at transit latitude -33.2° demonstrate moderate solar-type activity for this slow rotator ($v \sin i \simeq 2$ km s^{-1}). The modest number of transit band starspots and faculae may be indicative of a rotation-activity relation for M dwarfs which states that activity increases with increasing rotation as for G-K stars (Messina et al., 2003; Kiraga & Stepien, 2011; Hawley et al., 2014). Similar to their solar counterparts, starspots are observed within ±20° longitude of disk center in the observer's frame, whereas faculae are observed closer to the stellar limbs. The spot area coverage of approximately 4% is less than that of active G-stars but more than that of the current, quiet Sun.

Autocorrelation of the flux deficit for mapped starspots yields a short magnetic activity cycle of 295 ± 50 days. In comparison, a short-term variability of ≈ 154 days and quasi-biennial oscillations (QBOs) as short as ≈ 219 days and as long as ≈ 4 years have been observed for the Sun. QBOs are proposed to be produced by solar dynamo processes: near-surface differential rotation and shear at the tachocline (Bazilevskaya et al., 2014, and references therein).

Applying a solar differential rotation profile over latitudes 0° to 90° for a transit latitude rotation period of 15.520 days derived from starspots and faculae and a mean stellar rotation period of 15.762 days, Kepler-45's rotational shear is 0.031 ± 0.004 rad d^{-1}, corresponding to a relative differential rotation of 7.8 ± 0.9%. This shear is consistent with the calculations of Küker et al. (2019) for early M dwarfs. They calculate a shear in the range 0.028 to 0.047 rad d^{-1} for rotation periods of 1 to 10 days, with shear increasing as rotation period increases.

As on the Sun, starspots are cooler than and faculae are hotter than the quiet photosphere. Under the assumption that starspots and faculae radiate as black bodies, their intensities may be converted to temperatures via Planck's Radiation Law. The mean starspot temperature is 3470 ± 250 K, and the mean facula temperature is 4020 ± 60 K. Relative to the unspotted photosphere with an effective temperature of 3820 K, the mean contrasts are -350 K for starspots and +200 K for faculae. These are modest

as compared to solar contrasts and not surprising given the low luminosity of an M dwarf (Evren, 1999; Andersen & Korhonen, 2015; Shields et al., 2016).

> We do not know what the rules of the game are; all we are allowed to do is watch the playing. Of course, if we watch long enough, we may eventually catch on to a few of the rules.
>
> Richard Feynman

Chapter 4 An Exomoon Search using Accumulated Transits of the Kepler-45 System

The inspection of Kepler-45 transit light curves (Chapter 3) revealed two classes of flux modulation: aperiodic variations due to starspots and faculae, and periodic variations due to an unknown source. Starspot and facula modulations are strictly confined to the in–transit portion of light curves since these features must be occulted by an exoplanet as it traverses a stellar face in order to be detected. On the other hand, observed periodic variations appear both in–transit and out–of–transit, thus raising the question "Is there a second exoplanet orbiting between the host star and Kepler-45b or does Kepler-45b have a satellite?"

If there is a second planet in the Kepler-45 system having an orbital period less than that of Kepler-45b and a radial size meeting the *Kepler* detection threshold of $0.5R_{\oplus}$, its orbit would produce a secondary set of periodic dimmings in the transit light curves independent of those caused by the orbit of Kepler-45b. The observed flux reductions appear only in conjunction with the transits of Kepler-45b and not independently. Thus, they suggest photometric evidence of an exomoon in the Kepler-45 system.

Investigation of exomoon signatures in the Kepler-45 transit light curves followed

a multi-step approach, which may be adapted to any stellar system having a transiting planet. The star-planet model employed in Zaleski et al. (2019, 2020a) was first modified to include a simulated moon in order to estimate physical parameters for a companion to Kepler-45b. The eccentricity of the planet's orbit was also considered, and Kepler's equations of motion were incorporated to fully describe the planet's orbital position. Synthesized light curves for the planet in a prograde orbit with the moon in both prograde and retrograde orbit were fit to observed data via an MCMC algorithm to derive exomoon characteristics. Next, the solution for the orbital period and direction of a super-Earth exomoon in a stable orbit were used to accurately predict exomoon angular phase relative to planet position. Bayesian metrics also favored a planet+moon model over a planet-only model. A complete description of the periodic flux amplitude variations attributed to the exomoon and the methodology for evaluating those variations and inferred exomoon physical characteristics are presented in the following paper, "An Exomoon Search using Accumulated Transits of the Kepler-45 System" (Zaleski et al., 2020b).

4.1 Zaleski et al. (2020b) "An Exomoon Search using Accumulated Transits of the Kepler-45 System"

The manuscript in submission Zaleski et al. (2020b), "An Exomoon Search using Accumulated Transits of the Kepler-45 System", follows.

Draft version August 1, 2021
Typeset using LaTeX **twocolumn** style in AASTeX631

An Exomoon Search using Accumulated Transits of the Kepler-45 System

S. M. Zaleski,[1] A. Valio,[2] A. H. F. Guimarães,[3] B. D. Carter,[1] and S. C. Marsden[1]

[1] *Centre for Astrophysics*
University of Southern Queensland
Toowoomba, 4350, Australia
[2] *Centre for Radio Astronomy and Astrophysics*
Mackenzie Presbyterian University
São Paulo, SP 01302-907, Brazil
[3] *National Institute for Space Research*
Av. dos Astronautas, 1758, São José dos Campos, Brazil

ABSTRACT

The search for exomoons has moved to the forefront of astronomy given the significance of moons in understanding the formation, evolution, and even habitability of planetary systems. Among the search methods available, the transit method also holds great promise, given the wealth of extensive precision data from Kepler and other space missions. Here, we present a new multi-step methodology and use of accumulated light-curves to offer a flexible framework for the comparison of theoretical exomoon signatures to exoplanet transit photometry. As a case study, we present an analysis of the Kepler-45 system, an M dwarf orbited by a single hot Jupiter. Remarkably, our results offer some tantalising indications that the exoplanet may be orbited by a massive super-Earth over 2 times the size and 11 times the mass of Earth, and following a retrograde orbit with a period 1.09 d, a 9:4 resonance with the exoplanet orbital period. The analysis of accumulated transits for Kepler-45 and other low-mass stars with large transiting planets may thus present a new opportunity to survey for exomoons and so advance understanding of the formation and evolution of planetary systems.

Keywords: planets and satellites: detection, dynamical evolution and stability — methods: analytical

1. INTRODUCTION

While stellar systems other than our own may not replicate the planetary architecture of the Solar System, the hundreds of moons in our system lead to the belief that a variety of moons exist in the Galaxy. It is only reasonable to assume that many exoplanets have exomoon companions (Horner et al. 2020). Similar to the ratio of planets to moons in the Solar System, the number of exomoons may greatly outweigh the number of exoplanets. Given the continuing advances in telescope instrumentation and the ever increasing number of exoplanet discoveries, a catalog of exomoons will eventually accompany the list of exoplanets.

The search for exomoons is an extension of the search for exoplanets. The majority of exoplanets have been discovered via periodic variations in radial velocity measurements (Lovis & Fischer 2010) or periodic dimmings in stellar light curves (Borucki & Summers 1984; Charbonneau et al. 2006). Changes in a star's radial velocity due to gravitational forces between the star and an orbiting body is a dynamic effect, whereas repeated, u-shaped modulations of stellar flux due to a transiting exoplanet in periodic orbit is a photometric effect. The capability to measure changes in an exoplanet's radial velocity due to an exomoon's gravitational force does not currently exist. Yet, the dynamic and photometric effects which may appear as light curve variations act as barometers for assessing the presence of an exomoon.

Dynamic, or barycentric, effects due to the planet-moon forces affect the planet orbital position and cause an exomoon to alter the transit profile of the planet. An exomoon may dynamically alter the tangential component of a planet's velocity relative to the observer's line-of-sight thereby resulting in deviations to the planet's periodicity measured at the expected times of mid-transit (transit timing variations, or TTV's) and shortening/lengthening of transit duration (transit duration variations, or TDV's) (Kipping 2009). The blockage of

stellar irradiance by an exomoon will cause equivalent photometric effects, *i.e.* photometric timing and transit duration variations, PTV's (aka TTV_p's, Szabo et al. (2006); Simon et al. (2007)) and PDV's, respectively. When both a planet and a moon transit their host star, the ingress of a moon prior to the planet will cause a decrease in flux to occur sooner than if there were only a planet, thus increasing the width, or duration, of the transit. The same occurs if the moon egresses after the planet, extending the duration of the transit. The ingress or egress of a secondary orbiting body will also cause photometric transit-timing variations.

An additional photometric effect is the change in transit depth, or photometric radius variations, PRV's (aka TRV's, Rodenbeck et al. (2020)), due to both a transiting planet and moon. An exomoon's blockage of stellar flux commensurate with its position relative to a transiting planet will produce a periodic transit deepening from which the planet's and exomoon's radii may be inferred. At moon-planet conjunction, the moon's effect will be minimum.

Exomoon confirmation may require more than TTV measurements, though they may be the only avenue for discovery when the sensitivity is below photometric detection limits. To date, tentative detection of exomoon candidates have arisen from transit flux modulation and TTV measurements. The flux modulation proposed to be a signal of an exomoon candidate orbiting the gas giant Kepler-90g was found to be a false positive (Kipping 2015). The exomoon candidate, Kepler-1625b-i, was proposed by Teachey & Kipping (2018a) given significant TTV's in the mid-transit times of Kepler-1625b, a Jupiter-sized planet in a 287.4 d wide orbit about a G-type star (Morton et al. 2016). Limited observation of a blended moon-planet transit supported the claim. Fox & Weigert (2020) recently explored the possibility of indirectly detecting exomoon candidates from TTV measurements. They examined 13 *Kepler* systems of which 8 systems had signals that could be explained by the presence of an exomoon. Independent analyses of exomoon candidate Kepler-1625b-i (Heller 2018; Kreidberg et al. 2019) and the stellar systems studied by Fox & Weigert (2020) (Kipping & Teachey 2020; Quarles et al. 2020) have not yet resulted in the confirmation of an exomoon candidate.

In this work, we focus on the search for exomoon signals in transit photometry and address an approach for the analysis of stellar systems for which significant transit light curve data is available. In Section 2, we describe theoretical exomoon photometric effects on individual transits and explore the relationship among those effects as an exomoon indicator. To best demonstrate our methodology, the Kepler-45 system is used as a case study. The system is introduced in Section 2, with a description of photometric variations as observed in the Kepler-45 transit light curves. Following our multi-step analytic process outlined in Section 3, we examine and correlate variations in the more than 300 accumulated transit light curves of Kepler-45 to test if a moon signal could be highlighted. In consideration are the flux amplitude variations not attributable to starspots and faculae occulted during planetary transit. In Section 4, we test whether an exomoon could be dynamically stable. A discussion of our methodology and the results of its application are presented in Section 5 with a concluding summary in Section 6.

2. KEPLER-45 TRANSIT LIGHT CURVES

The detection of exomoons via photometry requires high temporal resolution light curves with detail fine enough to distinguish a transiting exoplanet from its transiting companion. Data from the *Kepler* mission are applicable to the detection of exomoons as small as 0.3 $R_\oplus$ (Tusnski & Valio 2011). Moreover, red dwarfs, which are significantly smaller than the Sun, are particularly well suited to the detection via transit (Borucki & Summers 1984; Deeg & Alonso 2018) of exoplanets and exomoons that may orbit relatively close to their star (Mann et al. 2012; Kopparapu 2013). Moreover, of great interest are hot Jupiters orbiting red dwarfs given the large ratio of planet to star radii and, thus, the higher detection probability compared to that of smaller planets. Also, the significant transit depths for hot Jupiters orbiting M dwarfs make possible the detection of flux modulations in transit light curves due to sizable exomoon companions.

The Kepler-45 system is one of a few known dwarf star transiting hot Jupiter systems. Its star, an M1 red dwarf, hosts a single planet, the hot Jupiter Kepler-45b (Johnson et al. 2012). System parameters are listed in Table 1. The planet orbits close to its stellar host at 0.03 au (Zaleski et al. 2020) and outside the star's habitable zone. Though not suited for habitability studies, the Kepler-45 system is a prime target for photometric analysis of transiting bodies.

2.1. *Observed transits*

Flux data for Kepler-45 is publicly available in the final data release of the *Kepler* mission (Data Release 25 (Twicken et al. 2016; Mathur et al. 2017)) for *Kepler* quarters 6 - 8 and 10 - 17. Using the Pre-search Data Conditioning Simple Aperture Photometry (PDCSAP) flux, we recently reported an analysis of magnetic activity via temporal mapping of starspots and faculae on the

Table 1. Kepler-45 System: Stellar and Planetary Parameters

Parameter	Value	Reference
Star		
Spectral type	M1V	Johnson et al. (2012)
Kepler magnitude (K_p)	15.979	Brown et al. (2011)
Mass ($M_\odot$)	0.59 ± 0.06	Johnson et al. (2012)
Radius ($R_\odot$)	0.624 ± 0.019	Berger et al. (2018)
Rotation Period (d)	15.762 ± 0.016	Zaleski et al. (2020)
Age (Gyr)	$0.80\ ^{+0.70}_{-0.50}$	Bonomo et al. (2017)
Limb darkening coeff 1, c_2	$1.45\ ^{+0.04}_{-0.03}$	Zaleski et al. (2020)
Limb darkening coeff 2, c_3	$-1.349\ ^{+0.013}_{-0.012}$	Zaleski et al. (2020)
Limb darkening coeff 3, c_4	$0.776\ ^{+0.009}_{-0.010}$	Zaleski et al. (2020)
Planet		
Mass (M_{Jup})	$0.4945\ ^{+0.0004}_{-0.0008}$	this work
Radius (R_{Jup})	$1.115\ ^{+0.023}_{-0.019}$	this work
Radius (R_{star})	$0.179\ ^{+0.004}_{-0.003}$	this work
Semi-major axis (au)	0.0299 ± 0.0007	this work
Semi-major axis (R_{star})	10.33 ± 0.24	this work
Mid-transit star-planet distance (au)	0.0318 ± 0.0007	this work
Mid-transit star-planet distance (R_{star})	11.0 ± 0.2	this work
Inclination angle (°)	$87.4\ ^{+1.4}_{-1.6}$	this work
Orbital period (d)	2.455239 ± 0.000004	Johnson et al. (2012)
Eccentricity	$0.149\ ^{+0.008}_{-0.007}$	this work
Angle of periastron (°)	212 ± 5	this work

stellar surface (Zaleski et al. 2020). We found that the low luminosity, early M1 dwarf Kepler-45 exhibits solar-type behaviour with areas of intense magnetic fields in the photosphere and a solar-type differential rotation profile (faster equatorial rotation than polar rotation).

Sectioning the PDCSAP short cadence (SC) data by the 2.455 d orbital period of Kepler-45b yielded 331 transits, which were then normalized, polynomial adjusted, and aligned to mid-transit (t = 0 h). Residuals from the subtraction of a planetary transit model from the SC transit light curves showed two distinct types of flux amplitude variation during transits: positive amplitude differences due to occulted starspots and negative amplitude differences due to occulted faculae or a possible satellite of Kepler-45b. Occultation of starspots on the stellar surface was noted as a distinctive increase in flux having a bump-like shape present on the order of minutes (Silva 2003). Faculae were observed close to the stellar limbs, where their occultation produces u-shaped depressions in the light curve proximal to planetary ingress or egress and lasting only minutes.

On the other hand, temporally extended decreases in flux on the order of half an hour to one hour were detected both in the in–transit and out–of–transit data of several transits, suggesting a change in irradiance due to another orbiting body rather than to starspots or faculae (Tusnski & Valio 2011; Teachey & Kipping 2018a; Teachey et al. 2018b). Examples of flux decreases prior or after the planetary transit are shown in Figure 1. To exclude the presence of a previously undetected inner planet, out–of–transit data were searched for periodic dimmings. The lack of periodic evidence for a second planet was verified using the *Transit Least Squares* (TLS) algorithm (Hippke & Heller 2019). Further, the periodic biases that induce observational effects leading to false exomoon detections are not present in Kepler-45b short cadence data (Szabo et al. 2013).

To additionally confirm that the modulations apparent in PDCSAP data were non-systematic, we detrended and normalized the Single Aperture Photometry for Kepler-45 using the CoFiAM algorithm (Kipping 2013). CoFiAM removes long-term trends while preserving transits and closely adjacent out–of–transit data. We found no difference in flux modulations between PDCSAP and SAP transits. Thus, the source of modulations not due to starspots and faculae warranted investigation and presented the option of an exomoon candidate.

2.2. *Theoretical transits*

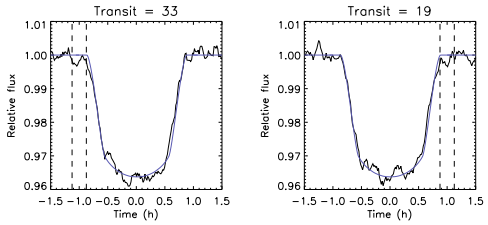

Figure 1. Limited by the vertical dashed lines are the depressions prior (transit 33) or after (transit 19) the planet ingress or egress that could be imprints of an orbiting moon.

The signatures of spots, or dark features on the surface of the star, and the shadow of an orbiting moon, albeit small, are not the same and can be differentiated. Figure 2 exemplifies the differences in transit signatures of starspot-facula (top left panel) versus moon (bottom left panel). The transit of a planet across a spotless stellar surface produces a smooth, U-shaped curve (black curve in Fig. 2, left panels), while a bump will appear in the curve if the planet crosses in front of a starspot (blue curve of Fig. 2, top left panel). Conversely, the occultation of a facula will cause a dip in the light curve (Fig. 2, top left panel). A planet+moon transit (Fig. 2, bottom left panel, red curve) is deeper than a planet only transit for a spotless stellar surface. The deepest portion of the transit well reflects the stellar surface areas blocked by the planet and moon, whereas the shallower portion reflects blockage by the planet only. A leading moon transit causes a decrease in stellar flux prior to planetary ingress (bottom left panel of Fig. 2, red curve, left shaded area). Angular positions of the moon in its orbit with respect to the planet are depicted in Fig. 2, bottom right panel.

In the planet+moon transit (Fig. 2 bottom left panel, red curve), the greater transit depth from -0.7 to +0.3 h is due to the joint planet+moon occultation of the stellar surface, while the transit depth from 0.3 to 0.7 h indicates the planet only transit (the moon has already egressed the stellar disc). The time period of flux decrease due to the moon transit is determined by the orbital position of the moon with respect to the planet as the planet approaches transit. An out–of–transit reduction in flux prior to planet ingress (Fig. 2, red curve, bottom left) or post planet egress is also dependent on moon phase as the moon's motion leads or trails the planet's motion, respectively.

2.3. *Photometric exomoon indicators*

We noted in our previous study of the Kepler-45 magnetic activity from starspot mapping that many transits

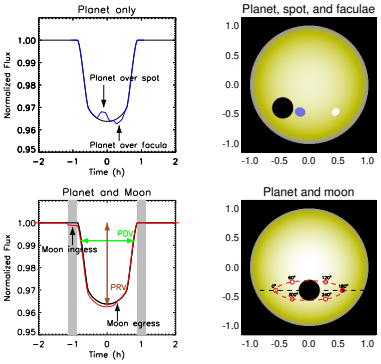

Figure 2. Effects of starspot/facula or exomoon in transit light curves. Top: Signatures of a starspot and a facula in a transit light curve (left) as they would appear on the stellar surface (right). The stellar surface is a yellow disc, with the planet, starspot, and facula shown as black, gray and white discs, respectively. **Bottom:** Effects of an exomoon on the transit light curve shown as variations in depth (PRV) and duration (PDV), as well as the relative flux in the wings just before planet ingress and after planet egress (shaded areas). An inclined orbit of the moon about the planet (black disc) is depicted by the dashed red ellipse with the moon position marked at 6 phase angles relative to the planet by red circles (right). The phase angle is defined relative to x-y axes in which the negative x-axis is 0° and the negative y-axis is 270° moving clockwise.

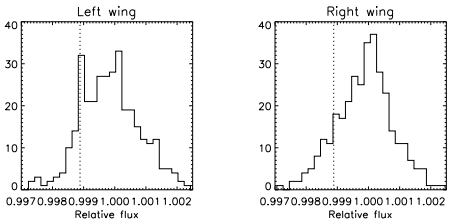

Figure 3. Relative flux distributions before and after planetary transits, within 15 min before ingress (left) and after egress (right), as delimited by the shaded vertical regions in the bottom left panel of Figure 2. A peak at intensity of 0.9989 in the left panel may indicate the presence of an exomoon transiting ahead of the planet in about 10% of the transits.

of Kepler-45b revealed flux modulations that could be interpreted as a moon transiting with its host planet (Zaleski et al. 2020). Subtraction of a model of the transiting hot Jupiter Kepler-45b from observed transits revealed flux amplitude modulations due to starspots. Additionally, interesting indicators of the presence of a

moon also surfaced as out–of–transit step-downs either before or after the transit when only the moon is transiting the star. The decrease in flux seen just before ingress of Kepler-45b transit 33 (622.54961 BKJD) or just after egress of transit 19 (588.17634 BKJD), are examples of potential exomoon transits ahead of (Fig. 1, left panel) or after the planet transit (Fig. 1, right panel).

Since it is difficult to disentangle moon signals from those due to starspots/faculae during transit, we began the search for moon transit signals in the short periods just before ingress or shortly after egress of the planet (for example, the time interval between the vertical dashed lines of Figure 1). The average flux within 15 min before or after the steep decrease in flux (delimited by the dashed lines) was estimated for all transits. The distributions of these fluxes before (left wing) and after (right wing) the planet transit are shown in Fig. 3. A signal of the presence of a moon will show itself in the histogram as a secondary peak with flux smaller than 1 (the normalized flux). Indeed, there is a peak at flux equal to 0.9989 in the histogram of the left wing relative flux before planet ingress (dotted vertical line in the left panel of Fig. 3). This flux decrease of 0.0011 is compatible with the transit of an object of radius $\sqrt{0.011} = 0.033 R_{star}$. We considered this indicator to be the first piece of an exomoon puzzle.

We next investigated variations in transit depth and width, as well as mid-transit time for observed transits. First, transit depth, or Photometric Radius Variation (PRV), was estimated within ±18 min of transit center time for each observed transit. The results are plotted as a histogram in the top panel of Fig. 4, where three peaks may be distinguished. The main peak at around PRV = 0.036 is related to the the transit of a single planet with a radius of 0.1794 R_{star} (noted by the blue line). The second peak at around PRV = 0.0353 is thought to be caused by the presence of spots located close to the center longitude of the star, which translates to "bumps" close to mid-transit. Finally, we interpret the third peak around PRV = 0.037 as due to the presence of an exomoon which further increases the depth of the transit. Importantly, this difference in transit depth due to the shadow of an exomoon is consistent with the observed decrease of 0.0011 in relative flux in the wings of the transits (Fig. 3, top left panel), at pre-ingress of the planet. The red vertical lines are the result of the applied exomoon model that is discussed in Section 3.3.

Second, transit width, or duration, defined as the time interval during which the flux was equal to 0.992 (refer to the green horizontal arrow in Fig. 2, bottom left panel), was also measured for all transits. The variation in duration, or Photometric Duration Variation (PDV),

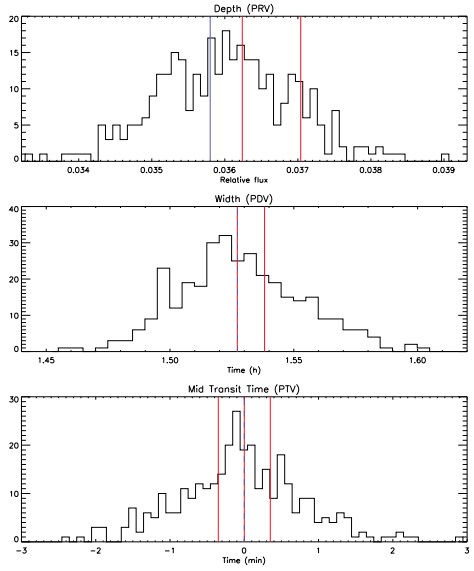

Figure 4. Photometric variations measured in (from top to bottom) transit depth, or PRV; transit duration, or PDV; and mid-transit time, or PTV. The vertical blue lines are the expected results for a planet-only transit, whereas the red lines are the expected parameters for simulated light curves using the parameters obtained from *emcee* for the moon-planet-star model (Section 3.3). There are multiple values depending if the moon is in conjunction with the planet (where the moon shadow is minimum) or at all other phases.

is plotted in the second panel of Fig. 4. The transit duration of a planet-only model is marked by the blue dashed vertical line. The two red lines at 1.527h and 1.538h indicate the predicted durations for the moon-inclusive model, described in the Section 3.3.

Third, photometric variations of the timing of transit centre (PTV's) were measured as the mid-time between the times of ingress and egress when the flux was equal to 0.992 (Fig. 2, bottom left panel). PTV's occur due to the moon's ingress and egress separately from the planet. The results are shown in the bottom panel of Fig. 4. As can be seen, there is a spread between ±2 min. The vertical dashed blue line at zero shows that no PTV is expected for a planet-only model. Again the three red lines are the results from the moon model explained in Section 3.3. All these variations may be subtle indications of the presence of a moon orbiting Kepler-45b.

The correlation between transit timing and duration variations have been studied by Heller and others (Kipping 2009; Heller et al. 2016; Rodenbeck et al. 2020). Depth variations are commensurate with the effects of a transiting moon and should be included for a comprehensive correlation. Periodicities in transit timing, duration, and depth should reveal periodicities of the stellar system, and may be related to the orbital period of an exomoon.

The individual Lomb-Scargle periodograms of the photometric variations (PRV, PDV, and PTV) measured for all transits spanning a period of about 1000 days showed many peaks (see Fig. 5). However, the periodicity due to a moon should be the same for all three types of photometric variations. Thus, to highlight the periodicity, we multiplied the individual power spectra for PRV, PDV, and PTV. The result is pictured in the bottom panel of Fig. 5. The periodogram product shows a strong peak at 16.26 ± 0.23 d and a secondary one at 9.59 ± 0.08 d. The secondary peak is approximately equal to 4 times the planet's orbital period. There is no obvious physical explanation for the primary peak. Thus, we propose that it is associated with the periodic transit of a potential exomoon and the second exomoon indicator. This possibility will be further investigated in the next section.

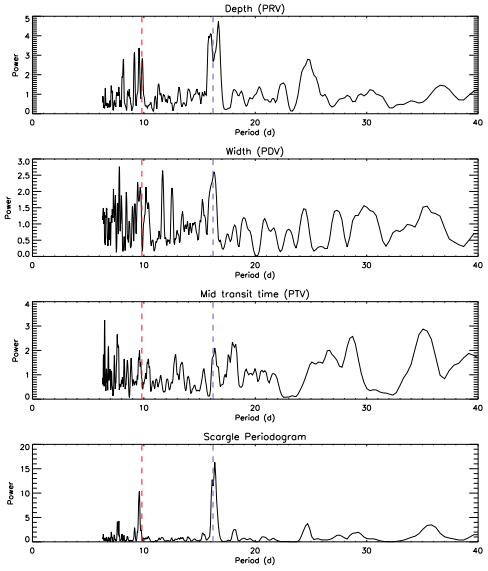

Figure 5. Lomb-Scargle periodograms of the photometric variations PRV, PDV, and PTV are shown in the top three panels. **Bottom:** The product of PRV, PDV, and PTV periodograms, where two main peaks are evident. The dashed red vertical line at 9.6d is about 4 times the planet's orbital period, whereas the vertical blue dashed line indicates the maximum power at a period of 16.2d, that will be further investigated.

3. METHODOLOGY: TESTING PHOTOMETRIC INDICATORS

Due to the noise of the Kepler-45 light curves, the search for small signals of an exomoon within single transits would be inconclusive. Examination of transits on a cumulative basis reveal indicators of unexplained affects. Therefore, to determine if light curve modulations could be due to an exomoon, we analysed all the transits jointly employing a multi-step methodology:

1. Markov Chain Monte Carlo (MCMC) analysis of transit light curves to estimate system parameters using a photometric star-planet model for a planet in elliptical orbit;

2. Addition of a moon in circular orbit to the star-planet model and estimation of the moon's physical parameters via a second MCMC analysis of transit light curves;

3. Comparison of the star-planet model to the star-planet-moon model via the Bayesian criterion for model selection to determine which model better describes observed data;

4. Re-assessment of photometric light curve variations in light of an moon, including photometric timing variations (PTV's), photometric transit duration variations (PDV's), and photometric radius variations (PRV's);

5. Prediction of the moon's angular position, or phase, ephemeris with correlation to observed data via our new technique of eXomoon Phase Gating (XPG);

3.1. *MCMC modeling*

The star-planet-moon model is an extension of the star-planet model of the model of Silva (2003) used in previous studies of CoRoT and Kepler stars (Silva-Valio et al. 2010; Valio et al. 2017; Zaleski et al. 2019; Netto & Valio 2020; Zaleski et al. 2020; Araújo & Valio 2021). The original model considered circular orbits of a transiting planet. Here, the star-planet model has been upgraded to an exoplanet in an eccentric orbit. However, the star-planet-moon model considers the simplest case of an exomoon in a circular orbit.

We remind the reader that our methodology is intended to be adaptive, and an alternative model which returns physical parameters for an orbiting body may be employed.

3.1.1. *Star-Planet Model*

In our star-planet transit model, the stellar surface is represented as a limb-darkened, white light image. The 3-parameter stellar limb darkening law applied is given by Sing (2010):

$$\frac{I(\mu)}{I(1)} = 1 - c_2(1-\mu) - c_3(1-\mu)^{3/2} - c_4(1-\mu)^2 \quad (1)$$

where $I(1)$ is the maximum intensity at disc centre, c_2, c_3, and c_4 are the limb darkening coefficients, and $\mu = \cos(\theta)$, where θ is the angle between the line–of–sight and the emergent intensity.

The planet is represented as a dark, opaque disc with radius in units of stellar radius. Kepler-45b is defined to be in a low eccentricity, null obliquity, prograde orbit. The planet's orbital position is given by the solution to the time-dependent Kepler equation for eccentric anomaly (Klioner 2016). The orbit is rotated to 0° at mid-transit (t = 0 h) relative to the observer's line-of-sight, equivalent to true anomaly = 90° - angle of periastron. The planet's position relative to the pixelated stellar image is calculated from t = -2 h to t = 2 h in 2 min increments. Pixels overlapped by the planet are assigned a flux value of 0, corresponding to flux blockage. At each time, the stellar intensity equals the sum of all pixels in the stellar image. The model generates a smooth light curve as a function of time with a maximum normalized flux of 1.

To determine a baseline transit light curve for the orbit of Kepler-45b, the affine invariant MCMC sampler *emcee* (Foreman-Mackey et al. 2013) was employed to fit transit light curves generated by our star-planet model to an average of all complete short cadence transits in order to obtain estimates of the means and variances of select free parameters. The sampler evolved an ensemble of walkers in a parameters space delimited by a range of possible values of equal likelihood, or uniform priors, for free parameters being fit. The uniform priors for the free parameters are given in Table 2. The eccentricity and angle of periastron priors are based on the values $0.186\ ^{+0.11}_{-0.09}$ and $242\ ^{+16}_{-30}$, respectively, published by Bonomo et al. (2017). The stellar radius, R_{star}, was fixed at $0.624 R_{\odot}$.

The baseline star-planet transit model was constructed from the resulting most probable parameter values: planet radius 0.1794 R_{star}, inclination angle 87.45°, semi-major axis 10.33 R_{star}, eccentricity 0.149, and angle of periastron 211.5°.

Table 2. Uniform priors for star-planet model light curve fitting

Parameter	Range
Planet radius (R_{star})	[0.15 - 0.20]
Semi-major axis (R_{star})	[9 - 16]
Inclination angle (°)	[80- 100]
Eccentricity	[0.0 - 0.3]
Angle of periastron (°)	[200.0 - 270.0]

3.1.2. *Star-Planet-Moon Model*

A moon was added to the star-planet model to create a new star-planet-moon model incorporating a quantitative profile of exomoon orbital and physical parameters. The simplest case of a moon in circular orbit about Kepler-45b was considered. Though the simplest planet-moon orbital configuration is one in which the moon's orbit is coplanar to the planet's orbit, this may not be the case. Fig. 2 bottom right panel shows a case where the moon's orbital plane is inclined by 70° with respect to the star's spin axis.

The moon was represented by a dark, opaque disc. Its orbital direction was definable as either prograde or retrograde, with Kepler-45b in prograde orbit. The moon's orbital position is defined relative to a Cartesian coordinate system in which the negative x-axis represents 0° and and the negative y-axis represents 270° moving clockwise from the negative x-axis (see Fig. 2, bottom right panel). The moon phase angle $\theta(n)$ at mid-transit of the n^{th} transit is estimated by:

$$\theta(n) = \theta_0 \pm 2\pi\ n\ \frac{P_p}{P_m} \quad (2)$$

where P_p is the planet period, P_m is the moon period, and θ_0 is the phase of the moon at mid-transit of the very first transit. The plus sign defines prograde motion of the moon, whereas the minus sign refers to a retrograde moon orbit.

The planet-moon distance is calculated at each iteration of the model from the moon's orbital period using Kepler's Third Law. Assuming a non-negligible mass for the moon, the distance is given by

$$d_m = \left[\frac{G(M_p + M_m)P_m^2}{4\pi^2}\right]^{1/3} \quad (3)$$

where d_m is the planet-moon distance, G is the Gravitational constant, M_p and M_m are the planet and moon masses, and P_m is the moon's period.

From the planet's distance to the star, orbital period, and inclination angle, and the moon's distance to the

Table 3. Uniform priors of exomoon parameters

Parameter	Range
Radius (R_p)	[0.20 - 0.60]
Mass ($M_\oplus$)	[1.0 - 12.0]
Orbital period (d)	[0.03 - 1.57]
Inclination angle (°)	[0.0 - 90.0]
Phase angle (°)	[0.0 - 360.0]

planet, orbital period, orbital phase, and inclination angle, the positions of both the planet and moon are calculated from t = -2 h to t = 2 h in 2 min increments. Assuming that the planet-star orbital distance does not vary greatly during transit, the planet-star distance is that at mid-transit, as given by

$$a_{mt} = \frac{a_p(1-e^2)}{1+e\ \sin\omega} \tag{4}$$

where a_{mt} is the planet-star distance at mid-transit, and a_p, e, and ω are the semi-major axis, eccentricity, and periastron angle of the planet's orbit.

At each 2 min interval, the stellar intensity equals the sum of all pixels in the stellar image not covered by the planet and moon. The model thus generates a smooth light curve as a function of time for star+planet+moon.

For either orbital direction of the moon, star-planet-moon transit light curves generated by *emcee* from the model as it moved through parameter space were fit to unbroken SC for all *Kepler* quarters. The moon's radius, mass, period, orbital inclination angle, and initial phase relative to the planet during first mid-transit were free parameters sampled from uniform priors that delimited realistic parameter values of equal probability. The moon priors are listed in Table 3. The minimum and maximum periods are those which are possible at distances equivalent to 33% and 100% of the Hill radius for a planet of Kepler-45b's mass. The planet radius and planet-star distance of the planet+moon system were fixed, using values from the baseline transit light curve.

The *emcee* transit fit for prograde orbital motion of both the moon and planet resulted in an exomoon radius of 0.034 R_{star} in a 1.09 d orbit about the planet at a distance of 2.5×10^5 km. Estimated parameters with uncertainties are given in Table 4. The moon's estimated mass is $11.0 M_\oplus$, placing it in the super-Earth/mini-Neptune classification. The centre–of–mass of the planet–moon system lies within Kepler-45b at approximately 30% of its radius. The planet's and moon's orbital inclination angles are 87.5° and 73°, respectively, and thus, the orbits of the planet and the moon are not co-planar.

The fit for a retrograde exomoon again yielded a super-Earth or mini-Neptune sized exomoon with similar parameters for the prograde solution, *i.e.*, radius $0.035 R_{star}$ and mass 11.1 $M_\oplus$ in a 1.09 d orbit around the planet. Table 4 lists all fit parameters. The values for fit parameters agree with those from the prograde orbit analysis within $\pm1\sigma$ confidence, where the lower and upper errors correspond to the 16% and 84% quantiles.

Table 4. Exomoon Candidate Parameters

Parameter	Prograde	Retrograde
Mass ($M_\oplus$)	$11.0\ ^{+0.7}_{-0.9}$	$11.1\ ^{+0.6}_{-1.1}$
Radius ($R_\oplus$)	$2.35\ ^{+0.20}_{-0.22}$	$2.36\ ^{+0.23}_{-0.21}$
Radius (R_{star})	0.034 ±0.003	0.035 ±0.003
Inclination angle (°)	$73\ ^{+7}_{-8}$	$73\ ^{+6}_{-7}$
Orbital period (d)	$1.09\ ^{+0.13}_{-0.12}$	$1.09\ ^{+0.15}_{-0.10}$
Planet-moon distance (R_p)	$3.2\ ^{+0.4}_{-0.5}$	$3.2\ ^{+0.8}_{-0.4}$
Planet-moon distance (10^5 km)	$2.5\ ^{+0.3}_{-0.4}$	$2.5\ ^{+0.6}_{-0.3}$
Initial phase of orbit (°)	290^{+28}_{-29}	290^{+30}_{-40}

3.2. *Bayesian Metrics*

A planet+moon transit model constructed from derived exomoon parameters may or may not yield a series of synthetic light curves that demonstrates a better fit to observed data than a planet-only transit model. The goodness-of-fit to observed data for transits generated by a planet+moon model versus a planet-only model was assessed via the Bayesian Information Criterion (BIC) (Schwarz 1978). The BIC provides for comparison of models with different free parameters and selection of the model with the lowest BIC score. The BIC score of a model is classically defined as

$$BIC = -2\ lnP(x|k) + k\ ln(n) \tag{5}$$

where k is the number of free parameters, n is the number of points in the dataset, and $P(x \mid k)$ is the likelihood of the parameters given the observed data.

Assuming that the model errors are independent and that the model parameters have been well constrained by *emcee*, the BIC may be redefined in terms of the error variance as (Clement 2014)

$$BIC = n\ ln(\sigma^2) + k\ ln(n) \tag{6}$$

where σ^2 is the error variance, or in the commonly used form,

$$BIC = \chi^2 + k\ ln(n) \tag{7}$$

where χ^2 is the goodness-of-fit of a model to observed data.

When the number of free parameters differs between models, the penalty term $kln(n)$ assists in resolving the difference between models. While a more complex model

is expected to trend well to the data and yield a lower Bayesian metric than a simpler model, it is penalized for extra parameters when computing the metric. If the number of free parameters is the same between models, comparing BIC scores indicates which model is a better statistical fit to data.

If the planet+moon model is able to simulate the blended transits of a moon and planet that match observed transits, that model will be more probable and yield a lower Bayesian metric than a planet-only model. We note that any starspots and/or faculae present in observed transit light curves will equally affect the fits and scores for both models.

The planet-only model has 5 free parameters (semi-major axis, eccentricity, inclination angle, planet radius, and the planet's angular orbital position). The planet+moon model introduces moon-specific parameters (moon radius, mass, orbital inclination, period, and initial phase angle).

The score difference, ΔBIC, between models is defined as

$$\Delta BIC = \frac{\Sigma(BIC_{p+m}) - \Sigma(BIC_p)}{N_t} \quad (8)$$

where BIC_{p+m} and BIC_p are the BIC values for each transit as compared to the planet+moon and planet-only models, respectively, and N_t is the total number of complete transits. Scores were calculated for 245 data points spanning -2 h to +2 h about mid-transit and 329 unbroken transits.

When compared to observed data, simulated transits for the star-planet-moon model yielded a lower Bayesian score, or BIC, than those for the star-planet model. For the planet with a moon in either a prograde or retrograde orbit versus a planet with no moon, Δ BIC was ≃ -5.8. A significant, negative ΔBIC offers support for a meaningful planet+moon model but without preference to moon orbital direction.

3.3. *Photometric variations*

Preference of a moon-inclusive model infers that photometric variations due to an exomoon are present in observed transits and can be simulated. Thus, we re-examined the variations of transit depth and width as well as mid-transit time for observed data. Simulations of the planet-moon model, with the parameters given in Table 4, were performed for comparison to the observed data. The results are presented as the red vertical lines in the plots in Fig. 4, explained in the following.

The transit depth estimated from simulations of the planet-moon model resulted in the two values represented by the red lines depending on the moon's phase with respect to the planet, as shown in the top panel of Fig. 4. The red line at 0.0362 marks the shallower depth when the moon is at or near conjunction with the planet (90° and 270° phases, see Fig. 2, bottom right panel) but not totally occulted by the planet due to its inclined orbit; the other red line at 0.037 corresponds to the transit depth of planet+moon for all other moon phases.

In the second plot, that of PDV, the two red lines at 1.527h and 1.538h indicate the predicted durations for the moon-inclusive model. The width at 1.527h is coincident with the planet-only model width and represents the planet and moon in conjunction. The width of 1.538h will occur when the moon is not in conjunction with the planet and transits either ahead of or behind the planet.

Photometric variations of the timing of transit centre (PTV's) were again measured as the mid-time between the times of ingress and egress when the flux was equal to 0.992 (Fig. 2, bottom left panel). When a moon described by the parameters estimated via *emcee* is considered (see Table 4), its transit ahead or after the planet's transit shifts the time of mid-transit by -0.35 min or +0.35 min, respectively. These values are marked by the red lines in Fig. 4, with the one at 0 min coinciding with the expected PTV for a planet-only model.

Due to its small radial size, the moon only deepens the transit by about 0.0012 relative flux units (or 0.0004 when in planet conjunction). Nevertheless, the PRV distribution is seen to extend to values higher than the planet-only expected value. Moreover, the shadow of a moon also increases the transit duration by about 0.011 h (or 40s). While this cannot be seen directly in the data, the observed PDV distribution appears to be skewed to higher values of transit duration. Finally, whereas no PTV is expected for a planet-only model, the observed distribution does seem to be broader than a simple Gaussian centred on the blue line at 0 min.

The multiplication of the individual power spectra for PRV, PDV, and PTV, pictured in the bottom panel of Fig. 5, showed a strong peak at 16.26 ± 0.23 d and a secondary one at 9.59 ± 0.08 d. The primary peak in the Scargle periodogram (blue dashed line in Fig. 5, bottom panel), which was previously unquantified, reveals a coupling between the planet's orbital period, P_p, and the moon's orbital period, P_m, as derived by *emcee*. The moon completes 9 revolutions around the planet while the planet orbits the star 4 times. Thus, the synodic period of the moon, given by $P_{syn} = P_p P_m/(P_p - P_m)$, is 1.966 d. The 4 P_p = 9.82 d periodicity is seen in the periodogram of PRV, PDV, and PTV variations (Fig. 5, red dashed line), as well as the 9 P_{syn}/P_m = 16.2 d (Fig. 5, bottom panel, blue dashed line).

3.4. *eXomoon Phase Gating - XPG*

Moon-inclusive model transits that fit true data must also exhibit a repeatability in moon position, or angular phase, relative to the planet's position. The moon's angular position ephemeris is determined by its initial phase at the planet's first mid-transit and the ratio of the planet and moon orbital periods (see Eq. 2). An ephemeris spanning all observations was used to search for transits whose corresponding moon position matched within a defined angular gate (eXomoon Phase Gating, or XPG). Transits with gaps in data were disqualified from selection to enhance the clarity of exomoon modulations. Transits whose moon phase angle was within a $\pm 4°$ gate of each of the phase angles were averaged and compared to the planet+moon transit models for the moon at those phase angles. The gate width accommodated phase angle uncertainty while allowing a sufficient number of transits to pass.

XPG results for an exomoon in an 1.09 d retrograde orbit are shown in Fig. 6 for 6 moon phases. The transit averages include 9 to 11 transits for each phase, and the numbers of the transits included in the phase averages are enumerated in each panel of Fig. 6, with the numbering starting at transit 0. Transit numbers are converted to time at mid-transit by

$$t(n) = t_0 + n\ P_p \tag{9}$$

where $t(n)$ is the mid-transit time of the n^{th} orbit in BKJD, P_p is the planet period of 2.455 d, n is the transit number, and t_0 is the mid-transit time of transit 0, or 541.5269 BKJD.

The averaged transit light curves are shown in the panels of Fig. 6 as black irregular curves (smoothed every 5 data points). Averaging removes flux modulations due to starspots and faculae, which are short-lived relative to the orbital period of Kepler-45b, but preserves moon events in phase. The gray shaded areas represent averaged data uncertainty. The red curves depict the best fit models for an exomoon (given in Table 4) for each phase, whereas the blue curves represent the model transit of Kepler-45b only over an unspotted stellar surface. The residuals after subtraction of the models (planet only – blue curve, and planet+moon – red curve) from the observations are shown in the bottom part of each panel.

All planet+moon transits are generally deeper than the planet-only transit for the mean planet radius of 0.1794 R_{star}. At conjunction, when the moon is partially behind or in front of the planet relative to the observer's line–of–sight (90° and 270°), the planet+moon model almost matches the planet only model. Notably, the out–of–transit flux reductions near -1 h for a phase of 30° and +1 h for a phase of 210°, which are best seen in the residuals plots, are indicative of the moon's transit trailing the planet's transit and leading the planet's transit, respectively, as predicted by our model.

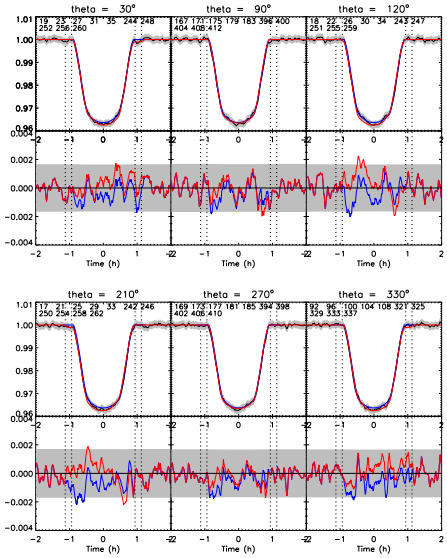

Figure 6. The moon-planet-star model compared to averaged transit data at 6 moon phases. The averaged transit data for each moon phase (theta) is shown by the black irregular curves, whereas the red curves represent moon-planet-star model configurations corresponding to the best fit parameters for the exomoon candidate. The blue curves represent the transit of Kepler-45b only over an unspotted stellar surface. The gray shaded areas represent averaged data uncertainty. The numbers of the averaged transits are given in the upper part of each panel. The residuals after subtraction of the planet only (blue curve) and moon-planet-star (red curve) models are shown in the bottom part of each panel. The vertical dashed lines depict the moon ingress and egress regions.

4. DYNAMICAL STABILITY

The degeneracy in orbital direction cannot be broken via light curve analysis (Lewis & Fujii 2014; Heller & Albrecht 2014b). Fitting transits to our star-planet-moon model for prograde and retrograde lunar orbits yields values for exomoon period, radius, mass, and initial phase angle that are similar within the uncertainties.

4.1. *Moon orbital constraints*

Orbital direction degeneracy may be resolved when considering the planet's Hill radius. The Hill radius de-

pends on both the planet and stellar masses, and the semi-major axis and eccentricity of the planet's orbit. The eccentricity of the planet's orbit reduces the Hill radius by a factor of $(1 - e)$, thereby changing the limits of orbital stability. The Hill radius for an eccentric planetary orbit is approximated by

$$R_{Hill} = a_p \left(\frac{M_p}{3M_{star}} \right)^{1/3} (1 - e) \quad (10)$$

where a_p and e are the semi-major axis and eccentricity of the planet's orbit, and M_p and M_{star} are the planet and stellar masses.

A median mass for Kepler-45b is obtained by substituting maximum a priori values for eccentricity and inclination from *emcee* fits and values for stellar mass, planet orbital period, and the RV semi-amplitude from Bonomo et al. (2017) in the following equation:

$$M_p \sin i = K \left(\frac{P_p \, M_{star}^2}{2\pi G} \right)^{1/3} \sqrt{1 - e^2} \quad (11)$$

where M_p and M_{star} are the planet and stellar masses, respectively. P_p, e, i, and K are the planet's orbital period, eccentricity, and inclination angle, and RV semi-amplitude. G is the gravitational constant.

For K = 107 m/s, i = 87.4 °, P_p = 2.455 d, and e = 0.149, the approximate mass of Kepler-45b is 0.4945 M_{Jup}, or 9.385×10^{26} kg. Given this estimate for M_p, and $M_{star} = 1.174 \times 10^{30}$ kg and $a_p = 4.486 \times 10^6$ km, Equation 10 yields an eccentric Hill radius of 2.467×10^5 km.

Moons with random inclination angles are projected to be stable when their orbital distance for non-eccentric orbits of both the planet and the moon is no more than 49% of the Hill radius for prograde orbits and no more than 93% for retrograde orbits (Domingos et al. 2006). For the Kepler-45 system, the estimated median planet-moon distance is roughly 2.47×10^5 km, thus placing the orbit of an exomoon candidate at close to 100% of the Hill radius. The only viable option for orbital direction is retrograde.

The minimum distance to which a moon can near the planet before it is disintegrated by tidal forces is defined by the Roche Limit. The Roche limit for rigid bodies is

$$R_{Roche} = 1.44 \; R_p \left(\frac{\rho_p}{\rho_m} \right)^{1/3} \quad (12)$$

where R_p is the planet radius, and ρ_p and ρ_m are the planet and moon densities.

The estimated planet and exomoon densities are ρ_p = 0.475 g/cm^3 and ρ_m = 4.656 g/cm^3, yielding a Roche limit of 5.237 x 10^4 km. A density of $4.6^{+0.5}_{-0.6}$ g/cm^3 lies midway between that of Earth and our moon, inferring a moon composition of rock/iron (Guimaraes & Valio 2018). The greater the moon's density, the higher the probability that its orbit is stable and that the moon can survive outside the Roche limit (within which it would be disintegrated by tidal forces) (Weidner & Horne 2010).

4.2. *Exomoon Evolution and Stability*

The external stability limit, or upper critical orbit a_E (Dvorak et al. 1989), which defines the circumplanetary region within which an exomoon can survive for any length of time, depends on the planet's Hill radius and the eccentricities of the planet and satellites. For prograde and retrograde orbits, the upper critical limits are fully expressed by the equations of Domingos et al. (2006) as

$$a_{E,pro} = R_{Hill} \; 0.4895(1 - 1.0305 \; e_p - 0.2738 \; e_{sat}) \quad (13)$$

and

$$a_{E,ret} = R_{Hill} \; 0.9309(1 - 1.0764 \; e_p - 0.9812 \; e_{sat}) \quad (14)$$

where e_p and e_{sat} are the eccentricities of the planet and its satellite, respectively, and R_{Hill} is the Hill radius for a zero eccentricity planetary orbit.

From the extensive literature devoted to determining the maximum distance from the central body at which an object would be in a stable orbit, the radial limit of about half of the Hill sphere, defined in Domingos et al. (2006) is commonly adopted. However, the equations do not expose all stable regions to some system conditions, such as the case of the Pluto-Charon sailboat region (Giuliatti et al. 2014).

Preliminary application of Equations 13 and 14 to our star-planet-moon system, assuming $e_p = e_{sat} = 0$ and a non-eccentric Hill radius of 2.899 x 10^5 km, yielded $a_{E,pro}$ = 1.82 R_p and $a_{E,ret}$ = 3.46 R_p. In light of an estimated mean planet-moon separation of 3.17 R_p, a prograde solution is well outside the critical limit for this type of orbit. One possibility for long term stability is a retrograde moon orbit with a semi-major axis within $3.17 \; ^{+0.8}_{-0.4} \; R_p$. Thus, the initial conclusion is that the moon could not be in a prograde orbit but could be in a retrograde orbit, albeit close to the reduced Hill radius.

In search of peculiarities of a Kepler-45b and moon system, we next considered the star-planet-moon dynamics as a three-body problem in general mode. We simulated exomoon stability as a function of planet-moon distance and orbital eccentricity considering the moon's inclination. We performed numerical long-term integrations ($\sim 10^4$ years) (Holman & Weigert 1999)

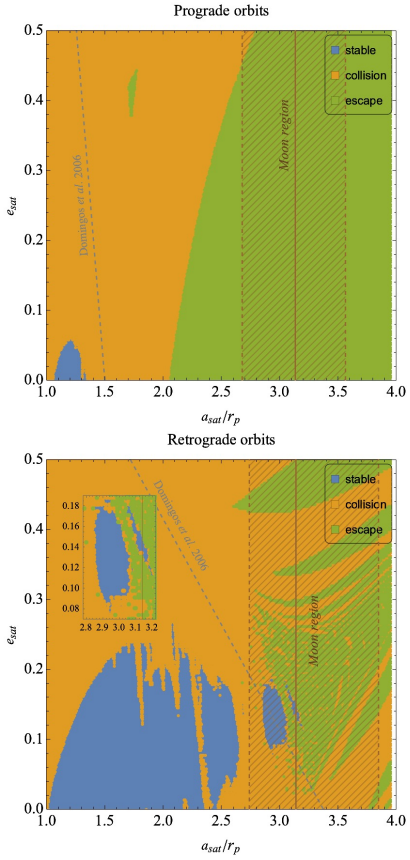

Figure 7. Regions of stability for orbits of a massive exomoon. The results of numerical simulations of a non-restricted 3 body system, with a moon of $11 M_{\odot}$ mass, over long-term integration in the initial condition space e_{sat} x a_{sat}, for prograde (top) and retrograde (bottom) orbits. The blue, orange, and green regions indicate stable, collision, and unstable orbits, respectively, after 10^4 years. The median semi-major axis of the moon, 3.17 R_p, and its uncertainty are marked by the solid and dashed red lines, respectively. Hashed lines highlight the regions of uncertainty. The inset in the bottom panel shows a blow-up of the stability region close to the moon distance obtained from the *emcee* results. The dashed blue curves signify the upper critical limits for prograde and retrograde orbits defined by Domingos et al. (2006).

of a circularly non-restricted 3 body problem (Szebehely 1967; Murray 1999) by employing the procedure of Vieira-Neto & Winter (2001), which uses the Radau integrator (Everhart 1985). The initial conditions for the moon were semi-major axis in the range $R_p \leq a_{sat} \leq a_p$, where a_p is the planetary semi-major axis, and eccentricity in the range $0.0 \leq e_{sat} \leq 0.5$. The initial conditions cover the same area of phase space described by Domingos et al. (2006). The intervals for a_{sat} and e_{sat} take into account the uncertainties in Table 4. In all simulations, the planet's orbit was co-planar with the stellar equator. Each simulation was integrated for a time up to 10^4 years. The integration is interrupted if the moon escapes the system or collides with the planet. Conversely, we considered the orbits stable if there is no change in the results over time.

The maps in Fig. 7 represent the results of the numerical simulations. The maps depict the stability, instability, and collision regions for a moon in prograde and retrograde orbits in the condition space $e_{sat} \times a_{sat}$, or the moon's eccentricity vs its orbital semi-major axis in units of planet radius. The solid blue areas represent regions of orbital stability. A dashed blue curve corresponding to the eccentric Hill radius limits passes through the plots, with the hashed region marking the planet-moon distance, or moon's semi-major axis, including uncertainty from *emcee*. For prograde orbits, there is no stable region for the moon. The moon would be fated to spiral inward or be ejected from orbit.

For retrograde orbits, the numerical simulations confirm stable regions outside the stability limit (Domingos et al. 2006) for profound trajectories - the blue "island" regions. The solid red line in Fig. 7, which represents the median semi-major axis of the moon, passes through a small "island" of stability. A larger "island" of stability lies within the region delimited by the semi-major axis uncertainty, thus indicating the possibility of an object orbiting the planet for long periods of time. The moon's orbit is slightly non-circular in both regions. Integration of points inside the "islands" for periods of up to $\sim 10^6$ years confirmed the long term stability. Only a negligible reduction in the island's edges due to late collisions were obtained. Thus, a moon could exist in these regions for at least one million years. The moon could possibly be caught in a resonant orbit depicted by the "islands", similar to the Pluto-Charon sailboat region (Giuliatti et al. 2014).

5. DISCUSSION

Astronomers (theoretical and observational) have investigated stellar system configurations suited to the discovery of extra-solar moons. In 2002, Barnes and

O'Brien (Barnes & O'Brien 2002) proposed that in stellar systems having a single giant planet, tidal forces will perturb an exomoon's orbit resulting in escape or collision with the planet. Theory currently limits the domain within which exomoons may orbit a giant planet to the habitable zones of target stars at distances of 0.4 - 0.6 au (Barnes & O'Brien 2002; Sasaki et al. 2012). There has not been an expectation of finding stable moons at closer distances. Piro (2018) estimated that the timescales for the ejection or disintegration of a moon in low-mass star systems varies from 1 Myr to 100 Gyr. Recently, Quarles et al. (2020) studied the effect of moon/planet mass ratio and planet-moon separation on circular orbit stability, hypothesizing that a massive, close-in moon will be subject to tidal migration. Their analyses also highlight the importance of photometric data, i.e. exomoon transits, to the confirmation of an exomoon.

The Kepler-45 system is relatively young with an estimated age of $0.80\ ^{+0.70}_{-0.50}$ Gyr. Thus, we may be viewing but a glimpse of the state of the Kepler-45 system. The significant amount of photometric data from the *Kepler* mission is but a time-released snapshot of the system's long-term evolution. The existence of a moon would present an interesting datapoint.

The existence of exomoons may be explained by various formation theories. Among them are accretion of planetesimals in the protosatellite disc on retrograde trajectories, capture of planet embryos in retrograde orbits or of a large moon by a close-in hot Jupiter, or confinement of satellites in the gap formed by a hot Jupiter in its proto-planetary disc (Gorkavyi 1993; Heller et al. 2014a; Namouni 2010; Sasaki et al. 2010; Lewis & Fujii 2014). In the particular case of a companion to Kepler-45b, the masses involved make formation of a super-Earth or a mini-Neptune from a circumplanetary disc seem unlikely in cooperation with the creation of a Jupiter-sized planet. The mass ratio of the planet and moon is roughly 0.07 whereas the mass ratio of Io+Ganymede+Europa+Callisto and Jupiter is 0.0004, over two orders of magnitude smaller.

Capture scenarios look more likely for a massive planet-moon pair. During the early evolution of the Kepler-45 system, Kepler-45b and the potential moon may have both been planets in orbit about the host star. With an estimated density of 4.7 g/cm^3, the moon may either be the remnant core of a gas planet which atmosphere was depleted by hydrodynamic escape due to radiation from the active M1 host star or a captured terrestrial planet. During an early phase of dynamic instability, the orbit of the less massive planet may have brought it close to the larger planet. This would allow for the smaller body to be tidally captured by the larger body and placed into orbit about Kepler-45b as a moon (Heller et al. 2014a; Hamers & Portegies Zwart 2018).

The fate of a moon, including bound orbit, inward spiral to collision, or outward migration ending in ejection, may be determined by various dynamic and physical factors: the moon's orbital period and direction, the initial spin period and current period of the planet, the initial separation between the planet and the star, tidal interaction with the planet and/or the gravitational attraction of the star (Barnes & O'Brien 2002; Zollinger et al. 2017; Piro 2018; Hansen 2019). The gravitational tug-of-war for the moon will be won by the star if the planet's initial spin period is short (on the order of a few hours) and transfer of the planet's angular momentum causes the moon to migrate outward to ejection. Further, the time to strip the moon from orbit varies directly with increasing star-planet initial separation. Conversely, when the planet's initial spin period is longer, tidal interactions cause the moon to migrate inward. When the moon reaches the Roche limit, it will be disintegrated by tidal forces. We estimate the average orbital semi-major axis of Kepler-45b's possible moon to be 2.47×10^5 km, or 4.72 times the planet's Roche limit, 5.24×10^4 km.

The moon's orbital period and the planet's rotation can also contribute to the time-dependent stability of the moon's orbit. Dynamic planet-moon interactions act to decrease the moon's orbital distance when the moon orbits faster than the planet rotates (Barnes & O'Brien 2002). Considering that the planet is tidally locked to the star, then its rotation period will be the same as its orbital period. The suspected moon orbits at 6.7×10^{-5} rad/s, faster than the planet rotates at 2.9×10^{-5} rad/s. Gravitationally induced torques would act to increase the planet's rotation period and decrease the planet-moon distance. Given the many factors that may affect an exomoon's orbit, it is safe to say that the long-term evolution of a moon remains unknown and cannot be firmly predicted without knowledge of the system's initial conditions.

6. CONCLUSIONS

The quest to understand the formation and evolution of planetary systems includes an ongoing search to robustly identify and characterize exomoons. Here, we focus on the flux modulations in transit light curves as possible exomoon indicators. A multi-step methodology for evaluating evidence of an exomoon in transit photometry is comprised of 1) Estimation of star-planet system parameters for a planet on an elliptical orbit through MCMC sampling to compare synthetic models to observed transits; 2) Addition of a moon in circular orbit about the planet and estimation of moon parameters via

a second MCMC analysis; 3) selection of the preferred model using Bayesian metrics; 4) analyses of photometric light curve variations due to a moon to include transit timing, duration, and depth variations; 5) prediction of the moon's angular position and phase ephemeris correlated with observed data. In the particular case of the Kepler-45 system, application of this methodology yielded results suggesting a possible moon. The moon is seemingly a super-Earth more than twice the size and eleven times the mass of Earth, and completing a retrograde orbit about the hot Jupiter planet in about 1.09d, in a 9:4 resonance with the planet orbital period. We conclude that the Kepler-45 system warrants further observation and investigation of an exomoon candidate. More generally, our approach to the analysis of accumulated transits for Kepler-45 and other low-mass stars with large transiting planets suggests a new opportunity to search for exomoons. Successful searches will in turn open up a new avenue of research by using exomoons to study the formation and evolution of planetary systems.

A.V. acknowledges partial financial support from São Paulo Research Foundation (FAPESP, grants #2013/10559-5 and #2018/04055-8), Brazil.

The transit light curve data is available at MAST: DOI:10.17909/t9-1564-vb03

REFERENCES

Araújo, A. & Valio, A. 2021, ApJL, 907, L5

Barnes, J. W. & O'Brien, D. P., 2002, ApJ, 755, 1087-1093

Berger, T., Huber, D., Gaidos, E., van Saders, J. L., 2018, AJ, 866, 99

Bonomo, A. S., Desidera, S., Benatti, S., Borsa, F., Crespi, S., Damasso, M., Lanza, A. F., Sozzetti, A., Lodato, G., Marzari, F., et al., 2017, A&A, 602, A107

Borucki, W. J. & Summers, A. L., 1984, Icarus, 58, 1

Brown, T. M., Latham, D. W., Everett, M. E., Esquerdo, G. A., 2011, AJ, 142, 112B

Cassidy, T. A., Mendez, R., Arras, P., Johnson, R. E., Skrutskie, M. F., 2009, ApJ, 704, 1341-1348

Charbonneau, D., Brown, T. M., Burrows, A., Laughlin, G., 2009, When Extrasolar Planets Transit Their Parent Stars, in Protostars and Planets V, Univ. of Arizona Press, 701

Clement, E. P., 2014, Amer. J. of Mathematic & Statistcs, 4, 214-221

Deeg, H.-J. & Alonso, R., 2018, Transit Photometry as an Exoplanet Discovery Method, in Handbook of Exoplanets, Springer International Publishing, 633-657

Domingos, R. C., Winter, O. C., Yokoyama, T., 2006, MNRAS, 373, 1227-1234

Dvorak, R., Froeschle, C., Froeschle, C., 1989, A&A, 226, 335-342 (1989).

Everhart, E., 1985, Dynamics of Comets: their origin and evolution, Springer, 185-202

Foreman-Mackey, D., Hogg, D. W., Lang, D., Goodman, J., 2013, PASP, 125, 306-312

Fox, C. & Weigert, P., 2020, MNRAS, 502, 2378-2293

Giuliatti, S. M., Winter, O. C., Vieira Neto, E., Sfair, R., 2014, MNRAS, 439, 3300

Gorḱavyi, N. N., 1993, Pisḿa v Astronomischeskii Zhurnal, 19, 448-456

Guimaraes, A. & Valio, A., 2018, AJ, 156, 50

Hamers, A. S. & Portegies Zwart, S. F., 2018, ApJL, 869, L27

Hansen, B. M. S., 2019, Sci. Adv., 5

Heller, R., Williams, D., Kipping, D., Limbach, M. A., Turner, E., Greenberg, R., Sasaki, T., Bolmont, E., Grasset, O., Lewis, K. et al., 2014a, Astrobiology, 14, 798-835

Heller, R. & Albrecht, S., 2014b, ApJ, 796, L1

Heller, R., Hippke, M., Placek, B., Angerhausen, D., Agol, E., 2016, A&A, 591, A67

Heller, R., 2018, A&A, 610, A39

Hippke, M. & Heller, R., 2019, A&A, 623, A39

Holman, M. & Wiegert, P., 1999, AJ, 117, 621-628

Horner, J., Kane, s. R., Marshall, J. P. et al., 2020, PASP, 132, 102001

Johnson, J. A., Gazak, J. K., Apps, K., Muirhead, P. S., Crepp, J. R., Crossfield, I. J. M., Boyajian, T., von Braun, K., Rojas-Ayala, B., Howard, A. W. et al., 2012, AJ, 143, 111

Kipping, D. M., 2009, MNRAS, 392, 181-189

Kipping, D. M., Hartman, J., Buchhave, L. A., Schmitt, A. R., Bakos, G., Nesvorný, D., 2013, ApJ, 770, 101

Kipping, D. M., Huang, X., Nesvorný, D., Torres, G., Buchhave, L. A., et al., 2009, AJ, 799, L14

Kipping, D. M. & Teachey, A., 2020, Serbian Astronomical Journal, 201, 25

Klioner, S. A., Basic Celestial Mechanics

Kopparapu, R. K., 2013, ApJ, 767, L8

Kreidberg, L., Luger, R., Bedell, M., 2019, ApJL, 877, L15

Lewis, K. M. & Fujii, Y., 2014, ApJ, 791, L26

Lovis, C. & Fischer, D., 2010, Radial Velocity Techniques for Exoplanets, in Exoplanets, 27-53

Mann, A. W., Gaidos, E., Lepine, S., Hilton, E. J., 2012, ApJ, 753, 90
Mathur, S., Huber, D., Batalha, N. M., Ciardi, D. R., Bastien, F. A., Bieryla, A., Buchhave, L. A., Cochran, W. D., Endl, M., Esquerdo, G. A. et al., 2017, ApJS, 229, 30
Morton, T., Bryson, S., Coughlin, J., Rowe, J. et al., 2016, ApJ, 822, 86
Murray, C., McDermott, S., 1999, Solar system dynamics, Cambr. Univ. Press
Namouni, F., 2010, ApJL, 719, L145-L147
Netto, Y. & Valio, A. 2020, A&A, 635, A78
Ni, D., 2010, A&A, 613, A32
Penev, K., 2010, Bouma, L. G., Winn, J. N., Hartman, J. D., AJ, 155, 165
Piro, A. L., 2018, AJ, 156, 54
Quarles, B., Li, G., Rosario-Franco, M., 2020, ApJL, 902, L20
Rodenbeck, K., Heller, R., Gizon, L., 2020, A&A, 638, A43
Sasaki, T., Stewart, G. R., Ida, S., 2010, ApJ, 714, 1052-1064
Sasaki, T., Barnes, J. W., O'Brien, D. P., 2012, ApJ, 754, 51
Schwarz, G., 1978, Annals of Statistic, 6, 461-464
Sestovic, M., Demory, B.-O., Queloz, D., 2010, A&A, 616, A76
Silva, A. V. R., 2003, ApJ, 585, L147-L150
Simon, A., Szatmáry, K., Szabó, Gy., M., 2007, A&A, 2, 727-731
Silva-Valio, A., Lanza, A. F., Alonso, R., & Barge, P. 2010, A&A, 510, A25
Sing, D. K., 2010, A&A, 510, A21
Szabó, Gy. M., Szatmáry, K., Divéki, SZ., Simon, A., 2006, A&A, 450, 395-398
Szabo, R., Szabo, Gy. M., Dalya, G., Simon, A. E., Hodosan, G., Kiss, L. L., 2013, A&A, 553, A17
Szebehely, V., 1967, Theory of orbits: the restricted problem of three bodies. NY: Acad. Press
Tusnski, L. R. M. & Valio, A., 2011, ApJ, 743, 97
Twicken, J. D., Jenkins, J. M., Seader, S. E., Tenenbaum, P., Smith, J. C., Brownston, L. S., Burke, C. J., Catanzarite, J. H., Clarke, B. D., Cote, M. T. et al., 2016, AJ, 152, 158
Teachey, A. & Kipping, D. M., 2018a, Sci. Adv., 4, eaav1784
Teachey, A., Kipping, D. M., Schmitt, A. R., 2018b, AJ, 155, 36
Valio, A., Estrela, R., Netto, Y., Bravo, J. P., & de Medeiros, J. R., 2017, ApJ, 835, 294
Vieira-Neto, E. & Winter, O. C., 2001, AJ, 122, 440
Weidner, C. & Horne, K., 2010, A&A, 521, A76
Zaleski, S. M., Valio, A., Marsden, S. C., & Carter, B. D., 2019, MNRAS, 484, 618
Zaleski, S. M., Valio, A., Carter, B. D., Marsden, S. C., 2020, MNRAS, 492, 5141-5151
Zollinger, R. R., Armstrong, J. C., Heller, R., 2019, MNRAS, 472, 8-25

Zaleski et al. (2020b) presents the search for an exomoon using an accumulation of transits and compelling evidence for an unexpected discovery - the first exomoon candidate detected in a red dwarf system. To wit, the accumulation of Kepler-45 transit light curves offers the strongest photometric evidence to date of an exomoon in any planet-hosting system.

The exomoon candidate is a super-Earth (11 $M_{\oplus}$, 2.3 $R_{\oplus}$) in a 1.092 day retrograde orbit about the hot Jupiter Kepler-45b. Multiple lines of evidence support the moon's quantitative profile as obtained via an MCMC algorithm:

- When a star-planet model and a star-planet-moon model are fit to observed data, the Bayesian Information Criterion strongly favors the latter model.
- Photometric transit variations (Photometric Timing Variations, Photometric Duration Variations, and Photometric Radius Variations) occur with the same periodicity.
- As observed in the out–of–transit SC Kepler-45 transit lights curves, pre-planetary ingress and post-planetary egress flux losses correspond to the exomoon leading and trailing the planet's orbit at a difference in angular position of 180° relative to the planet's position. Moon angular position, or phase, relative to the transiting planet can be predicted for all data quarters. The new technique of eXomoon Phase Gating (XPG), whereby transits are grouped by similar moon phase within a predefined angular gate, or uncertainty, correlated correct transit sequences.
- Simulations of exomoon stability yield regions of stability delimited by exomoon eccentricity and planet-moon distance. A moon as massive as Kepler-45b-1 can be bound in retrograde orbit.

A capture scenario is most likely for a massive exomoon. This exomoon candidate would offer an important datapoint for models of the formation and evolution of hot

Jupiters and the orbital stability of exomoons.

> Remember to look up at the stars and not down at your feet. Try to make sense of what you see and wonder about what makes the universe exist. Be curious. And however difficult life may seem, there is always something you can do and succeed at. It matters that you don't just give up.
>
> Stephen Hawking

Chapter 5 Discussion and Conclusions

5.1 The Magnetic Activity of Solar-Type Stars

The Sun is located near the center of the main sequence on the Hertzsprung-Russell diagram at a temperature of ≈ 6000 K. FGKM dwarf stars appear in the temperature range of ≈ 7000 - 2500 K, occupying the lower main sequence. This thesis has focused on the photometry of the G star Kepler-71 and the M dwarf Kepler-45 to examine their activity as compared to that of the Sun. How well does the observed behavior of these stars adhere to the processes of an $\alpha\Omega$ dynamo modeled after the Sun?

Kepler-71 and Kepler-45 differ in their physical parameters. Kepler-71 is younger and slightly smaller than the Sun (2.5 - 4.0 Gyr, 0.997 $M_{\odot}$, 0.887 $R_{\odot}$), whereas Kepler-45 is much younger and smaller (0.5 Gyr, 0.59 $M_{\odot}$, 0.624 $R_{\odot}$). Both are orbited by a single hot Jupiter, Kepler-71b and Kepler-45b, respectively, in a non-oblique orbit. Successive exoplanet orbits repeatedly probe the stellar surfaces of their respective hosts at the transit latitude defined by the semi-major axes and inclinations relative to stellar rotation axes of each star-planet system.

The studies presented in chapters 2 and 3 show that the magnetic phenomena, i.e. starspots and faculae, appear in the photospheres of Kepler-71 and Kepler-45 within the transit bands. These features behave as do their solar counterparts, with starspots visible closer to disk center than faculae which are observed closer to the stellar limbs. Starspot and facula parameters are summarized in Table 5.1. Intensities are scaled rel-

Table 5.1: Starspot and Facula Comparison

Parameter	Kepler-71	Kepler-45
Starspot		
Mean Radius (km)	$(51 \pm 26) \times 10^3$	$(40 \pm 17) \times 10^3$
Mean Intensity	0.55 ± 0.23	0.57 ± 0.22
Spotted area (%)	4.3	4.1
Facula		
Mean Radius (km)	$(67 \pm 25) \times 10^3$	$(45 \pm 16) \times 10^3$
Mean Intensity	1.19 ± 0.09	1.37 ± 0.12

ative to the unspotted photosphere (= 1).

The mean radial sizes of starspots and faculae on Kepler-71 are generally larger than those on Kepler-45 but show no correlation with the significant difference in stellar masses. Still, starspots on both exoplanets are bigger than a large sunspot (Silva-Valio et al., 2010). The coverage areas of starspots with the transit bands for the two stars are equivalent. Both target stars are slow rotators, with mean stellar rotation periods of 19.77 d for Kepler-71 and 15.76 d for Kepler-45. The level of stellar activity reflects the magnetic fields generated and sustained by a layered solar dynamo as a function of rotation. This rotation-activity relation by which activity increases with increasing rotation applies to M dwarfs as well as G dwarfs (Suárez Mascareño et al., 2016; Raetz et al., 2020). Thus, it is not surprising to observe a similar activity level for both stars, at least in the transit band.

Differential rotation is fundamental to the generation of large-scale magnetic fields such as those of the Sun and other stars (Kitchatinov & Nepomnyashchikh, 2017). The tachocline layer where a solidly rotating radiative core transitions to a differentially rotating convective zone is an area of shear great enough to produce large-scale magnetic fields. From stellar equatorial and transit latitude rotation rate, estimation of relative differential rotation and rotational shear are presented for the target stars in chapters 2 and 3 from, for the first time, the temporal longitudes of faculae as well as starspots. The values for Kepler-71 (rotational shear less than about 0.005 rad d^{-1} or a relative differential rotation less than 2%) infer an almost rigid but differential rotation, while the values for Kepler-45 (rotational shear of 0.031 rad d^{-1} or a relative

differential rotation of 7.8%) are within the theoretical range for an early M dwarf.

The traits of Kepler-71 and Kepler-45 largely fit the framework describing solar activity - from active longitudes for Kepler-71 to a short-term magnetic cycle for Kepler-45. While different in age and effective temperature, these dwarf stars indicate the closeness of a solar-stellar connection.

5.2 The Search for an Exomoon Candidate Orbiting Kepler-45b

Question arises as to the ability of a hot Jupiter to host an exomoon (Barnes & O'Brien, 2002; Trani et al., 2019). The existence of an exomoon companion complicates hypotheses on the provenance of hot Jupiters, which include in situ formation, disk migration, high eccentricity tidal migration, and pull-down capture (Dawson & Johnson, 2018). The addition of large exomoon to a star-planet system may introduce dynamics such as tidal interactions that destabilize the orbit of a hot Jupiter and cause both the hot Jupiter and the exomoon to be ejected (Trani et al., 2019).

Kepler-45b is a rare hot Jupiter orbiting a red dwarf. Few Jovian-sized planets orbit low mass M dwarfs, symptomatic of the dependency of planet formation on stellar mass (Alibert & Benz, 2017). A sizable exomoon companion to Kepler-45b may be rarer still. The possibility of sufficient material in the proto-planetary disk for the formation of both a Jupiter-sized planet and a super-Earth-sized moon is considered in Chapter 4. Also proposed are the capture of planet embryos or a planet, and the confinement of a planet-sized satellite in the proto-planetary disk gap. In the particular case of an exomoon companion to Kepler-45b, pull-down capture is most likely.

Kepler-45b's 2.455 d orbit is assumed to be stable, and the orbit of the exomoon candidate is proposed to be in a region of stability as well. The 1.092 d orbit of the super-Earth moon (11 $M_{\oplus}$, 2.3 $R_{\oplus}$) is stable if retrograde at a planet-moon distance of of 2.47×10^5 km, close to the planet's eccentric Hill radius. The moon completes 9 revolutions around the planet while the planet orbits the star 4 times. The moon's angular phases relative to the planet's position are predictable and correlate with in–transit and out–of–transit flux modulations. The photometric evidence for this exomoon is

compelling and warrants further observation of the Kepler-45 system.

5.3 Conclusions

This thesis highlights the broad application of transit photometry to offer new observational evidence for a solar-type dynamo active in G and early M stars, and the possible presence of an exomoon orbiting a hot Jupiter in a red dwarf system. *Kepler* photometry proves to be a valuable resource, with transit light curves containing a wealth of information. What began as the study of the solar-stellar connection led to a novel methodology for the identification of an exomoon. This body of work shows that flux amplitude variations not due to systematic noise or stellar variability may be attributed to two physical sources: magnetic features (starspots and faculae) and exoplanet companions. The physical characteristics of starspots and faculae observed in–transit serve to measure latitudinal and differential rotations, whereas the correlation of out–of–transit and in–transit flux losses evince the orbit of an exomoon.

5.4 The Future

The field of exoplanetary science has a bright future. Given the success of the CoRoT and *Kepler* missions, the start of operation of NASA/MIT's TESS program[1] in July 2018 and the future deployment of ESA's PLATO mission [2] in 2026 have been eagerly anticipated. These missions will observe bright stars in the solar neighborhood with the goal of detecting Earth-sized exoplanets. TESS is expected to find thousands of exoplanets, with ≈ 500 orbiting M dwarfs (Barclay et al., 2018).

TESS will observe some 200,000 stars, of which ≈ 7000 are M dwarfs, at a short cadence of 2 min over observation periods of ≈ 27 days to ≈ 1 year (Raetz et al., 2020). As compared to the almost 4 year observation length and 58.85 sec short cadence of the *Kepler* telescope, TESS observational parameters do not permit the measurement of long-term features such as magnetic activity cycles and may not permit assessment

[1] https://tess.mit.edu
[2] platomission.com

of differential rotation. Yet, hope remains that TESS will provide information beyond that of its primary goal as did *Kepler* whose goal was to discover Earth-sized exoplanets in the habitable zones of their stellar hosts.

The monitoring of FGKM stars by TESS offers the opportunity to expand upon the studies undertaken in this thesis. First, much remains to be learned about the rotation-activity relation for M dwarfs. TESS observations of magnetic activity (starspots, faculae, and flares) will yield new data points to enhance the understanding of the stellar dynamo. Second, investigation into the transits of the hot Jupiter TOI-564b will preview the evolutionary future of the Sun. The age of the mid-G star TOI-564 is approximated at 7.3 Gyr (Davis et al., 2020). Third, the mass-radius relationship for red dwarfs is poorly understood (Parsons et al., 2018). A knowledge of M dwarf radii and masses is required for the characterization of exoplanet mass, radius, and density. Fourth, the search for exoplanets and exomoons continues.

Our understanding of the solar dynamo is incomplete. Our knowledge of M dwarfs is wanting. The distribution of extra-solar moons is unknown. Answers lie in the study of new targets.

References

Note that the following references are for Chapters 1 and 5, and as appear in introductory and summary sections of the remaining chapters. References for the papers included in Chapters 2 - 4 are included in the references sections of those papers.

Adams, F. C., Bodenheimer, P., & Laughlin, G. (2005). M dwarfs:planet formation and long term evolution. *Astronomical Notes*, 326(10), 913–919.

Aerts, C., Christensen-Dalsgaard, J., & Kurtz, D. W. (2010). *Asteroseismology*.

Alibert, Y. & Benz, W. (2017). Formation and composition of planets around very low mass stars. *Astron. & Astrophys.*, 598, L5.

Ammler-von Eiff, M. & Reiners, A. (2012). New measurements of rotation and differential rotation in A-F stars: are there two populations of differentially rotating stars? *Astron. & Astrophys.*, 542, A116.

Andersen, J. M. & Korhonen, H. (2015). Stellar activity as noise in exoplanet detection – ii. application to m dwarfs. *MNRAS*, 448(4), 3053–3069.

Apai, D. & Pascucci, I. (2010). Different initial conditions for planet formation around cool and sun-like stars: Disk mass, disk structure, dust composition, and organics inventory. In *Astrobiology Science Conference 2010: Evolution and Life: Surviving Catastrophes and Extremes on Earth and Beyond*, volume 1538 (pp. 5396).

Arlt, R., Leussu, R., Giese, N., Mursula, K., & Usoskin, I. G. (2013). Sunspot positions and sizes for 1825-1867 from the observations by samuel heinrich schwabe. *MNRAS*, 433(4), 3165–3172.

Baglin, A. (2003). COROT: A minisat for pionnier science, asteroseismology and planets finding. *Advances in Space Research*, 31(2), 345–349.

Bakos, G. A., Bayliss, D., Bento, J., Bhatti, W., Brahm, R., Csubry, Z., Espinoza, N., Hartman, J. D., Henning, T., Jordán, A., Mancini, L., Penev, K., Rabus, M., Sarkis, P., Suc, V., de Val-Borro, M., Zhou, G., Butler, R. P., Crane, J., Durkan, S., Shectman, S., Kim, J., Lázár, J., Papp, I., Sári, P., Ricker, G., Vanderspek, R., Latham, D. W., Seager, S., Winn, J. N., Jenkins, J., Chacon, A. D., Fűrész, G., Goeke, B., Li, J., Quinn, S., Quintana, E. V., Tenenbaum, P., Teske, J., Vezie, M., Yu, L., Stockdale, C., Evans, P., & Relles, H. M. (2018). HATS-71b: A giant planet transiting an M3 dwarf star in TESS sector 1, eprint:1812.09406.

Barclay, T., Pepper, J., & Quintana, E. V. (2018). A revised exoplanet yield from the transiting exoplanet survey satellite (TESS). *Astrophys. J.S Series*, 239(1), 2.

Barnes, J. R., Collier Cameron, A., Donati, J. F., James, D. J., Marsden, S. C., & Petit, P. (2005). The dependence of differential rotation on temperature and rotation. *MNRAS*, 357(1), L1–L5.

Barnes, J. R., Jeffers, S. V., Haswell, C. A., Jones, H. R. A., Shulyak, D., Pavlenko, Y. V., & Jenkins, J. S. (2017). Surprisingly different star-spot distributions on the near equal-mass equal-rotation-rate stars in the M dwarf binary GJ 65 AB. *MNRAS*, 471(1), 811–823.

Barnes, J. W. & O'Brien, D. P. (2002). Stability of satellites around close-in extrasolar giant planets. *Astrophys. J.*, 575(2), 1087–1093.

Barr, A. C. (2017). Formation of exomoons: a solar system perspective. *Astronomical Review*, 12, 24–52.

Bayliss, D., Gillen, E., Eigmüller, P., McCormac, J., Alexander, R. D., Armstrong, D. J, ., Booth, R. S., Bouchy, F., Burleigh, M. R., Cabrera, J., & et al. (2018). NGTS-1b: a hot Jupiter transiting an M-dwarf. *MNRAS*, 475(4), 4467–4475.

Bazilevskaya, G., Broomhall, A.-M., Elsworth, Y., & Nakariakov, V. M. (2014). A combined analysis of the observational aspects of the quasi-biennial oscillation in solar magnetic activity. *Space Science Reviews*, 186, 359–386.

Beatty, T. G. & Seager, S. (2010). Transit probabilities for stars with stellar inclination constraints. *Astrophys. J.*, 712(2), 1433–1442.

Berdyugina, S. V. (2005). Starspots: A key to the stellar dynamo. *Living Reviews in Solar Physics*, 2(1), 8.

Berdyugina, S. V. & Usoskin, I. G. (2003). Active longitudes in sunspot activity: Century scale persistence. *Astron. & Astrophys.*, 405, 1121–1128.

Bonomo, A. S., Desidera, S., Benatti, S., Borsa, F., Crespi, S., Damasso, M., Lanza, A. F., Sozzetti, A., Lodato, G., Marzari, F., Boccato, C., Claudi, R. U., Cosentino, R., Covino, E., Gratton, R., Maggio, A., Micela, G., Molinari, E., Pagano, I., Piotto, G., Poretti, E., Smareglia, R., Affer, L., Biazzo, K., Bignamini, A., Esposito, M., Giacobbe, P., Hébrard, G., Malavolta, L., Maldonado, J., Mancini, L., Martinez Fiorenzano, A., Masiero, S., Nascimbeni, V., Pedani, M., Rainer, M., & Scandariato, G. (2017). The GAPS Programme with HARPS-N at TNG . XIV. Investigating giant planet migration history via improved eccentricity and mass determination for 231 transiting planets. *Astron. & Astrophys.*, 602, A107.

Bonomo, A. S. & Lanza, A. F. (2012). Starspot activity and rotation of the planet-hosting star kepler-17. *Astron. & Astrophys.*, 547, A37.

Borucki, W. J., Koch, D., Basri, G., Brown, T., Caldwell, D., Devore, E., Dunham, E., Gautier, T., Geary, J., Gilliland, R., Gould, A., Howell, S., & Jenkins, J. (2003). Kepler mission: a mission to find earth-size planets in the

habitable zone. In M. Fridlund, T. Henning, & H. Lacoste (Eds.), *Earths: DARWIN/TPF and the Search for Extrasolar Terrestrial Planets*, volume 539 of *ESA Special Publication* (pp. 69–81).

Borucki, W. J. & Summers, A. L. (1984). The photometric method of detecting other planetary systems. *Icarus*, 58(1), 121–134.

Brun, A. S., García, R. A., Houdek, G., Nandy, D., & Pinsonneault, M. (2014). The solar-stellar connection. *Space Science Reviews*, 196(1-4), 303–356.

Burke, C. J. (2008). Impact of orbital eccentricity on the detection of transiting extrasolar planets. *Astrophys. J.*, 679(2), 1566–1573.

Cañas, C. I., Stefansson, G., Kanodia, S., Mahadevan, S., Cochran, W. D., Endl, M., Robertson, P., Bender, C. F., Ninan, J. P., Beard, C., & et al. (2020). A warm jupiter transiting an m dwarf: A tess single-transit event confirmed with the habitable-zone planet finder. *Astrophys. J.*, 160(3), 147.

Cassidy, T. A., Mendez, R., Arras, P., Johnson, R. E., & Skrutskie, M. F. (2009). Massive Satellites of Close-In Gas Giant Exoplanets. *Astrophys. J.*, 704(2), 1341–1348.

Charbonneau, D., Brown, T. M., Burrows, A., & Laughlin, G. (2007). When extrasolar planets transit their parent stars. In B. Reipurth, D. Jewitt, & K. Keil (Eds.), *Protostars and Planets V* (pp. 701).

Charbonneau, P. (2014). Solar dynamo theory. *Annual Reviews of Astronomy and Astrophysics*, 52, 251–290.

Charbonneau, P. (2020). Dynamo models of the solar cycle. *Living Reviews in Solar Physics*, 17, 4.

Collier Cameron, A. (1986). *Starspot Imaging Using VRI Photometry*, volume 118.

Collier Cameron, A. (2007). Differential rotation on rapidly rotating stars. *Astron. Nachr.*, 328(10), 1030.

Davenport, J. R. A. (2015). The shape of M dwarf flares in Kepler light curves. *Proceedings of the International Astronomical Union*, 11(S320), 128–133.

Davis, A. B., Wang, S., Jones, M., Eastman, J. D., Günther, M. N., Stassun, K. G., Addison, B. C., Collins, K. A., Quinn, S. N., Latham, D. W., Trifonov, T., Shahaf, S., Mazeh, T., Kane, S. R., Wang, X.-Y., Tan, T.-G., Tokovinin, A., Ziegler, C., Tronsgaard, R., Millholland, S., Cruz, B., Berlind, P., Calkins, M. L., Esquerdo, G. A., Collins, K. I., Conti, D. M., Evans, P., Lewin, P., Radford, D. J., Paredes, L. A., Henry, T. J., James, H.-S., Law, N. M., Mann, A. W., Briceño, C., Ricker, G. R., Vanderspek, R., Seager, S., Winn, J. N., Jenkins, J. M., Krishnamurthy, A., Batalha, N. M., Burt, J., Colón, K. D., Dynes, S., Caldwell, D. A., Morris, R., Henze, C. E., & Fischer, D. A. (2020). TOI 564 b and TOI 905 b: Grazing and fully transiting hot jupiters discovered by TESS. 160(5), 229.

Dawson, R. I. & Johnson, J. A. (2018). Origins of hot Jupiters. *Annual Review of Astronomy and Astrophysics*, 56(1), 175–221.

Deeg, H. J. & Alonso, R. (2018). Transit photometry as an exoplanet discovery method. *Handbook of Exoplanets*, (pp. 633–657).

Deleuil, M., Aigrain, S., Moutou, C., Cabrera, J., Bouchy, F., Deeg, H. J., Almenara, J.-M., Hébrard, G., Santerne, A., Alonso, R., & et al. (2018). Planets, candidates, and binaries from the corot/exoplanet programme. *Astron. & Astrophys.*, 619, A97.

Domingos, R. C., Winter, O. C., & Yokoyama, T. (2006). Stable satellites around extrasolar giant planets. *MNRAS*, 373(3), 1227–1234.

Dorren, J. D. & Guinan, E. F. (1982). Evidence for starspots on single solar-like stars. *Astrophys. J.*, 87, 1546–1557.

Evren, S. (1999). Facular structures on cool stars. *Turkish Journal of Physics*, 23, 383–390.

Fischer, D. A., Howard, A. W., Laughlin, G. P., Macintosh, B., Mahadevan, S., Sahlmann, J., & Yee, J. C. (2014). Exoplanet detection techniques. *Protostars and Planets VI*.

Foreman-Mackey, D., Hogg, D. W., Lang, D., & Goodman, J. (2013). emcee: The MCMC hammer. *Publications of the Astronomical Society of the Pacific*, 125(925), 306–312.

Gilliland, R. L., Jenkins, J. M., Borucki, W. J., Bryson, S. T., Caldwell, D. A., Clarke, B. D., Dotson, J. L., Haas, M. R., Hall, J., Klaus, T., & et al. (2010). Initial characteristics of Kepler short cadence data. *Astrophys. J.*, 713(2), L160–L163.

Goodman, J. & Weare, J. (2010). Ensemble samplers with affine invariance. *Communications in Applied Mathematics and Computational Science*, 5(1), 65–80.

Granzer, T. (2004). Thin tube flux models for star spots. *Astron. Nachr.*, 325(5), 417–423.

Hale, G. E., Ellerman, F., Nicholson, S. B., & Joy, A. H. (1919). The magnetic polarity of sun-spots. *Astrophys. J.*, 49, 153–178.

Hawley, S. L., Davenport, J. R. A., Kowalski, A. F., Wisniewski, J. P., Hebb, L., Deitrick, R., & Hilton, E. J. (2014). Kepler flares. i. active and inactive M dwarfs. *Astrophys. J.*, 797(2), 121.

He, H., Wang, H., & Yun, D. (2015). Activity analyses for solar-type stars observed with Kepler I. proxies of magnetic activity. *Astrophys. J. Suppl. Series*, 221(1), 18.

Heller, R. (2018). Detecting and characterizing exomoons and exorings. *Handbook of Exoplanets*, (pp. 835–851).

Heller, R. & Albrecht, S. (2014). How to determine an exomoon's sense of orbital motion. *Astrophys. J.*, 796(1), L1.

Heller, R., Williams, D., Kipping, D., Limbach, M. A., Turner, E., Greenberg, R., Sasaki, T., Bolmont, E., Grasset, O., Lewis, K., & et al. (2014). Formation, habitability, and detection of extrasolar moons. *Astrobiology*, 14(9), 798–835.

Hogg, D. W. & Foreman-Mackey, D. (2018). Data analysis recipes: Using Markov Chain Monte Carlo. *Astrophys. J. Suppl. Series*, 236(1), 11.

Howe, R. (2009). Solar interior rotation and its variation. *Living Reviews in Solar Physics*, 6(1), 1.

Howell, S. B., Sobeck, C., Haas, M., Still, M., Barclay, T., Mullally, F., Troeltzsch, J., Aigrain, S., Bryson, S. T., Caldwell, D., & et al. (2014). The K2 mission: Characterization and early results. *Publications of the Astronomical Society of the Pacific*, 126(938), 398–408.

Hubbard, A., Rheinhardt, M., & Brandenburg, A. (2011). The fratricide of $\alpha\Omega$ dynamos by their α^2 siblings. *Astron. & Astrophys.*, 535, A48.

Iliev, I. K. (2010). Challenges of modern stellar spectroscopy: Doppler imaging and doppler tomography. *Publications de l'Observatoire Astronomique de Beograd*, 90, 91–96.

Isik, E., Schmitt, D., & Schüssler, M. (2011). Magnetic flux generation and transport in cool stars. *Astron. & Astrophys.*, 528, A135.

Jao, W.-C., Henry, T. J., Gies, D. R., & Hambly, N. C. (2018). A gap in the lower main sequence revealed by Gaia Data Release 2. *Astrophys. J.*, 861(1), L11.

Jenkins, J. M., Caldwell, D. A., Chandrasekaran, H., Twicken, J. D., Bryson, S. T., Quintana, E. V., Clarke, B. D., Li, J., Allen, C., Tenenbaum, P., & et al. (2010). Initial characteristics of Kepler long cadence data for detecting transiting planets. *Astrophys. J.*, 713(2), L120–L125.

Johnson, J. A., Gazak, J. Z., Apps, K., Muirhead, P. S., Crepp, J. R., Crossfield, I. J. M., Boyajian, T., von Braun, K., Rojas-Ayala, B., Howard, A. W.,

& et al. (2012). Characterizing the cool KOIs. ii. the m dwarf KOI-254 and its hot jupiter. *Astrophys. J.*, 143(5), 111.

Juvan, I. G., Lendl, M., Cubillos, P. E., Fossati, L., Tregloan-Reed, J., Lammer, H., Guenther, E. W., & Hanslmeier, A. (2018). PyTranSpot: A tool for multiband light curve modeling of planetary transits and stellar spots. *Astron. & Astrophys.*, 610, A15.

Kipping, D. M. (2009). Transit timing effects due to an exomoon. *MNRAS*, 392(1), 181–189.

Kipping, D. M. (2014). In search of exomoons, eprint:1405.1455.

Kipping, D. M., Bakos, G. A., Buchhave, L., Nesvorný, D., & Schmitt, A. (2012). The hunt for exomoons with *kepler* (hek). i. description of a new observational project. *Astrophys. J.*, 750(2), 115.

Kiraga, M. & Stepien, K. (2011). Age-rotation-activity relations for M dwarf stars based on ASAS photometric data, eprint:0707.2577.

Kitchatinov, L. L. (2011). Solar differential rotation: origin, models and implications for dynamo. In *Astronomical Society of India Conference Series*, volume 2 of *Astronomical Society of India Conference Series* (pp. 71–80).

Kitchatinov, L. L. & Nepomnyashchikh, A. A. (2017). A joined model for solar dynamo and differential rotation. *Astronomy Letters*, 43(5), 332–343.

Kochukhov, O., Petit, P., Strassmeier, K. G., Carroll, T. A., Fares, R., Folsom, C. P., Jeffers, S. V., Korhonen, H., Monnier, J. D., Morin, J., & et al. (2017). Surface magnetism of cool stars. *Astron. Nachr.*, 338(4), 428–441.

Küker, M. & Rüdiger, G. (2011). Differential rotation and meridional flow on the lower zero-age main sequence: Reynolds stress versus baroclinic flow. *Astron. Nachr.*, 332, 933.

Küker, M., Rüdiger, G., Oláh, K., & Strassmeier, K. G. (2019). Cycle period, differential rotation, and meridional flow for early M dwarf stars. *Astron. & Astrophys.*, 622, A40.

Lanza, A. F., Netto, Y., Bonomo, A. S., Parviainen, H., Valio, A., & Aigrain, S. (2019). Stellar activity and rotation of the planet host Kepler-17 from long-term space-borne photometry. *Astron. & Astrophys.*, 626, A38.

Lehtinen, J., Jetsu, L., Hackman, T., Kajatkari, P., & Henry, G. W. (2016). Activity trends in young solar-type stars. *Astron. & Astrophys.*, 588, A38.

Lewis, K. M. & Fujii, Y. (2014). Next generation of telescopes or dynamics required to determine if exo-moons have prograde or retrograde orbits. *Astrophys. J.*, 791(2), L26.

Matilsky, L. I., Hindman, B. W., & Toomre, J. (2020). Revisiting the sun's strong differential rotation along radial lines. *Astrophys. J.*, 898(2), 111.

Maunder, E. W. (1904). Note on the distribution of sun-spots in heliographic latitude, 1874 to 1902. *MNRAS*, 64, 747–761.

Mayor, M. & Queloz, D. (1995). A Jupiter-mass companion to a solar-type star. *Nature*, 378, 355–359.

McQuillan, A., Aigrain, S., & Mazeh, T. (2013). Measuring the rotation period distribution of field M dwarfs with Kepler. *MNRAS*, 432(2), 1203–1216.

McQuillan, A., Mazeh, T., & Aigrain, S. (2014). Rotation periods of 34,030 Kepler main sequence stars: the full autocorrelation sample. *Astrophys. J. Suppl. Series*, 211(2), 24.

Mehrabi, A., He, H., & Khosroshahi, H. (2017). Magnetic activity analysis for a sample of G-type main sequence Kepler targets. *Astrophys. J.*, 834(2), 207.

Messina, S., Guinan, E. F., & Lanza, A. F. (1998). Photospheric magnetic activity in a proxy for the young sun: Hd 134319. *Astron. & Astrophys. Suppl.*, 260(4), 493–505.

Messina, S., Pizzolato, N., Guinan, E. F., & Rodonò, M. (2003). Dependence of coronal X-ray emission on spot-induced brightness variations in cool main sequence stars. *Astron. & Astrophys.*, 410, 671–684.

Morris, B. M., Agol, E., Davenport, J. R. A., & Hawley, S. L. (2018). Possible bright starspots on TRAPPIST-1. *Astrophys. J.*, 857(1), 39.

Mulders, G. D., Pascucci, I., & Apai, D. (2015). A stellar-mass-dependent drop in planet occurrence rates. *Astrophys. J.*, 798, 112.

Murphy, S. J. (2012). An examination of some characteristics of Kepler short- and long-cadence data. *MNRAS*, 422(1), 665–671.

Murray, C. D. & Correia, A. C. M. (2011). Keplerian orbits and dynamics of exoplanets.

Murray, C. D. & Dermott, S. F. (1999). *Solar system dynamics*.

Neff, J. E., O'Neal, D., & Saar, S. H. (1995). Absolute measurements of starspot area and temperature: Ii pegasi in 1989 october. *Astrophys. J.*, 452, 879.

Netto, Y. & Valio, A. (2020). Stellar magnetic activity and the butterfly diagram of kepler-63. *Astron. & Astrophys.*, 635, A78.

Ni, D. (2018). Empirical models of Jupiter's interior from Juno data. Moment of inertia and tidal Love number k_2. *Astron. & Astrophys.*, 613, A32.

Nielsen, M. B., Gizon, L., Cameron, R. H., & Miesch, M. (2019). Starspot rotation rates versus activity cycle phase: Butterfly diagrams of Kepler stars are unlike that of the Sun. *Astron. & Astrophys.*, 622, A85.

Noyes, R. W., Hartmann, L. W., Baliunas, S. L., Duncan, D. K., & Vaughan, A. H. (1984). Rotation, convection, and magnetic activity in lower main-sequence stars. *Astrophys. J.*, 279, 763–777.

Olah, K., Kővári, Z., Bartus, J., Strassmeier, K. G., Hall, D. S., & Henry, G. W. (1997). Time-series photometric spot modeling. III. thirty years in the life of hk lacertae. *Astron. & Astrophys.*, 321, 811.

O'Neal, D., Saar, S. H., & Neff, J. E. (1996). Measurements of starspot area and temperature on five active, evolved stars. *Astrophys. J.*, 463, 766.

Oshagh, M., Santos, N. C., Boisse, I., Boué, G., Montalto, M., Dumusque, X., & Haghighipour, N. (2013). Effect of stellar spots on high-precision transit light-curve. *Astron. & Astrophys.*, 556, A19.

Parsons, S. G., Gänsicke, B. T., Marsh, T. R., Ashley, R. P., Breedt, E., Burleigh, M. R., Copperwheat, C. M., Dhillon, V. S., Green, M. J., Hermes, J. J., & et al. (2018). The scatter of the M dwarf mass–radius relationship. *MNRAS*, 481(1), 1083–1096.

Perryman, M., Hartman, J., Bakos, G. A., & Lindegren, L. (2014). Astrometric exoplanet detection with gaia. *Astrophys. J.*, 797(1), 14.

Press, W. J., Teukolsky, S. A., Vetterling, W. T., & Flannery, B. P. (1992). *Numerical Recipes in FORTRAN, The Art of Scientific Computing, 2nd Edition*. Cambridge University Press.

Prusti, T., de Bruijne, J. H. J., Brown, A. G. A., Vallenari, A., Babusiaux, C., Bailer-Jones, C. A. L., Bastian, U., Biermann, M., Evans, D. W., & et al. (2016). Thegaiamission. *Astron. & Astrophys.*, 595, A1.

Raetz, S., Stelzer, B., & Scholz, A. (2020). The rotation-activity relation of M dwarfs: From K2 to TESS and PLATO. *Astron. Nachr.*, 341(5), 519–556.

Raymond, S. N., Izidoro, A., & Morbidelli, A. (2018). Solar system formation in the context of extra-solar planets, eprint:1812.01033.

Reiners, A. (2006). Rotation- and temperature-dependence of stellar latitudinal differential rotation. *Astron. & Astrophys.*, 446(1), 267–277.

Reinhold, T. & Gizon, L. (2015). Rotation, differential rotation, and gyrochronology of active kepler stars. *Astron. & Astrophys.*, 583, A65.

Reinhold, T., Reiners, A., & Basri, G. (2013). Rotation and differential rotation of active Kepler stars. *Astron. & Astrophys.*, 560, A4.

Ricker, G. R., Winn, J. N., Vanderspek, R., Latham, D. W., Bakos, G. A., Bean, J. L., Berta-Thompson, Z. K., Brown, T. M., Buchhave, L., Butler,

N. R., & et al. (2014). Transiting exoplanet survey satellite. *Journal of Astronomical Telescopes, Instruments, and Systems*, 1(1), 014003.

Rodenbeck, K., Heller, R., & Gizon, L. (2020). Exomoon indicators in high-precision transit light curves. *Astron. & Astrophys.*, 638, A43.

Rodenbeck, K., Heller, R., Hippke, M., & Gizon, L. (2018). Revisiting the exomoon candidate signal around Kepler-1625 b. *Astron. & Astrophys.*, 617, A49.

Roettenbacher, R. M., Monnier, J. D., Korhonen, H., Harmon, R. O., Baron, F., Hackman, T., Henry, G. W., Schaefer, G. H., Strassmeier, K. G., Weber, M., & et al. (2017). Contemporaneous imaging comparisons of the spotted giant σGeminorum using interferometric, spectroscopic, and photometric data. *Astrophys. J.*, 849(2), 120.

Santerne, A., Fressin, F., Díaz, R. F., Figueira, P., Almenara, J.-M., & Santos, N. C. (2013). The contribution of secondary eclipses as astrophysical false positives to exoplanet transit surveys. *Astron. & Astrophys.*, 557, A139.

Sartoretti, P. & Schneider, J. (1999). On the detection of satellites of extrasolar planets with the method of transits. *Astron. & Astrophys.*, 134, 553–560.

Schou, J., Antia, H. M., Basu, S., Bogart, R. S., Bush, R. I., & et al. (1998). Helioseismic studies of differential rotation in the solar envelope by the solar oscillations investigation using the michelson doppler imager. *Astrophys. J.*, 505(1), 390.

Schüssler, M., Caligari, P., Ferriz-Mas, A., Solanki, S. . K., & Stix, M. (1996). Distribution of starspots on cool stars. I. Young and main sequence stars of $1M_{sun-}$. *Astron. & Astrophys*, 314, 503–512.

Schüssler, M. & Solanki, S. K. (1992). Why rapid rotators have polar spots. *Astron. & Astrophys.*, 264, L13–L16.

Seager, S. & Mallén-Ornelas, G. (2003). A Unique Solution of Planet and Star Parameters from an Extrasolar Planet Transit Light Curve. *Astrophys. J.*, 585(2), 1038–1055.

Semel, M. (1989). Zeeman-Doppler imaging of active stars. i - basic principles. *Astron. & Astrophys.*, 225, 456–466.

Sestovic, M., Demory, B.-O., & Queloz, D. (2018). Investigating hot-Jupiter inflated radii with hierarchical Bayesian modelling. *Astron. & Astrophys.*, 616, A76.

Shapiro, A. I., Solanki, S. K., Krivova, N. A., Schmutz, W. K., Ball, W. T., Knaack, R., Rozanov, E. V., & Unruh, Y. C. (2014). Variability of Sun-like stars: reproducing observed photometric trends. *Astron. & Astrophys.*, 569, A38.

Shapiro, A. I., Solanki, S. K., Krivova, N. A., Yeo, K. L., & Schmutz, W. K. (2016). Are solar brightness variations faculae- or spot-dominated? *Astron. & Astrophys.*, 589, A46.

Shields, A, L., Ballard, S., & Johnson, J. A. (2016). The habitability of planets orbiting m-dwarf stars. *Physics Reports*, 663, 1–38.

Silva, A. V. R. (2003). Method for spot detection on solar-like stars. *Astrophys. J. Lett.*, 585(2), L147–L150.

Silva-Valio, A. & Lanza, A. F. (2011). Time evolution and rotation of starspots on CoRoT-2 from the modelling of transit photometry. *Astron. & Astrophys.*, 529, A36.

Silva-Valio, A., Lanza, A. F., Alonso, R., & Barge, P. (2010). Properties of starspots on corot-2. *Astron. & Astrophys.*, 510, A25.

Simon, A., Szatmáry, K., & Szabó, G. M. (2007). Determination of the size, mass, and density of "exomoons" from photometric transit timing variations. *Astron. & Astrophys.*, 470(2), 727–731.

Simon, A. E., Szabó, G. M., Kiss, L. L., Fortier, A., & Benz, W. (2015). CHEOPS Performance for exomoons: The detectability of exomoons by using optimal decision algorithm. *Publications of the Astronomical Society of the Pacific*, 127(956), 1084–1095.

Skumanich, A. (1972). Time scales for CA II emission decay, rotational braking, and lithium depletion. *Astrophys. J.*, 171, 565.

Smith, J. C., Stumpe, M. C., Van Cleve, J. E., Jenkins, J. M., Barclay, T. S., Fanelli, M. N., Girouard, F. R., Kolodziejczak, J. J., McCauliff, S. D., Morris, R. L., & Twicken, J. D. (2012). Kepler presearch data conditioning ii - a bayesian approach to systematic error correction. *Astronomical Society of the Pacific*, 124(919), 1000.

Spruit, H. C. (1976). Pressure equilibrium and energy balance of small photospheric fluxtubes. *Solar Phys.*, 50(2), 269–295.

Spruit, H. C. (2010). Theories of the solar cycle: a critical view, eprint:1004.4545.

Strassmeier, K. G., Hall, D. S., & Henry, G. W. (1994). Time-series photometric spot modeling. ii. fifteen years of photometry of the bright rs cvn binary hr 7275. *Astron. & Astrophys.*, 282, 535.

Stumpe, M. C., Smith, J. C., Catanzarite, J. H., Van Cleve, J. E., Jenkins, J. M., Twicken, J. D., & Girouard, F. R. (2014). Multiscale systematic error correction via wavelet-based bandsplitting in kepler data. *Publications of the Astronomical Society of the Pacific*, 126(935), 100.

Stumpe, M. C., Smith, J. C., Van Cleve, J. E., Twicken, J. D., Barclay, T. S., Fanelli, M. N., Girouard, F. R., Jenkins, J. M., Kolodziejczak, J. J., McCauliff, S. D., & Morris, R. L. (2012). Kepler presearch data conditioning i - architecture and algorithms for error correction in kepler light curves. *Astronomical Society of the Pacific*, 124(919), 985.

Suárez Mascareño, A., Rebolo, R., & González Hernández, J. I. (2016). Magnetic cycles and rotation periods of late-type stars from photometric time series. *Astron. & Astrophys.*, 595, A12.

Szebehely, V. & Grebenikov, E. (1969). Theory of orbits - the restricted problem of three bodies. *Soviet Astronomy*, 13, 364.

Teachey, A., Kipping, D. M., & Schmitt, A. R. (2017). HEK. VI. on the dearth of galilean analogs in kepler, and the exomoon candidate Kepler-1625b i. *Astrophys. J.*, 155(1), 36.

Trani, A. A., Hamers, A., & Geller, A. (2019). Can a hot Jupiter host exomoons? In *AAS/Division for Extreme Solar Systems Abstracts*, volume 51 of *AAS/Division for Extreme Solar Systems Abstracts* (pp. 318.18).

Tregloan-Reed, J., Southworth, J., Burgdorf, M., Novati, S. C., Dominik, M., Finet, F., Jørgensen, U. G., Maier, G., Mancini, L., Prof, S., Ricci, D., Snodgrass, C., Bozza, V., Browne, P., Dodds, P., Gerner, T., Harpsøe, K., Hinse, T. C., Hundertmark, M., Kains, N., Kerins, E., Liebig, C., Penny, M. T., Rahvar, S., Sahu, K., Scarpetta, G., Schäfer, S., Schönebeck, F., Skottfelt, J., & Surdej, J. (2015). Transits and starspots in the WASP-6 planetary system. *MNRAS*, 450(2), 1760–1769.

Tsapras, Y. (2018). Microlensing searches for exoplanets. *Geosciences*, 8(10), 365.

Twicken, J. D., Jenkins, J. M., Seader, S. E., Tenenbaum, P., Smith, J. C., Brownston, L. S., Burke, C. J., Catanzarite, J. H., Clarke, B. D., Cote, M. T., & et al. (2016). Detection of potential transit signals in 17 quarters of Kepler data: Results of the final Kepler mission transiting planet search (DR25). *Astrophys. J.*, 152(6), 158.

Valio, A., Estrela, R., Netto, Y., Bravo, J. P., & de Medeiros, J. R. (2017). Activity and rotation of Kepler-17. *Astrophys. J.*, 835(2), 294.

Vogt, S. S., Hatzes, A. P., Misch, A. A., & Kurster, M. (1997). Doppler imagery of the spotted rs cvn star hr 1099 (= v711 tau) from 1981 - 1992. *arXiv e-prints*, (pp. astro–ph/9704191).

Vogt, S. S. & Penrod, G. D. (1983). Doppler imaging of starspots. In P. B. Byrne & M. Rodono (Eds.), *IAU Colloq. 71: Activity in Red-Dwarf Stars*, volume 102 of *Astrophysics and Space Science Library* (pp. 379–385).

Weber, M. A. & Browning, M. K. (2016). Modeling the Rise of Fibril Magnetic Fields in Fully Convective Stars. *Astrophys. J.*, 827(2), 95.

Weber, M. A., Fan, Y., & Miesch, M. S. (2013). A theory on the convective origins of active longitudes on solar-like stars. *Astrophys. J.*, 770(2), 149.

Wei, J. (2018). A survey of exoplanetary detection techniques.

Wittenmyer, R. A., Wang, S., Horner, J., Butler, R. P., Tinney, C. G., Carter, B. D., Wright, D. J., Jones, H. R. A., Bailey, J., O'Toole, S. J., & et al. (2019). Cool jupiters greatly outnumber their toasty siblings: occurrence rates from the anglo-australian planet search. *MNRAS*, 492(1), 377–383.

Yadav, R. K., Gastine, T., Christensen, U. R., & Reiners, A. (2015). Formation of starspots in self-consistent global dynamo models: Polar spots on cool stars. *Astron. & Astrophys.*, 573, A68.

Zaleski, S. M., Valio, A., Carter, B. D., & Marsden, S. C. (2020a). Activity and differential rotation of the early M dwarf Kepler-45 from transit mapping. *MNRAS*, 492(4), 5141–5151.

Zaleski, S. M., Valio, A., Guimaraes, A. H. F., Carter, B. D., & Marsden, S. C. (2020b). Method for Photometric Evaluation of Gnomic Exomoons: Case Study of the Kepler-45b System, submitted.

Zaleski, S. M., Valio, A., Marsden, S. C., & Carter, B. D. (2019). Differential rotation of Kepler-71 via transit photometry mapping of faculae and starspots. *MNRAS*, 484(1), 618–630.

Zucker, S., Mazeh, T., Santos, N. C., Udry, S., & Mayor, M. (2003). Multi-order TODCOR: Application to observations taken with the CORALIE echelle spectrograph. *Astron. & Astrophys.*, 404(2), 775–781.